Nanoscale Fiber Tip Probe for Biomedical and Intracellular Sensing

Nanoscale Fiber Tip Probe for Biomedical and Intracellular Sensing

A DISSERTATION PRESENTED

BY

WOOYOUNG HONG

TO

THE DEPARTMENT OF CHEMISTRY AND CHEMICAL BIOLOGY

IN PARTIAL FULFILLMENT OF THE REQUIREMENTS

FOR THE DEGREE OF

DOCTOR OF PHILOSOPHY

IN THE SUBJECT OF

CHEMICAL PHYSICS

HARVARD UNIVERSITY

CAMBRIDGE, MASSACHUSETTS

MAY 2016

Thesis advisor: Professor Marko Loncar   Wooyoung Hong

Nanoscale Fiber Tip Probe for Biomedical and Intracellular Sensing

Abstract

Fluorescent-labeling imaging techniques have been widely used in live cell studies; however, the labeling processes can be laborious and challenging for non-transfectable cells and clinical cells, and labels can interfere with protein functions. In this thesis, we present the first demonstration of label-free detection and quantification of intracellular biomarker dynamics with a nanoscale localized-surface-plasmon fiber-tip-probe (LSP-FTP). Our results have established the FTP technique as a new tool to study the time dynamics of proteins and protein phosphorylations in single live cell, and could be generalized to study other types of primary cells in response to external triggers, including drugs.

Chapter 2 focuses on the fabrication methods of fiber tip probes (FTPs). FTP is a lab-on-a-fiber probe wet-etched at nanoscale dimensions. The base material of FTPs may comprise any solid materials as long as they have matching etchants. FTPs take various configurations and may comprise of single-ended fiber, double-ended fiber, or an end-portion or mid-portion nanowire with various aspect ratios. Structures of FTPs

can be tuned at nanoscale accuracy with extreme surface smoothness. These FTPs can be mass-fabricated and multiplexed at a single fabrication step and at low cost.

Chapter 3 discusses the procedures and results on measuring intracellular biomarker dynamics in intact live cells. We demonstrated label-free detection of tumor suppressor p53 dynamics in single HeLa cells under ultraviolet radiation and under treatment with neocarzinostatin (NCS). Also, we employed the FTP technique to prove that β-Amyloid generation precedes Tau phosphorylation by continually monitoring intracellular levels of β-Amyloid and phosphorylated Tau in live human neuroblastoma cells (SY5Y).

Chapter 4 discusses other potential applications of FTPs. An FTP with a nanodiamond at its tip can be used to measure various intracellular properties such as electromagnetic fields, temperature, or pressure. Manipulation of electron spins at nitrogen-vacancy centers in a nanodiamond allows these measurements. An FTP with a plasmonic particle at its tip can be used for surface-enhanced Raman spectroscopy (SERS) and potentially allow single molecular detection. A mechanical FTP with an end-portion nanowire (a few hundred micrometers long and sub-micron thick) functions as a cantilever sensor, and we can detect changes in its vibration modes induced by binding of analytes to a reaction entity immobilized relative to the nanowire. Free-standing FTP waveguides with a sub-micron portion in diameter can be used for efficient light coupling and device characterizations.

Contents

For Mom and Dad

Acknowledgments

I acknowledge Jesus Christ as my savior and my lord who bestowed upon me the wisdom, the knowledge, the peace in my mind, and the good health, all of which allowed me to finish this thesis.

I would like to thank Dr. Qimin Quan and Prof. Marko Loncar for their expertise, generous guidance and encouragement. Their support has been a guiding light for me to work on the biosensor projects and present my work of the past five years in my thesis. I learned how to conduct research, which is very different from mere studying. From their advice and comments, I learned (1) the significance of background knowledge and literature search on previous works for gauging the research feasibility and meaningfulness, (2) the scientific insight on not naively believing in the data but interpreting them critically, (3) the scientific creativity to decide what paths to progress the research, (4) the leadership to set up clear research goals and wrap up projects, and (5) work ethics to cooperate with group members in the most efficient way.

I still remember the day when I brought my research proposal to Qimin and

Marko for review and discussed its feasibility with Qimin at the second floor lab of McKay building. It was an exciting and life-changing moment for me to join Marko lab and work closely with Qimin, when Qimin just started the lab at Rowland Institute of Harvard. I learned a lot from seeing Qimin building up the lab and progressively achieving many scientific advances. When working on the intracellular biomarker sensing project, I thank his support and guidance to spend over many nights trying to make the project work and discussed the research breakthrough and progress at daily basis. Also, he was very considerate not only on my research progress but on my general well-being. Qimin was my mentor, coworker, and friend.

I thank Marko for his generous support. He was always very supportive on the new ideas that we proposed and gave us the best advice for progress. Also, whenever I had a hard time not making expected research progress, he always tried to understand my situation and provided the best guidance in terms of both insightful research advice and emotional support. I could complete the doctoral program mainly due to his generous understanding and guidance.

I thank Prof. George Whitesides, Prof. Marko Loncar, and Prof. Adam Cohen for their invaluable advice and comments on my annual progress. They were on my advisory committee and gave me evaluation and invaluable advice when I made big decisions of my research. It was a great honor to interact with renowned, admired researchers like them.

I also want to specially thank my collaborators, Dr. Feng Liang, Dr. Diane Schaak,

1

Introduction

1.1 Outline of the Thesis

In this thesis, we will focus on how to fabricate nanosize lab-on-a-fiber probe in a scalable and reproducible manner and will demonstrate and propose applications of this nanosize tool in biomedical and intracellular sensing[52,77].

Chapter 2 will focus on how to fabricate different configurations of the fiber tip probe (FTP). FTP is a fiber wet-etched at nanoscale dimensions. One type of FTPs is a tapered optical fiber that has a sub-100nm tip in diameter (Figure 1.1). A single nanosensor can be attached to its tip. It is composed of a starting portion of initial cylindrical optical fiber, a tapered portion with tunable tapering lengths and angles, and an end portion of nanosize cylinder with tunable diameter scaling down to <100nm and with tunable length from sub-micron to several hundreds of micrometers. Various scalable shapes of starting, tapered, and end portions can be combined, and the materials such as silica, silicon, silicon nitrite, or metals can be used to form an FTP device. Immobilization method of various nanosensors such as antibody-functionalized nanoparticles, functional polymers, or nanodiamonds at the FTP tip will be discussed.

Chapter 3 will describe a localized-surface-plasmon fiber-tip-probe(LSP-FTP) approach to detect biomarkers in the high-ionic cell culture medium and inside single live cells. The three-dimensional shape of FTP enables *in-situ* analysis of biomarkers without fluidic delivery systems, which will be especially useful for detecting biomarkers in primary cells or precious clinical samples at nanoscale spatial resolution. We present the first demonstration of label-free detection of dynamic concentration change of intracellular p53 in a HeLa cell with a nanoscale FTP. Furthermore, we demonstrate continually monitoring levels of β-Amyloid and phosphorylated Tau in individual live human neuroblastoma cell (SY5Y) and show that Aβ42 generation

2

precedes Tau phosphorylation, which then facilitates the Aβ42 generation.

Chapter 4 will discuss other potential applications of FTP approach. Spin states of nitrogen-vacancy (NV) centers in a nanodiamond immobilized at the nanosize FTP tip can be optically addressed for measuring cellular electromagnetic fields, temperature, and pressure. An LSP-FTP with an immobilized plasmonic particle can be used for surface-enhanced Raman spectroscopy (SERS) and detect single molecules. A nanoprobe with a nanosize cylinder of high aspect ratio (>100μm in length and <1μm in diameter) at an FTP tip can function as a mechanical cantilever sensor that can potentially measure temperature, humidity and floating pollutants in air. A plasmonic metasurface fabricated at a flat microsize fiber tip allows superfocusing and optical trapping of nanosensors at its tip and can be used as a basis for a non-invasive bioprobe for cellular interrogation.

Appendix section will focus on the theoretical background required to understand the various applications of FTPs. We will discuss surface plasmon polariton of metals, mechanical vibration of a cantilever, and optical trapping force of a focused light. In addition, we will discuss how error bars should be used to interpret results correctly in experimental cell biology.

1.2   Motivation and Scientific Achievements

Fluorescent imaging technology has been extensively used to study living cells, including protein function, metastatic processes, and signaling networks[78,37]. However, reliable fluorophore labeling is laborious and challenging, for example, as biomarkers are dynamically synthesized and redistribute inside the cells[112,104]. *De-novo* expression of fluorescent proteins, such as green fluorescent proteins (GFP), can be difficult to implement for non-transfectable cells, and labels can change protein dynamics, especially with proteins where slight modification of the proteins might change the dynamics of the signaling, and further affect the cell response[126,72]. An alternative strategy is to make nanoscale sensors (which are two to three orders of magnitude smaller than cells), physically place into the cells, detect proteins and transduce the biological signal to an optical or electronic signal[123,118,109,137,107,131,75]. In this thesis, we describe the fiber tip probe (FTP) technique as a step toward this goal[52,77].

FTP is a lab-on-a-fiber probe wet-etched at nanoscale dimensions. One type of FTP mainly discussed in this thesis is a tapered optical fiber with a nanosize tip that carries a nanosensor at its end (Figure 1.1). For real-time intracellular biomarker detection, a gold nanorod is used as the nanosensor. Transistor-based electrical biosensors cannot function at cellular ionic concentrations, because analyte charges are screened out by the interfacial double layer[123,7]. On the other hand, a gold nanos-

4
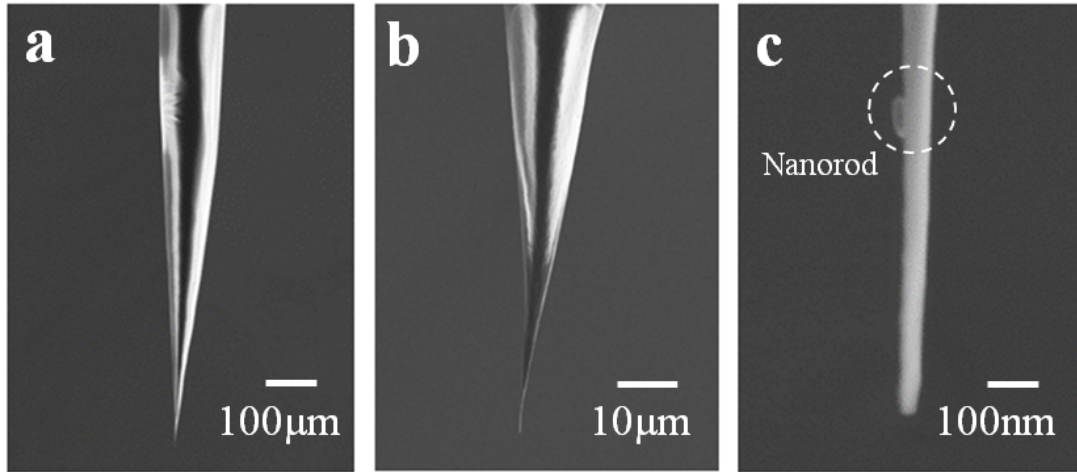
Figure 1.1: Scanning electron microscope (SEM) image of a LSP-FTP. (a) An optical fiber is gradually tapered from 125 µm to sub-100 nm. (b,c) Enlarged SEM images of the end portion of an FTP. A single nanorod is immobilized at the FTP tip.

tructure carries localized surface plasmons (LSPs) sensitive to the local change of refractive index around the nanostructure, and the optical signal is independent to the ionic concentration[6,145]. We present the first demonstration of label-free, real-time detection of intracellular protein concentration dynamics with a nanoscale fiber tip probe (FTP)[52,77].

Other forms of FTPs can be fabricated and used for various purposes. We propose using a nanodiamond-FTP sensor for measuring intracellular temperature, pressure, or electromagnetic field such as neural or cardiac action potentials. We can fabricate a mechanical FTP with an end-portion nanowire at high aspect ratio functions as a microcantilever mass spectrometer. Double-ended FTP with a mid-portion

nanowire can be fabricated and used for efficient light coupling to planar photonic structures for optical characterization.

We invented methods to fabricate various configurations of nanosize FTPs with extreme smoothness (Figure 1.2). Structures fabricated via wet-etching method often have rough surface due to continual etching of etchant remnants on the surface left while extracting them from the etchant. The structural roughness can be detrimental when the structure size becomes at order of wavelength, because light scatters on its rough surface and cannot be carried along the fiber. Our fabrication method can maintain smoothness all over the structure with various structural configurations.
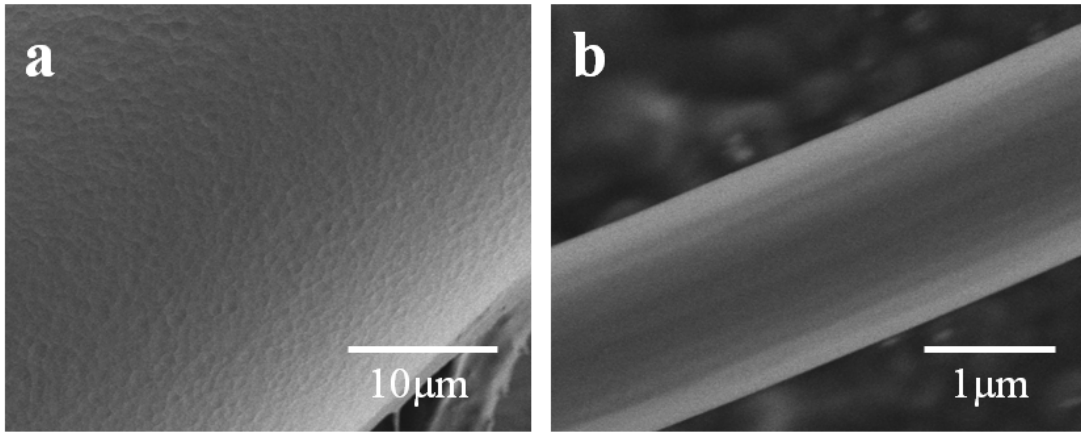
Figure 1.2: Scanning electron microscope (SEM) image of surface roughness of FTPs. (a) FTP etched via traditional meniscus etching method. Surface is covered with crater-like rough features (several microns in size) (b) Surface of FTP etched via two step meniscus etching method (detailed description in Section 2.3). Surface is much smoother.

1.3 Commercialization Potential of FTP and Fabrication Technique

Nanodevices carry its unique physical characteristics that are not found in conventional devices and are better understood these days for innovative biomedical, optical, material science applications. Nanotechnology has been undergoing transition from laboratories to commercial applications. However, nanotechnology processes are often non-scalable and require significantly large funding and longer term commitments of cash flows. Our patented FTP fabrication processes are wet-chemistry-based, which is scalable, mass-producible, and significantly less-expensive.

The resulting structures can be at any dimensions ranging from microstructures to sub-nanometer precisions, and identical nanosize bioprobes can be processed at the same fabrication round and at low cost. The structures can be fabricated with any base solid material as long as the material has a matching etchant[133]. Also, multiple structures cab be assembled and be used for 3D multiplexed mapping[101] of biological or physical systems.

We mainly discuss biological applications of fiber tip probe (FTP) in this thesis. FTP can target any intracellular biological markers with a nanosensor functionalized with antibodies. Also, FTPs provides nanoscale spatial resolution and allows quantitative measurement of intracellular biomarker dynamics. FTP can function

as an excellent tool to elucidate fast, unknown biological pathways, study real-time pathogenic strains of small bacteria and viruses, and interrogate precious or non-tranfectable cells such as patients' cells.

The FTP device can be also used outside biology disciplines. For example, free-standing FTP waveguides can be used for efficient optical coupling and photonic device characterization. We thinned the mid portion of a fiber to a sub-micron in diameter for efficient coupling to diamond waveguides at visible wavelength[23]. Laser-pulled optical fiber cannot be stably pulled to sub-micron and be used for coupling at visible regime. Double-ended tapered fibers can be used for transmission measurements at visible wavelengths, and single-ended tapered fibers can be used for reflection measurements at visible wavelengths (Figure 2.6).

2

Versatile Fabrication Methods of FTP

In this chapter, fabrication optimization protocols of fiber tip probes (FTPs) will be discussed. Our wet-chemistry fabrication method allows surface roughness control at sub-nanometer accuracy and provides high throughput, scalability, mass-producibility, multiplexing capability, and cost effectiveness. In addition, an FTP may comprise of any base material that can be wet-etched.

2.1 Selective Etching and Miniscus Etching Method

Many publications discuss methods for fabricating near-field scanning optical microscopy (NSOM) tips. The two most common techniques are adiabatic pulling and chemical etching[42,17,96,89,84]. The pulling technique is not suitable for structures with large cone angles[42]. Also, the large cone-angle tips provide at least an order of magnitude higher optical efficiency and preserve polarization properties better, in comparison to the pulled tips. There are two different general wet-etching techniques, meniscus etching and selective etching (Figure 2.1). One advantage attributed to selective etching over conventional meniscus etching is the extremely smooth glass surface and taper shape that is produced, probably due to the protective environment of the tube enclosure[84]. However, the tip geometries of the fiber are limited for the tube etching method due to the fixed position of unetched acrylic jackets. We goal to fabricate a tapered optical fiber with a <100nm nanowire tip, and our tweaked meniscus method allows more versatility on the structures and extreme surface smoothness. In this chapter, we focus on wet-etching optical fibers with hydrogen fluoride etchants or related families. We note, however, that using our method it is possible to etch any materials including metals, silicon, silicon nitride with its corresponding etchants into the fiber-tip-probe (FTP) configuration.

The fiber tip probe (FTP) was fabricated from the widely available glass opti-

cal fibers. Glass fibers (SM28, Thorlabs Inc.) were etched with hydrogen fluoride (HF) wet chemistry to taper the tip down to sub-100 nm size (Figure 2.2). First, the acrylate coating layers of the optical fibers were removed. These stripped fibers were cleaved to generate flat facets. A fiber holder that can hold as many as 10 fibers was mounted on a translational stage. Fiber ends were immersed in the piranha solution ($H_2SO_4 : H_2O_2 = 3:1$) for 10 minutes for cleaning and rinsed with de-ionized water. Subsequently, these cleaned fibers were perpendicularly dipped into the HF/o-zylene interface, roughly 1 mm deep. The hydrofluoric acid wets the fiber surface with an initial meniscus height (Figure 2.2a). The fiber tip was sharpened by the gradual reduction of the etchant meniscus height that was associated with the decrease of the tip diameter during etching (Figure 2.2b). In order to prevent the disturbance on the etching rate and maintain smoothness throughout the tapered section of the fiber, all the way to the nano-tip, the etching apparatus was placed on the air-floating optical bench and in a windproof enclosure. The whole etching process could be monitored with a CCD camera. After 35 minutes, the fibers were first taken out of HF/o-xylene and rinsed immediately with de-ionized water in order to prevent further etching by residual HF. To further fine-tune the tip size, we replaced the HF with Buffered Oxide Etch (5:1 BOE), as BOE has an etch rate 1/10th of HF. The etching time in BOE was precisely controlled, and the etched fiber was compared to an image of fibers with known sizes under the optical microscope. As shown in Figure 2.2c, we achieved the sub-100 nm tip size.

11
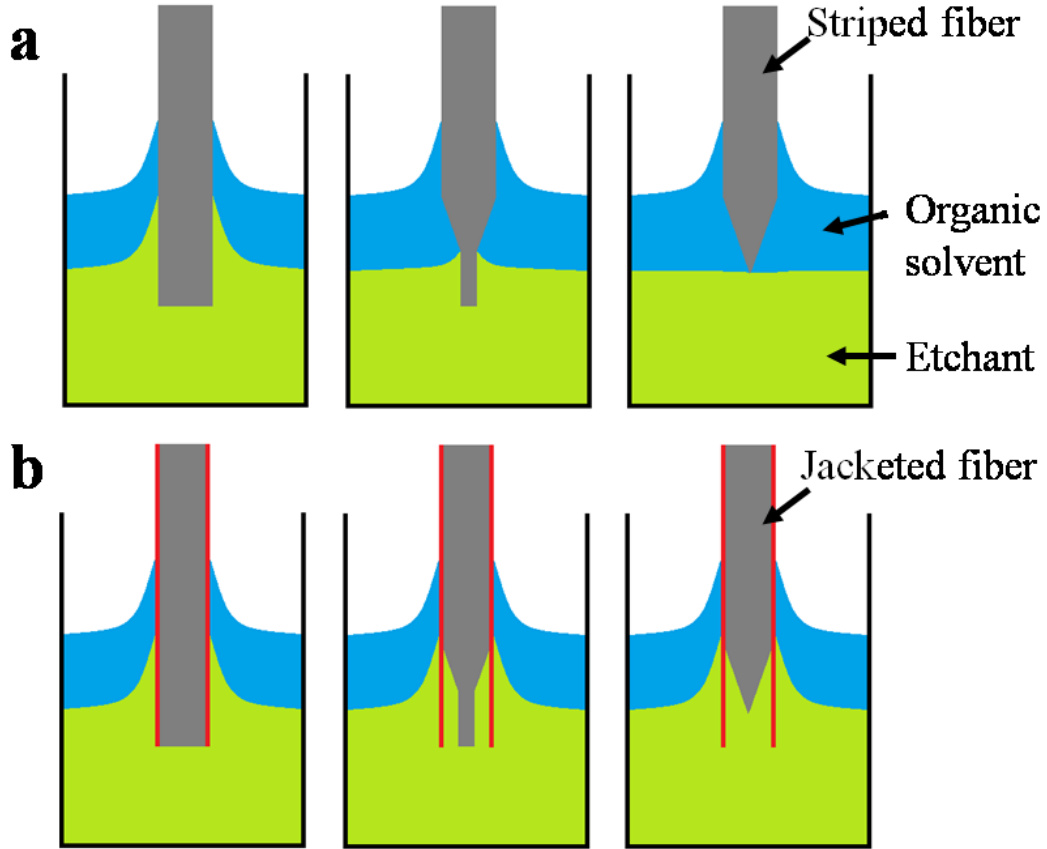
Figure 2.1: Schematics of two different etching methods. (a) Meniscus etching process. All cases show the fiber at time zero (left), at time $\tau/2$ (middle) and at time τ (right). The meniscus formed at the liquid–liquid and liquid–solid interfaces lowers height, as the fiber radius decreases. When the fiber radius converges to zero at time τ, the final taper portion is created. (b) Selective etching processes. As soon as a preliminary taper is formed (middle), convection starts to deliver the hydrofluoric acid to the upper region of the cone. This convection is driven by concentration gradients caused by the etching process and the gravitational removal of the reaction products.
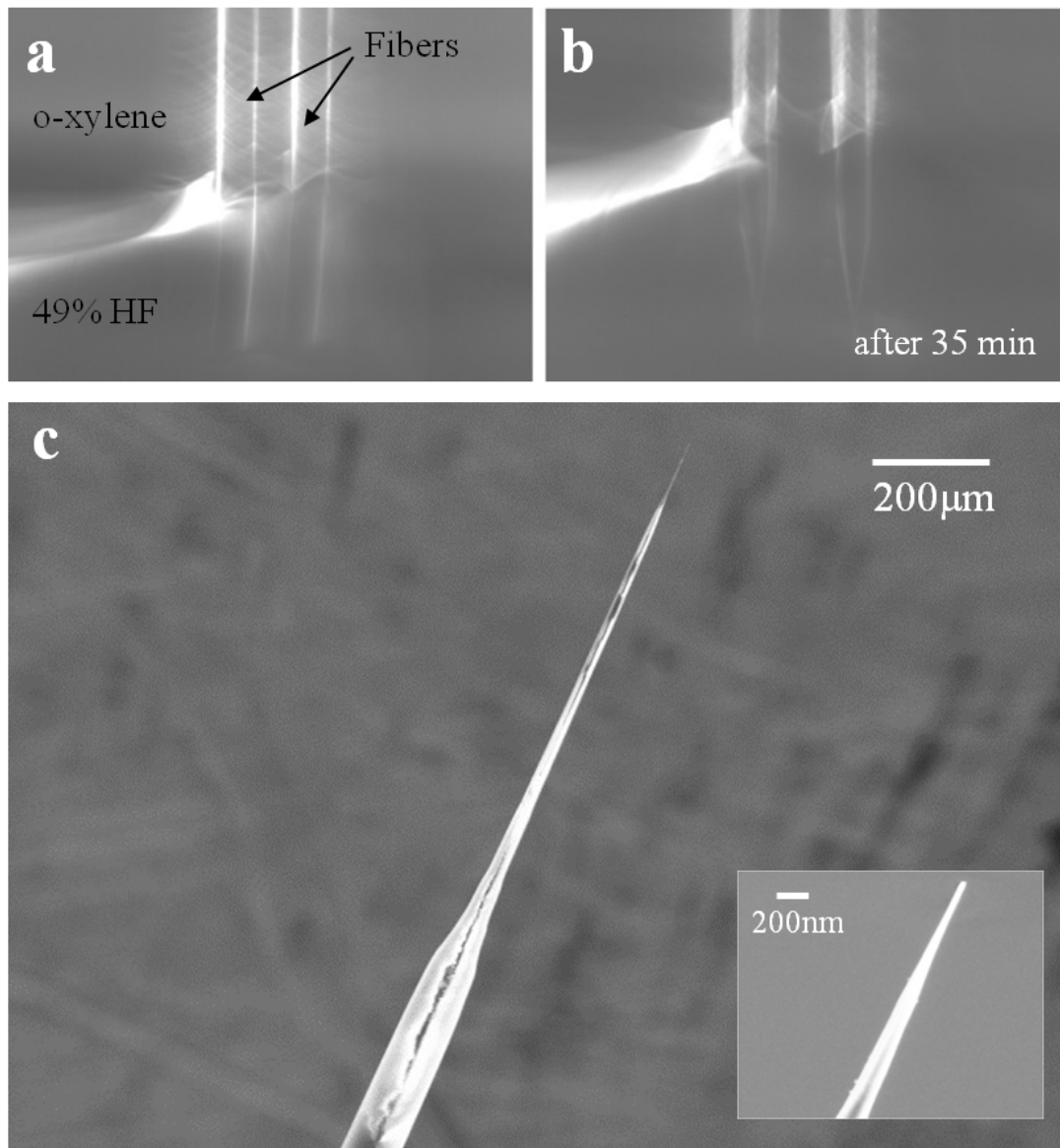
Figure 2.2: Image of fibers wet-etched to form FTPs. (a) and (b) Optical microscope image of two fibers before (left) and after etching (right). After 35 minutes of etching, taper portion at the fiber tips could be clearly seen. (c) SEM image of a fiber etched to form two taper shapes. Inset figure, the magnified SEM image of the FTP tip, shows that the tip is roughly 85nm in diameter.

13

2.2 Conic Angle and Aspect Ratio Control

Controlling conic angle of NSOM tips has been well studied[42,50]. Different organic layers can be used to produce different cone angles ranging from 8.5 to 41°[50], or by moving the fiber at variable speeds for different times, a variety of tip cone angles can be created[42]. For our silica fiber tip probe (FTP), we used o-xylene as an organic layer that produces roughly 30° cone angle.

We focused on expending the previous efforts on fabricating NSOM tips and invented a novel structure which encompasses a nanowire of various aspect ratios at the conic tip. For intracellular interrogation, we want minimal invasiveness when the FTP is inserted into the cell membrane, keeping its cellular physiology intact. The FTP with a nanoscale end-portion nanowire of <100nm thick and a few micron long can be created for this purpose (Figure 2.2). We can also fabricate an end-portion nanowire with high aspect ratio larger than 400 (Figure 2.3 and 2.4). These nanowires can function as a mechanical cantilever sensor which changes its natural frequency when the effective mass of the nanowire changes. Materials coating the nanowire may change its mass or volume in response to analyte adsorption, leading to the resonance frequency shift. In order to fabricate these structures, we immerse the fiber in a solution where the length of the nanowire is roughly equal to the length of a fiber immersed below the initial interfaces between an organic protective solvent and an

etchant (Figure 2.3a). By precisely controlling the etching time and the etchant concentration, we can create a <1μm-thick nanowire with high aspect ratio larger than 400.

For characterization of optical properties of photonic devices such as microring resonators, double-ended tapered silica fibers are often used for efficient optical coupling and transmission measurement. For optical characterization at telecom wavelength, an optical fiber can be pulled and dimpled to have a thin coupling region with thickness on the order of the telecom wavelength. However, it is possible but not reproducibly pull the fiber below 1 micron in thickness[125]. The sub-micron thick portion of the fiber functions as a waveguide with larger evanescent field, the exponentially decaying part of the guided light outside the waveguide, subject to coupling with the photonic devices at visible wavelength. For transmission measurements at visible wavelengths, double-ended fiber tapers were manufactured from commercial SM-600 fiber (Thorlabs) via meniscus wet-etching in hydrofluoric acid (Figure 2.5). Bare SM-600 fiber was mounted in a U-shape configuration, followed by localized wet-etching in hydrofluoric acid near the center. The final taper region at the center had a diameter of 500 to 700 nm. We used this double-ended tapered fiber for optical characterization of single-crystal diamond optical nanocavities (Figure 2.6a)[23,22]. Double-ended fiber is used for transmission measurement. The fiber configuration can be fined tuned such that the single-ended FTP can efficiently couple to the diamond nanocavities for reflection measurement (Figure 2.6b and 2.6c)[22].
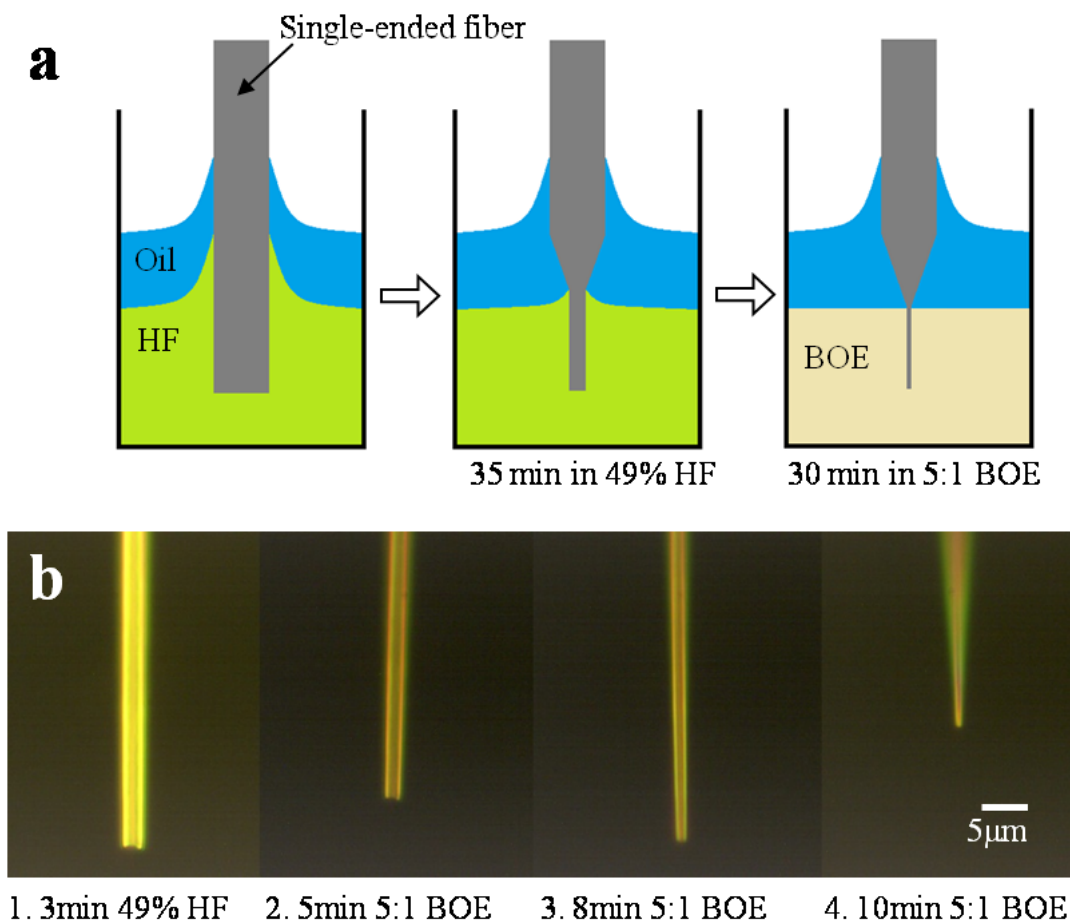
Figure 2.3: HF wet-etching process for mechanical FTP fabrication. (a) Schematics of the etching procedures for a mechanical FTP. The fiber is deeply immersed in HF/o-xylene interface for 35 minutes (left). The distance of the fiber immersed below the height of the original interface would be the length of the end-portion nanowire. After the fiber is etched to roughly 5 μm (center), the fiber is retracted out and immersed in 5:1 BOE/o-xylene interface for 30 minutes (right) until the end-portion nanowire is etched to sub-micron in diameter. (b) Optical microscope image of an end-portion nanowire at an FTP tip. After 35 min etch in the hydrofluoric acid solution, the FTP is etched with 5:1 BOE for surface smoothness and fine control of diameter. The nanowire gradually thins as immersed longer in the etchant.

16
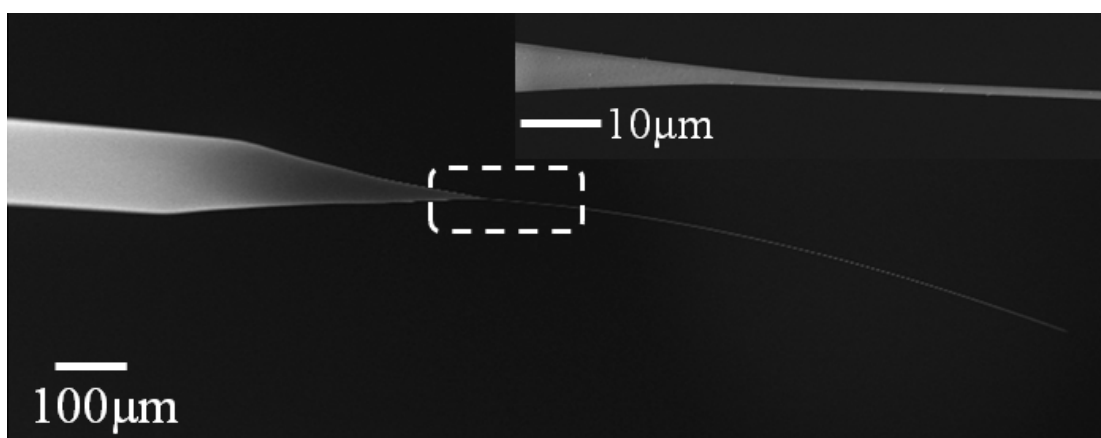
Figure 2.4: SEM image of a Mechanical FTP. The aspect ratio of the end portion of the fiber is >800 (>800 μm in length and sub-micron in diameter). Inset is a magnified SEM image of an FTP portion in the white dotted box.
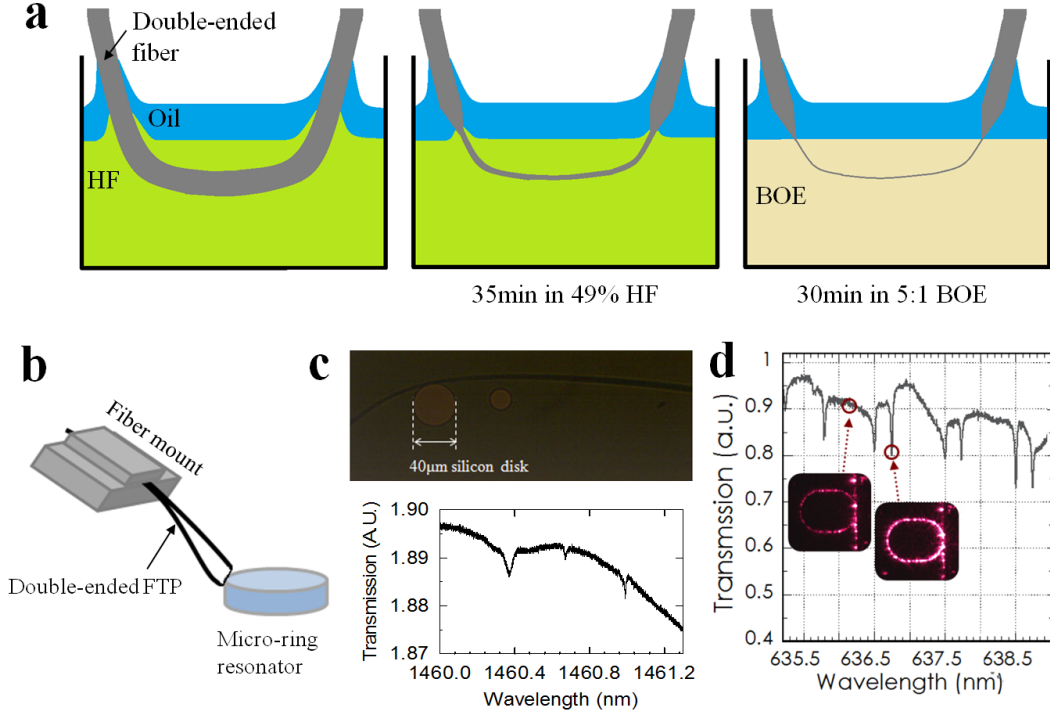
Figure 2.5: Double-ended FTP for optical structure characterization. (a) Schematics of the etching procedures for a double-ended FTP. Double-ended fiber is mounted on U-shaped boat for fixation and went through two step meniscus etching process to create sub-micron detection hotpot in the center of the fiber. (b) Schematics of characterization of a silicon ring resonator. The free-standing double-ended FTP mounted on a fiber holder was approached to a silica disk in three-dimension. The detection regime of the double-ended FTP is a flat mid-portion nanowire with sub-micron thickness. (c) Telecom broadband transmission measurement of a diamond nanocavity coupled with a double-ended fiber. Top shows an optical image of a double-ended FTP coupled with a silicon optical ring resonator. Bottom shows telecom transmission spectra. Transmission dips correspond to the resonant modes. (d) Visible broadband transmission measurement of a diamond nanocavity coupled with a double-ended fiber[22]. Transmission dips correspond to the cavity modes. The two inset figures show that the diamond nanocavity did not scattered much at frequency not critically coupled (left), but it scattered much brighter at the resonance frequency (right).

18
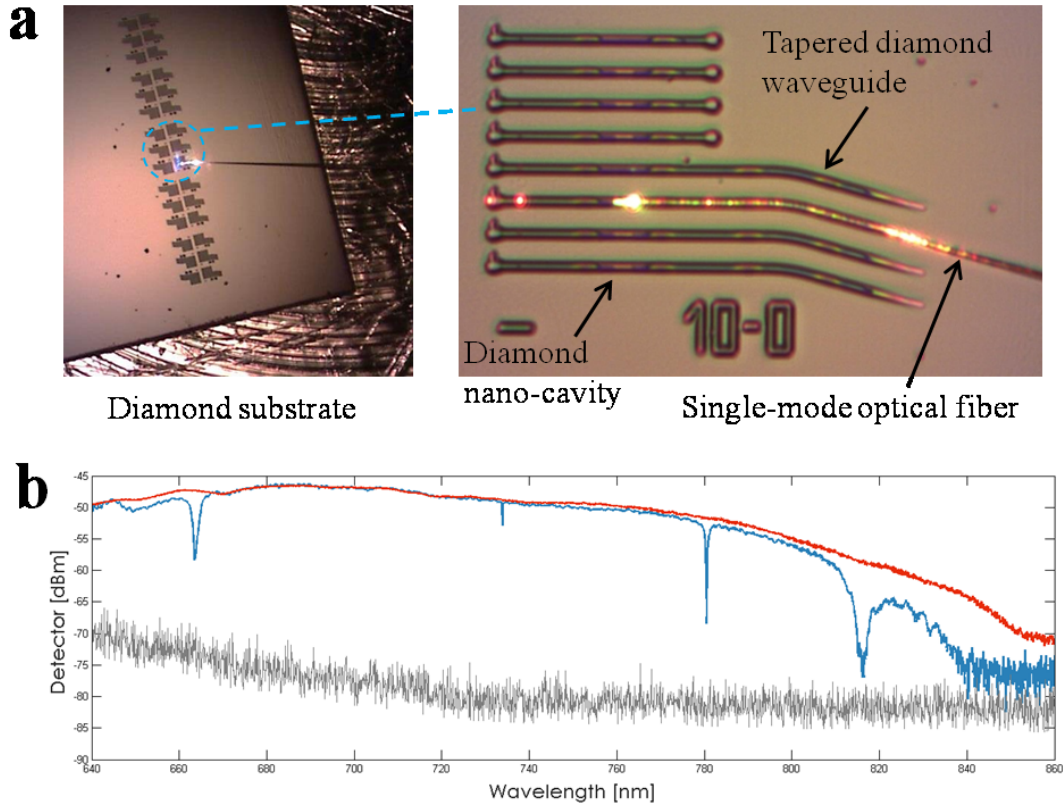
Figure 2.6: Reflection measurement of a diamond optical nanocavity with a single-ended FTP at visible regime[22]. (a) Optical image of coupling setup. A fiber is delivered one diamond nanocavity to couple light through the photonic device and collect reflected light from the device. (b) Reflection spectra of a diamond nanocavity coupled with a single-ended fiber. The graph includes control reflection spectra (gray curve) measured in air, reflection spectra at off-resonance (red curve) and TE-like (blue curve) polarized light transmitted through the diamond nanobeam waveguide which contains the optical cavity. Reflection spectra of TE-like mode shows clear resonance features.

2.3   Surface Smoothness Control

For NSOM fabrication, selective etching method is favored over meniscus etch-ing method, because structures from the meniscus method suffer from its rough sur-face. We found that the roughness from the meniscus method comes from the rem-nants of etchants when we extract the fibers from HF/o-xylene solutions. The radius of crator-like roughness decreases as the concentration of etchant decreases (Figure 1.2a). In order to smoothen the surface, a two-step etching process which includes roughly 35 minutes of etching in concentrated hydrofluoric acid, followed by 30 to 50 minutes etching in 5:1 buffered oxide etch (BOE) was used to thin 125μm-thick optical fiber to sub-micron in diameter (Figure 2.3).

For structures that require sub-nanoscale smoothness, rather than extracting the fiber from the etchant, we gradually diluted the etchants in order to prevent any remnant droplets to result in surface roughness (Figure 2.7a). This dilution menis-cus method prevents any etchant remnants to remain on the surface and contributed to creating roughness. De-ionized water enters from the upper tube and dilutes the etchant, while the original hydrofluoric acid is pumped out from the lower tube. Al-ternatively, higher concentration of etchants can enter through the upper tube in order to increase the etching concentration. Given that the flow rate from both tubes re-main constant, the etchant concentration gradually lowers while the solution level

remains even. By controlling the etching concentrations of the solvents, the shape and smoothness of FTPs can be delicately controlled.

We propose alternative triple-layer meniscus method to create smooth surface on FTP (Figure 2.7b). This method has additional polar solvent layer on top of the non-polar protective layer. This extra polar solvent serves as a cleaning solution that washes off and minimizes exposure to the etchant remnants on the device surface during the extraction of FTPs from the layered etching solvents. The density of the top polar solvent should be lower than the organic layer, and acetonitrile/cyclooctane/HF can form the triple-layer system where their densities are 0.786 g/ml, 0.834 g/ml, and 1.06 g/ml respectively.
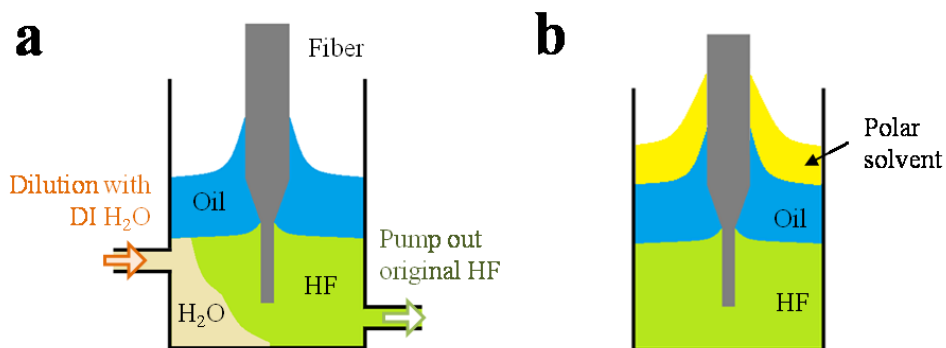
Figure 2.7: Two different etching schemes for smooth FTP surface. (a) Dilution etching method. Etchant is gradually diluted by the inflow of de-ionized water and the outflow of original HF etchant. This method results in much smoother surface by removing the etchant remnants left on its surface during its extraction from the etching solution. (b) Triple-layer etching method. The top polar solvent layer serves as a cleaning solution that washes off the etchant remnants from the FTP during extraction.

2.4   Multiplexing of FTPs

Since FTPs are fabricated via wet-chemistry, they can be scalable and mass-producible, a critical feature for commercialization by greatly reducing fabrication time and cost. A plurality of optical fibers can be simultaneously exposed to an etchant. For example, the materials can be individually applied, or an array of such materials can be simultaneously exposed to an etchant. As shown in in Figure 2.8a, a plurality of fibers, of which acrylic jackets were striped off at their tips, were fixed with an adhesive and formed a a bundle evenly spaced at the thickenss of the arcyrlic jacket. (e.g. spaced 250 μm apart, while the silica fiber is 125 μm thick). The spacing between the fibers can be tuned, and a much large number of fibers can form the fiber bundle, simultaneously etched, and have identical end structures.

The FTP bundle can be used to couple light through a periodically-spaced photonic waveguides or characterize periodically-spaced physical system. Also, multiple FTPs can form a circular bundle that can be used to interrogate single cells and map intracellular dynamics in three dimensions.
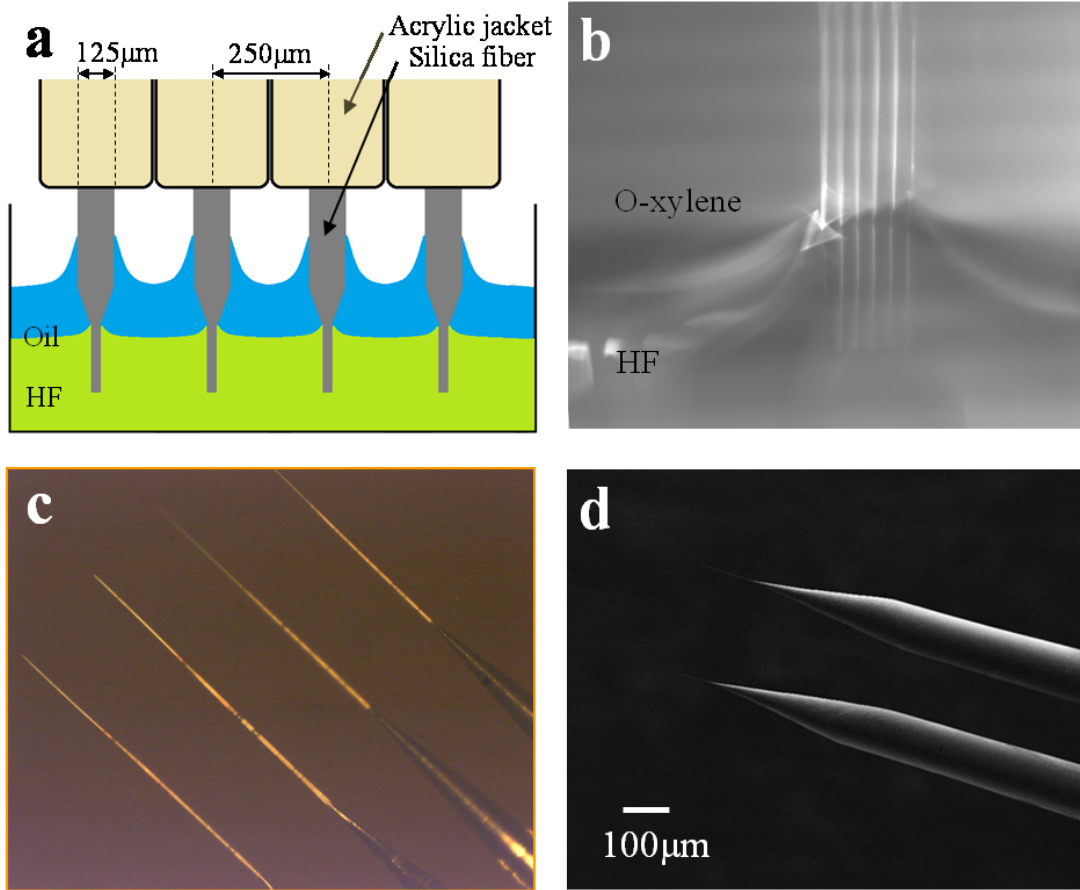
Figure 2.8: Multiplexing of FTPs. (a) Schematic of multiplexed etching procedures. Multiple fibers can form a bundle and be etched simultaneously. Spacing between fibers is determined by the acrylic jacket thickness (250 μm). (b) Optical microscope image of a plurality (three) of optical fibers immersed in the HF/o-xylene solution. (c) Image of multiplexed mechanical FTPs spaced 250 μm apart from one another. (d) SEM image of two mechanical FTPs spaced 250 μm apart from each other.

2.5   Immobilization of Nanoparticles on FTP

We can conjugate a single nanoparticle at the sub-100nm tip of an FTP. The gold nanorod were first dispersed onto a cover-glass and could clearly be observed under dark field (Figure 2.9). FTP was then dipped into an optical adhesive (Norland NOA 138) for a few seconds and immediately mounted onto the 3D micro-manipulator. The FTP precisely moved to the top of a single gold nanorod, and picked up the gold nanorod before the adhesive dried up[59]. The pig-tailed end of the FTP was then connected to a halogen lamp, whose UV components cured the optical adhesive.

This process require precise alignment of an FTP and a gold nanorod, which may limit mass-production of FTP devices. Instead of picking up a nanostructure, I propose electroless plating of thin gold films directly at the FTP tip, a wet-chemistry procedure[132]. A fresh HF-etched FTP tip is exposed to a solution containing Sn^{2+} ions, which are oxidized by the self-assembled layer of elemental silver. Gold replaces elemental silver via the galvanic-driven displacement. Gold films with thicknesses less than 100 nm were grown at 3 and 10 °C between 0.5 and 3 h, with mean grain sizes between 20 and 30 nm. The film's height depends on the height of the FTP immersed in the gold-plating solution, and its thickness depends on the time and temperature that the FTP remains in the solution. The nanosize gold film at the FTP tip should also carry localized surface plasmons (LSPs) sensitive to the local refractive index

24

change around the film.
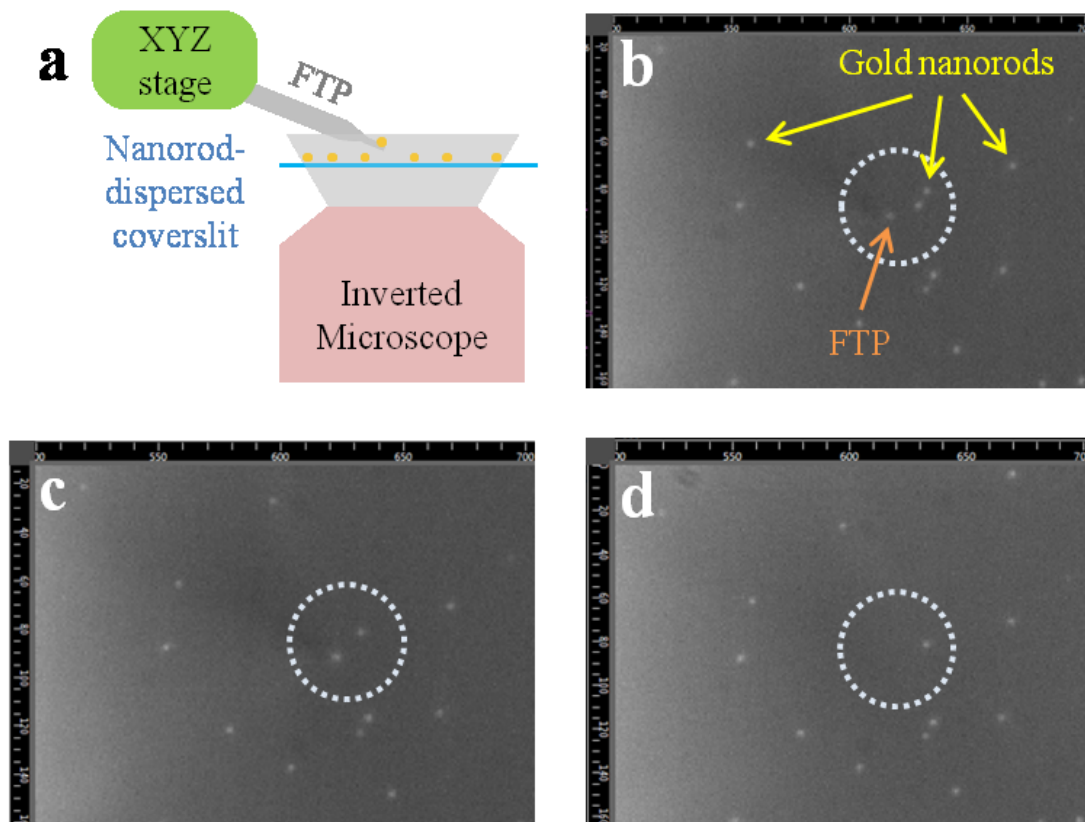
Figure 2.9: FTP conjugation with a single gold nanorod. (a) Experimental setup for picking up a single nanoparticle from the coverglass (b-d) EMCCD image from scattered light collected through the objective lens during the pick-up process of a single nanoparticle from the surface by an FTP. Circled area is a target region with an FTP (indicated with an orange arrow) approaching to pick up one of individual nanorods (indicated with yellow arrows). The tip (b) was applying shear-force onto the surface, (c) has established a contact to one particle, and (d) was conjugated with a nanorod and is retracted from the surface.

<div style="text-align: right">

3

</div>

Intracellular Sensing with FTP

3.1   Introduction

Much of our knowledge in biology so far is based on ensemble measurements on

cells[5]. However, the stochastic expression of genes, proteins and metabolites result in

cellular heterogeneity. A major challenge is to understand how individual cells pro-

cess information and respond to stimuli. Current techniques that measure intracellular proteins either are destructive to cells (e.g., enzyme-linked immunoassay, western blot) or require transfected cell lines or transgenic animals (e.g., fluorescent imaging)[78,37]. Emerging microfluidic techniques are constantly improving the detection and sample manipulation capability[140]. Fluorescent imaging is powerful technique for live cell imaging, but it is not efficient for primary cells and clinical samples. An alternative strategy is to make nanoscale sensors, physically place into the cells, detect proteins and transduce the biological signal to an optical or electronic signal. So far, intracellular action potential has been measured with three-dimensional nanowire field-effect transistors[123], intracellular pH has been measured with nanofibers,[118] and cellular endoscopy has been demonstrated with carbon nanotubes[109], nanowires[137], and nanobeams[107]. Vo-Dinh et al. further demonstrated the detection of enzymatic fluorescent intracellular proteins by integrating immunoassay with nanofibers[131]. Here, we describe an assay-on-a-tip platform (Figure 3.1) and demonstrate an *in-situ*, label-free technique to detect proteins inside single cells. Although electronic methods often suffer from surface charge screening by Helmholtz double-layer and are circumscribed to perform in environments with high ionic concentration such as cellular medium, our optical method is independent to ionic concentrations and sensitive to changes in refractive index vicinity to the gold surface, allowing our optical device to perform inside cells. Our method is widely applicable to other intracellular proteins as well, and have the spatial-temporal resolution to determine when, where, and under

27

what conditions specific proteins are created and disintegrated.

We describe a localized-surface-plasmon fiber-tip-probe (LSP-FTP) system, and demonstrate label-free, real-time detection of tumor suppressor p53 in single HeLa cells under ultraviolet radiation and under treatment with neocarzinostatin (NCS). Our results show that dynamic behavior of p53 varies depending on the stimulus; it shows a series of repeated pulses in response to neocarizinostatin treatment and sustained signaling in response to ultraviolet radiation[52]. In addition, we demonstrate continually monitoring levels of β-Amyloid and phosphorylated Tau in individual live human neuroblastoma cell (SY5Y) by employing the fiber tip probe (FTP) technique. Our results show that Aβ42 generation precedes Tau phosphorylation, which then facilitates the Aβ42 generation[77]. The FTP technique allows dynamically tracking the endogenous proteins (including their post-translational modifications) in single live cell, and is widely applicable to study pathogenesis of disease (e.g. Alzheimer's disease) and drug efficacies.

3.2   Sensing Principle

The LSP-FTP is a tapered optical fiber that has a sub-5 μm in length and sub-100 nm in diameter tip (Figure 3.1). One single gold nanorod (Nanopartz Inc.) was attached to the end of the tip, and its surface was functionalized with antibodies specific to the targeted analytes. The collective oscillation of the conductive electrons in

the gold nanorod couples strongly to polarized light in the visible wavelength range, generating a localized surface plasmon resonance (LSPR) signal.[9] The light, strongly localized on the surface of the gold nanorod, is sensitive to small perturbations of its optical mode near its surface[60,94,6]. Therefore, by monitoring the resonance shift of the LSPR, one can quantify the binding of analyte proteins to the sensor surface. Due to the nanoscale size of the tip and the immobilization of a gold nanorod at its end, the FTP allows minimal invasiveness when inserted into the cell membrane, keeping its cellular physiology intact.

A zoomed-in scanning electron microscope (SEM) image of the nanosize FTP tip attached with a single gold nanorod is shown in Figure 3.1a. A white light source (halogen lamp) was connected to the fiber and excited the LSPR of the gold nanorod at the tip (Figure 3.1b). The resonant scattering signal from a gold nanorod on the tip was visible to the naked eye (red glowing in Figure 3.2). The resonant scattering signal was collected via 50X objective and is coupled to a spectrometer (Princeton Instrument). Figure 3.2c shows the image on the spectrometer EMCCD when FTP was immersed in 10mM Phosphate Buffer Saline (PBS), pH 7.4. Spectrum profile analysis was performed by binning a few pixels around the bright spot to increase the signal-to-noise ratio. By fitting resonance spectrum with the Lorentzian profile, we found that the LSPR resonance of this individual gold nanorod was at 729nm, with quality factor of 10 (Figure 3.2c).
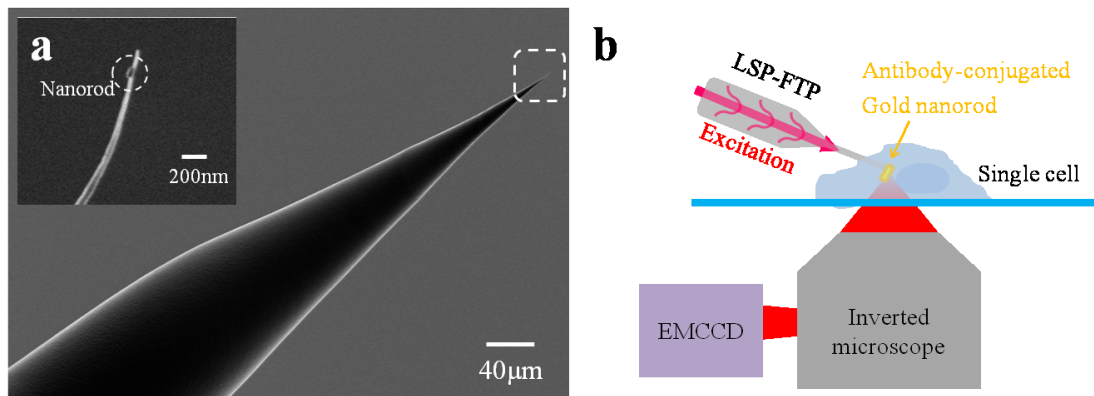
Figure 3.1: Gold nanorod Fiber tip probe (FTP). (a) Scanning electron micrograph (SEM) image of FTP. Inset shows a single gold nanorod attached to the FTP. (b) Schematic of the FTP setup. The probe, consisting of a gold nanorod immobilized at the sub-100nm FTP tip, is inserted into a single living cell at designated positions using a three-axis micromanipulator.
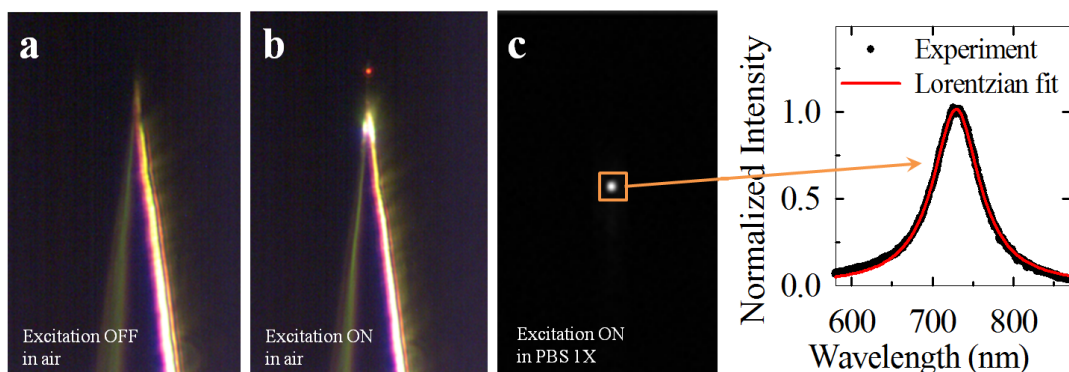
Figure 3.2: Demonstration of LSPR signal of a gold nanorod immobilized at an FTP tip. (a,b) Optical image of the LSP-FTP with excitation light source off (left) and on (right) in air. A red dot (right) corresponds to the LSPR of a gold nanorod. White-light form Halogen source was coupled into the fiber and used to excite the gold nanored at the fiber tip. (c) Image from the spectrometer CCD at the zeroth order grating (left) and a LSPR spectrum at the first order grating (right). This FTP was immersed in 10mM PBS.

3.3 Surface Functionalization and Fabrication

Gold nanorods were first functionalized with antibodies before conjugating at the tip of an FTP. 100 μL of a 20 mM solution of 11-mercaptoundecanoic acid (11-MUA, Sigma-Aldrich) prepared in ethanol was mixed with 1mL of the cetrimonium bromide (CTAB) capped gold nanorods (Nanopartz Inc.). The mixed solution was sonicated for 90 minutes at 55 °C [121]. After keeping the mixed solution at room temperature overnight, sedimentation of the rods was observed. The nanorods were re-immersed in a sonic bath and then the excess MUA was removed using centrifugation at 7000 rpm for 10 minutes. Then MUA-coated gold nanorods could be readily re-dispersed in water. These nanorods were dispersed on a thin cover glass and one nanorod was picked up by FTP mounted on the micromanipulator, as described in Section 2.5. For physiological experiment, FTP at this stage was assembled with a PDMS flow cell and functionalized with antibodies inside the microfluidic channel.

For intracellular biomarker measurement, the assembled LSP-FTP was incubated in 100mM 1-Ethyl-3-(3-dimethylaminopropyl)carbodiimide (EDC, Sigma-Aldrich) and 100nM anti-p53 (Santa Cruz) in 10mM PBS. EDC molecules react to the carboxyl groups of MUA molecules, which cap the gold nanorod, and form unstable easters, which react to the amine groups on the antibodies. Anti-p53 coated on the gold nanorod was then mounted on the three-dimensional piezo-stage for single live

cell interrogation and targeted measurement of intracellular p53.

3.4   LSPR Polarization Test

According to the Finite-difference-time-domain (FDTD) simulation with Lumerical, a gold nanorod supports LSPR when excited along its longitudinal axis (Figure 3.3). To investigate its LSPR dependency to its orientation, we tested LSP-FTP with two nanorods immobilized perpendicular to each other at an FTP tip (Figure 3.4). We used a gaussian halogen light for excitation through the fiber and used a linear polarizer for emission collection through the EMCCD. The emitted light polarized at different 90° featured the LSPR of an individual nanorod positioned 90° relative to each other. Spectrum analysis showed that LSPR peaks from both nanorods were at near 700 nm and differ by 50 nm. This is in consistent with the previous study of polarization-dependent gold nanorod spectrum[139].
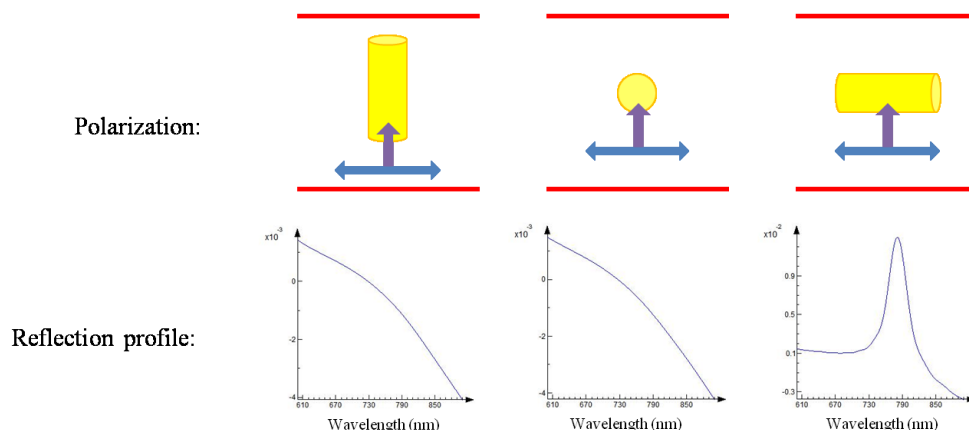
Figure 3.3: Finite-difference-time-domain (FDTD) simulation. Top three figures show configurations of a gold nanorod (75 nm in length and 25 nm in diameter, yellow cylinder), polarized white light source (blue arrow), and light propagation direction (purple arrow), and detectors (red lines). Bottom three plots show the reflection profile when the light polarized in blue axis impinges on a gold nanorod oriented as in the top figure. Reflection profile shows a resonance feature at 780 nm only when the light impinges parallel to the nanorod axis.
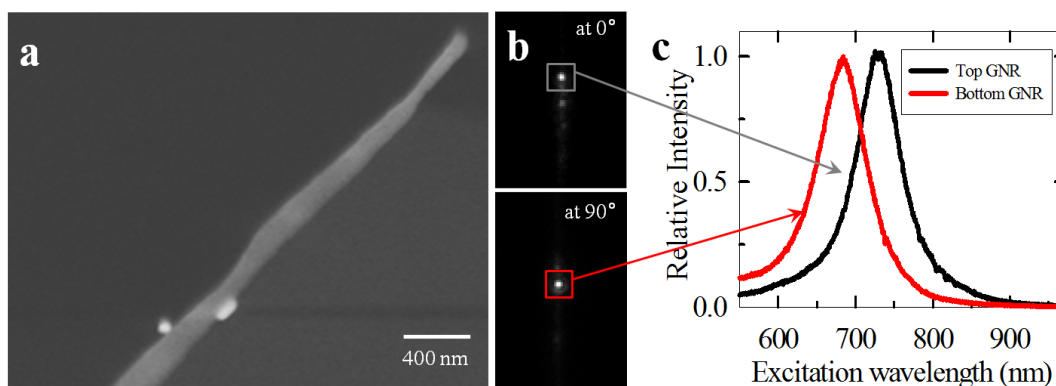
Figure 3.4: Gold nanorod (GNR) SPR polarization test. (a) SEM image of an FTP with two nanorods immobilized perpendicularly to each other. (b) EMCCD image at two different polarization of emitted light. Two GNRs individually glowed up at orthogonal polarizations. (c) SPR peaks of the two GNRs obtained after binning a few pixels around each GNR.

3.5 Measurements in Fluidic Channel

3.5.1 Microfluidics Setup

As shown in Figure 3.5, we used SU-8 (Shipley) to pattern 150 μm thick mold on top of a silicon substrate via photo-lithography. A 125 μm-wide channel was fabricated in the middle of the flow channel (2 mm by 10 mm) so that the fiber (125 μm in diameter at its stem) has a room to reside in the middle of the flow channel. The FTP was pasted onto an O_2-plasma-cleaned glass slide and the Polydimethylsiloxane (PDMS) channel was carefully assembled onto the glass slide.

For antibody conjugation on the nanorod surface, 100 mM EDC (Sigma-Aldrich) and 100 nM anti-p53 (Santa Cruz) in 10 mM PBS were flowed into the PDMS channel for 1 hour. The channel was then flushed with PBS 1X for 30 minutes to get rid of non-specific binding of anti-p53. The FTP was then flowed with 1X PBS solution containing biomarkers of various concentrations for physiological characterization.

3.5.2 Homogenous Refractive Index Test

To test the sensitivity of our LSP-FTP, we characterized it in an aqueous environment. First, we used FTP to detect different concentrations of glycerol (n=1.47) in water (n=1.33). We prepared solutions with 20%, 40%, 60%, and 80% of glyc-
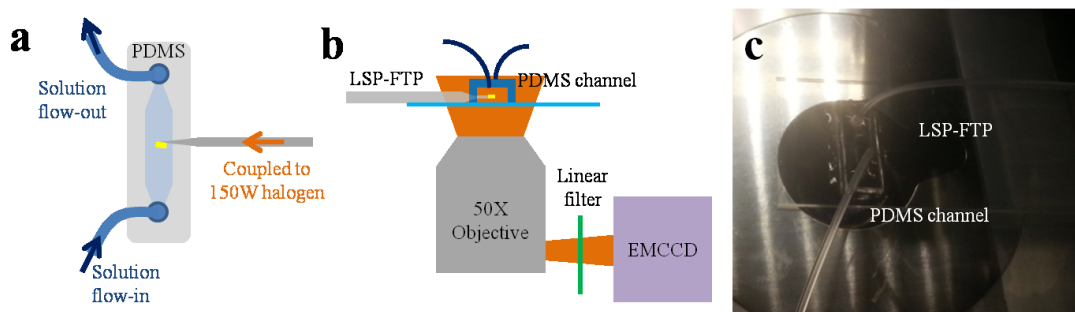
Figure 3.5: Schematics of microfluidic channel setup. ((a) top view, (b) side view) A PDMS channel has a groove in the middle where an FTP is placed and fixed inside the channel. The structure was aligned, assembled, and sealed with bio-compatible epoxy. (c) Image of an microfluidic setup placed on top of an inverted microscope.

erol, and injected them through a microfluidic channel. The FTP was inserted into this channel and sealed with epoxy. The LSPR signal, excited through the fiber coupled with halogen light source, was monitored with inverted microscope (Olympus IX71). Figure 3.6a shows representative spectra for each concentration. Increasing refractive index of the medium leads to a red-shift of the resonance due to the shielding of the surface charges by the polarization of the embedding medium. Figure 3.6b shows the real-time measurement of the LSPR peak wavelength (from Lorentzian fitting). Steps in the figure indicate the time when new concentrations reached the FTP. Figure 3.6c shows the resonance wavelength vs. refractive index of the solution. The LSPR shifted to longer wavelength in the presence of higher concentration of glycerol due to the increase in the refractive index of the solution[26]. Bulk index sensitivity of the FTP is defined as the resonance shift per unit refractive index change in the sur-

rounding medium. We found that the sensitivity of the current device was 187 ± 25 nm/RIU, significantly greater than that of the previously studied 39 nm diameter gold spheres (80 nm/RIU)[91]. Gold nanorods are also advantageous over gold spheres because of their reduced damping loss (thus higher Q-factor)[111].
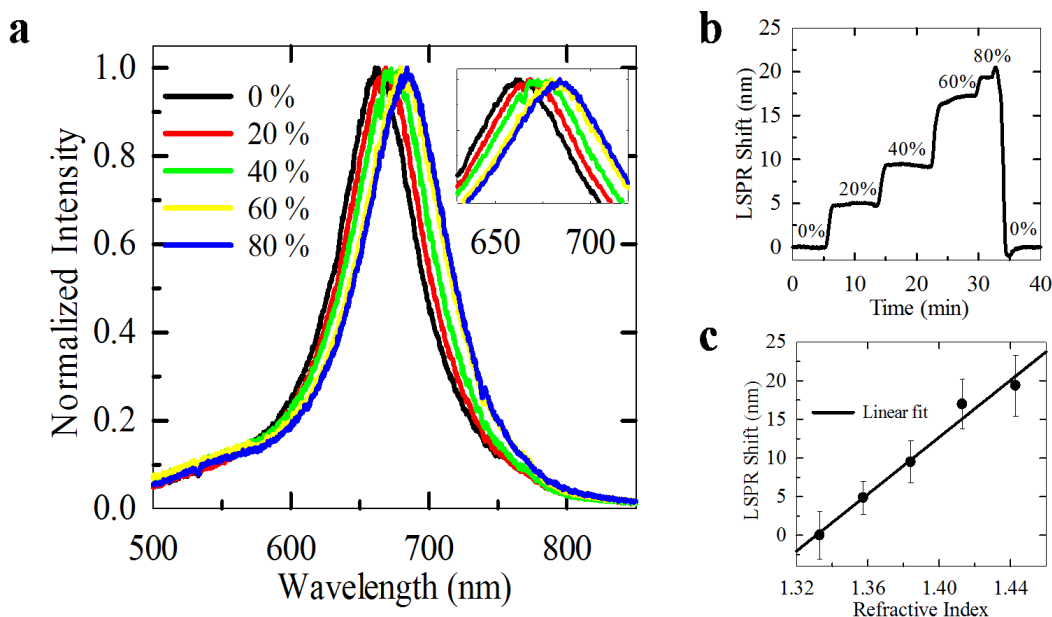
Figure 3.6: Characterization of the LSP-FTP in aqueous environment. (a) Normalized LSPR signal in various glycerol/water concentrations. Inset shows the zoomed-in view of LSPR peaks (b) Real-time monitoring of the LSPR when different concentrations of solutions are injected in the channel. The resonance wavelength is obtained by fitting LSPR signals to the Lorentzian equation. (c) Dependence of the LSPR position on the refractive indices of the solvents. A bulk index sensitivity of 187 ± 25 nm/RIU is obtained from linear fit. Error bar is the standard error from the measurements of five different nanorods (n=5).

3.5.3   Physiological Test

We used the LSP-FTP to detect different concentrations of biomarkers in 1X

PBS solution. The gold nanorod on the tip of the FTP was functionalized with p53

antibody (Santa Cruz sc-126). Different concentrations of p53 (Santa Cruz sc-4246)

in PBS were injected into the fluidic channel for 15 minutes, followed by washing

with pure PBS. Figure 3.7a and 3.7b shows the real-time response at several represen-

tative concentrations. LSPR shift of 5.13 nm was observed upon introducing 18.92

nM p53 solution. After washing with pure PBS at the 20th minute, the resonance de-

creased slowly, exhibiting the dissociation kinetics. A LSPR shift of 0.55 nm was ob-

served from 1 nM p53 solution, close to the detection limit of this system. The min-

imum discernible wavelength shift was 0.3 nm, estimated from the LSPR response

to pure PBS flowed for the first five minutes (black dashed line in Figure 3.7b). The

varying LSPR shifts subject to different levels of concentrations are shown in Figure

3c, a graph which was fitted with Langmuir equation. Error bar in this graph is the

standard error of five repeated experiments on different FTPs.

$$[A] + [L] \underset{k_b}{\overset{k_a}{\rightleftharpoons}} [AL] \tag{3.1}$$

As shown in Equation 3.1, Langmuir model displays the simplest situation of an

interaction between analyte (A) and immobilized ligand (L), where k_a and k_b are re-

spectively association and dissociation rate constants. It is equivalent to the Langmuir isotherm for adsorption to a surface. The Langmuir isotherm describes the dependence of the surface coverage of an adsorbed gas on the pressure of the gas above the surface at a fixed temperature[73]. The rate of adsorption (r_a) and the rate of desorption (r_d) are given by

$$\begin{cases} r_a = k_a p_A [S] \\ r_d = k_d [A_{AL}] \end{cases} \tag{3.2}$$

where p_A is the partial pressure of A over the surface, $[S]$ is the concentration of bare sites, $[A_{AL}]$ is the surface concentration of A. The equilibrium that exists between gas adsorbed on a surface and molecules in the gas phase is a dynamic state. At equilibrium, the rate of adsorption of molecules onto the surface is exactly counterbalanced by the rate of desorption of molecules back into the gas phase. It should therefore be possible to derive an isotherm for the adsorption process simply by equating the rates for these two processes ($r_a = r_d$), as following.

$$K_D = \frac{k_d}{k_a} = \frac{p_A [S]}{[A_{AL}]} \tag{3.3}$$

where K_D is the binding affinity. The concentration of all sites $[S_0]$ is the sum of the concentration of free sites $[S]$ and of occupied sites $[A_{AL}]$.

$$[S_0] = [S] + [A_{AL}] = \frac{[A_{AL}]K_D}{p_A} + [A_{AL}] = \frac{p_A + K_D}{p_A}[A_{AL}] \tag{3.4}$$

Defining the fraction of the surface sites covered with A as $\theta_A = [A_{AL}]/[S_0]$, Equation 3.4 can be rearranged to the Langmuir adsorption isotherm.

$$\theta_A = \frac{p_A \cdot [A_{AL}]}{p_A + K_D} \tag{3.5}$$

We can extract the affinity (K_D) by fitting to the Michaelis–Menten equation (Equation 3.6), a simple saturation binding model for equilibrium binding responses at different analyte concentrations[87].

$$R_{eq} = \frac{p_A \cdot R_{max}}{p_A + K_D} \tag{3.6}$$

where R_{eq} is the SPR peak shift at equilibrium corresponding to the analyte concentration (p_A), and R_{max} is the maximum SPR peak shift when the ligands on surface are saturated by its corresponding bound analytes ($[A] \gg K_D$). The binding affinity (K_D) of p53 from anti-p53 is 5.5 nM, in good agreement with published results obtained using commercial instrument[62]. Figure 3.8 shows the LSPR shifts vs. concentration of p53, measured with four other FTP devices. The binding affinity of p53 to anti-p53 was measured to be 5.5 nM, 4.2 nM, 7.1 nM, and 5.7 nM respectively. Variance in the binding affinity may originate from size difference of nanorods and different

39

molecular assembly during surface functionalization.

To investigate the specificity of the system, we functionalized the FTPs with antibodies of either tumor suppressor p53 or tumor necrosis factor (TNF-α) and used these FTPs to detect p53 and TNF-α (Figure 3.7d). When the FTP was functionalized with anti-p53, it could detect p53 in both pure PBS and PBS with concentrated Bovine Serum Albumin (1% BSA) as background. On the other hand, the sensor was not sensitive to TNF-α, a mismatched antigen-antibody pair. The FTP functionalized with anti-TNF-α also showed high specificity to TNF-α only. This demonstrates that the LSP-FTP shows high specificity to the targeted protein and non-specificity to the other proteins. Because the LSPR of a nanorod has exceptionally smaller optical mode volume[21] (on the order of the physical dimension of the nanorod) compared to other optical resonators[128], the sensor is sensitive only within a few nanometers from its surface and is insensitive to untargeted proteins[138].
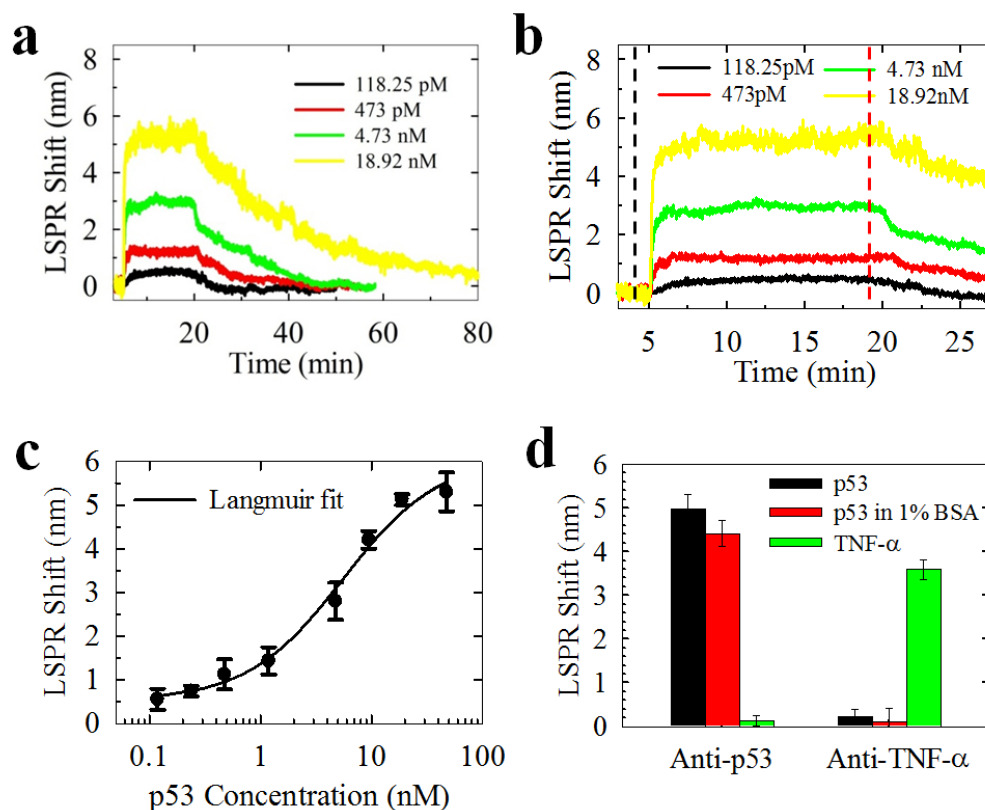
Figure 3.7: Characterization of the LSP-FTP in physiology condition. (a) Real-time measurement of LSPR shifts at various p53 concentrations. Binding kinetics happened at much faster rate than unbinding kinetics. (b) Portion of (a) up to 25 min. In all cases, the blank PBS was injected into the fluidic channel for the first 5 minutes (before black dashed line). Different concentrations of p53 in PBS were injected into the channel for 15 minutes, followed by additional PBS wash step to observe dissociation of p53 from its antibody (after red dashed line). (c) LSPR shift vs. p53 concentration. Binding affinity of 5.4 nM was extracted from the Langmuir fit (Equation 3.6). Error bar is the standard error (n=5). (d) Specificity test of LSP-FTP sensor. Two LSP-FTPs were coated with anti-p53 and anti-TNF-α respectively, and both sensors were used to detect p53, p53 in 1% BSA, and TNF-α(n=5). Significant LSPR shift only occurred when coated antibodies paired correctly with their antigens, thus demonstrating high sensor specificity. High specificity was retained when the p53 antigens were in 1% BSA background.

41
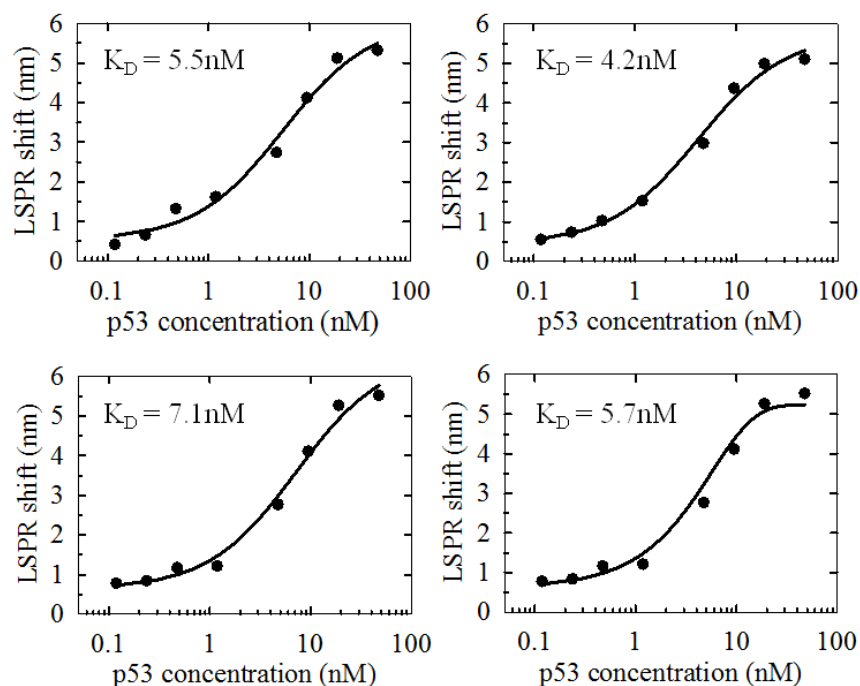
Figure 3.8: Binding curve of p53 obtained from physiological characterization in microfluidic channel. Four curves were obtained from four different FTP samples.

3.5.4 Comparison with Data from UV-Vis Spectrometer

The surface functionalization procedure was verified using UV-Visible spectrometer (Jasco Inc.). We measured the change of the absorption spectra at each step of the functionalization procedure. First, MUA-capped nanorods were mixed with 100 mM EDC (Sigma-Aldrich) and 100 nM p53 antibody (Santa Cruz) in PBS 1X (pH 7.4) for 1 hour. The resulting nanorods were then collected by centrifugation at

5000 rpm for 5 minutes and suspended again in a buffer containing 5 mM CTAB. After three rounds of vigorous washing, the collected nanorods were sonicated in 5 mM CTAB solution for 10 minutes. As shown in Figure 3.9c, after the 11-MUA coating, a red-shift of 5-7 nm in the longitudinal peaks was clearly identifiable, indicating the alkanethiol self-assembled-monolayer (SAM) formation. A further red-shift of the surface plasmon resonance peak was observed due to the antibody functionalization.

Different concentrations of p53 protein were added to the anti-p53 modified gold nanorod solution. Each solution was vortexed for 5 minutes under room temperature before UV-Visible spectrum measurement. In order to minimize bulk refractive index change, we mixed the nanorod solution with a minimal volume from original p53 stock solution with a high protein concentration (50 µg/mL). 1 µL of the p53 stock solution was added into 1 mL of gold nanorod to obtain 1 nM p53. Also, the concentration of p53 was ensured to be sufficiently higher than that of nanorods; the nanorod solution has $10^{10} mL^{-1}$, while 1 nM p53 has $10^{12} mL^{-1}$.

Figure 3.9d shows the resonance shift v.s. p53 concentration and the fitting curve by Langmuir equation. Binding affinity K_D =4.3 nM was obtained from fitting. We note that the resonance spectrum from UV-visible spectrometer is an ensemble measurement from the gold nanorod solution, and thus shows inhomogeneous broadening than the spectrum obtained from the single nanorod that was attached to the FTP (Figure. 3.9b).
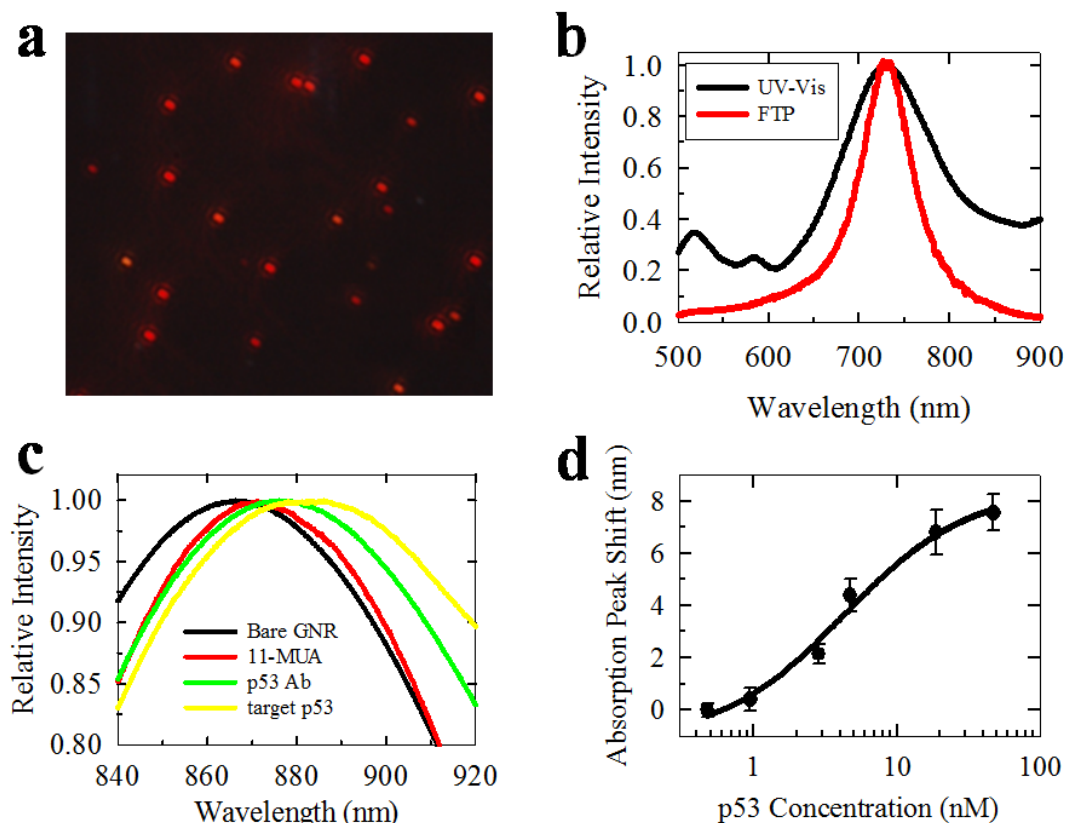
Figure 3.9: Characterization of surface functionalization with UV-Vis Spectrometer. (a) Darkfield microscopy images of gold nanorods. LSPR of the gold nanorod is roughly at 700 nm which glows in red, and each red glowing corresponds to an individual gold nanorod. (b) Scattering spectra of a single gold nanorod on a glass substrate (red) measured via EMCCD spectrometer and the extinction spectrum of an ensemble of gold nanorods (GNRs) measured via UV-Vis spectrometer (black). The ensemble spectrum from nanoparticles with a distribution of size and shapes exhibited heterogeneous broadening compared to the single Lorentzian peak observed from each resonance of a single nanoparticle. (c) UV-Vis absorption spectra of gold nanorods at each functionalization step. Functionalization of GNRs introduced a red-shift in the longitudinal plasmon peak. (d) Binding curve of p53 obtained from UV-Vis Spectrum analysis. Error bar is the standard error (n=3).

3.5.5   Regeneration Process

Due to the slow unbinding kinetics for some targeted biomarkers (Figure 3.7a) and the non-specific binding of untargeted proteins to the LSP-FTP surface in the complex cell medium, the sensor may have error when quantifying concentration of targeted biomarkers in the complex cellular medium. We demonstrated that the LSP-FTP biosensor can be efficiently and repeatedly regenerated with glycine solution (pH = 2.5 tuned with hydrogen chloride).

For this experiment, the FTP was functionalized with Tau protein antibodies (anti-Tau-PS262, sc-32828, Santa Cruz). In Figure 3.10, the baseline represents FTP in the complex cell culture medium without fetal bovine serum (DMEM F-12 Medium, 100 U/mL penicillin and 100 ug/mL streptomycin). 100nM Tau protein (Tau-PS262, sc-32828p, Santa Cruz) was mixed into the cell culture medium and was repeatedly detected with FTP, following the sequence of baseline, 100 nM Tau protein and re-generation. Figure 3.10a shows that FTP repeatedly goes back to the baseline value after regeneration, and 100 nM Tau protein was consistently measured. Regeneration solution was glycine with pH 2.5 tuned by hydrogen chloride acid. The regeneration step removed only the Tau proteins non-covalently bound to the surface, while the antibodies remained functional.
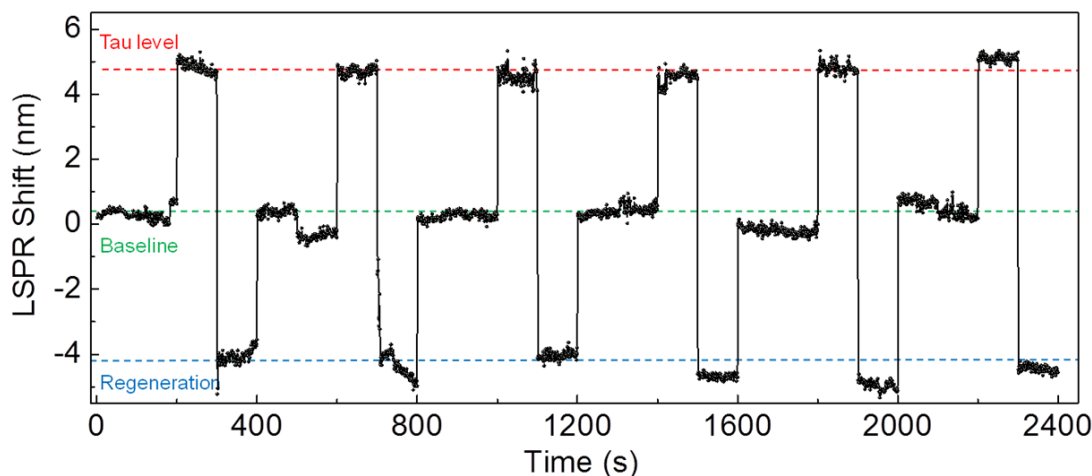
Figure 3.10: Regeneration of antibodies bound on the LSP-FTP surface. Repeated measurements in the regeneration process. The regeneration solution is glycine with pH = 2.5 (tuned with hydrogen chloride acid), baseline is the cell culture medium, and detected solution is 100 nM Tau protein mixed into the cell culture medium.

3.6   Measurement in Intact Live Cells

The FTP offers a unique three-dimensional nanoscale form-factor; thus, it is an ideal, minimally-invasive bioprobe of cells. LSP-FTP with a antibody-functionalized gold nanorod immobilized at its tip is used to demonstrate *in-situ*, label-free measurement of intracellular biomarkers in intact live cells. We tested the LSP-FTP device to target different biomarkers and function in different cells multiple times to prove its robust repetitivity and reproductivity.

3.6.1 Tumor Suppressor p53 Dynamics in HeLa Cells

We demonstrate how intracellular tumor suppressor p53 in HeLa cells dynamically react to ultra-violet (UV) exposure and neocarzinostatin (NCS) drug treatment. Cells experience p53 pulses in response to recovery from double-strand DNA breaks (NCS drug treatment), and cells that undergo senescence experience sustained p53 signaling (UV exposure)[99]. In order to minimize the invasiveness to the cell, anti-p53 functionalized LSP-FTP was inserted in and retracted out of the cell every 30 minutes. During each measurement, we first inserted the FTP into the cytoplasm of the cell, incubated for 5 minutes, retrieved the FTP out of the cell, and measured its LSPR in the cell culture medium adjacent to the cell of interest. This process was conducted to minimize the scattering background from the cytoplasm when FTP was inside the cell, as well as to wash off the non-specific bindings of other proteins inside the cell. LSPR measurement was immediately taken after the retraction to prevent the unbinding of p53 from anti-p53. After the FTP was inserted into the cell, we were able to clearly observe a single gold nanorod glowing inside the cell and gradually dimming down after a few minutes (Figure 3.11a). This dimming behavior is attributed to the scattering background from the possible non-specific binding of cytoplasmic proteins onto the nanosize tip, evidencing that the insertion of the FTP into the cytoplasm.

Before preforming the aforementioned measurement, the intensity of UV light

source was first calibrated. Live HeLa cells were exposed to either different dosages of UV light or different concentrations of NCS. The FTP experiments were performed immediately after the treatments. The results of our experiment indicate that the different stresses triggered different temporal responses of p53. As shown in Figure 3.11b, we quantified the dynamics of p53 in individual cells in response to different UV exposure and observed a sustained increase in amplitude and duration in proportion to the increase in UV dose. This dose-dependent, sustained escalation of p53 in relation to UV is a clear contrast to the repeated pulses in response to NCS. The amplitude and duration of individual p53 pulses do not depend on the NCS dose. As a control experiment, we performed the same procedure on an intact HeLa cell. As shown in Figure 3.11b, the intracellular p53 level remained constant. This consistency also indicates that the FTP is minimally invasive and has little effect on the cell physiology. p53 slowly dissociates off the sensor when the background p53 concentration is decreased, but full dissociation requires relatively long time (Figure 3.7a). The excess un-dissociated p53 adds to residue LSPR shifts from the sensor, and FTP may give higher LSPR shifts than the actual intracellular p53 concentration when p53 is down regulated. This problem can be remedied by regenerating the sensor or by using alternative affinity probes, such as aptamer or cellular receptors.

Our results agree with the previous studies of p53 using fluorescent microscopy and western blot[64,99,15]. Current FTP technology offers a range of comparable advantages. First, it is a label-free technology, which precludes the interference of labels

with biomarkers. Second, it is capable of interrogating single cells intact, without the need of cell harvest and cell lysis. Third, it allows the quantification of its real-time intracellular dynamics. By referring to the measurement in physiological environment, we assert that the p53 concentration can increase up to the order of 10 nM under external stress (UV illumination).

Similar experiments were repeated to demonstrate its ability to repeat intracellular p53 detection. For every measuerment, different FTPs and different cell batches were used. FTP was functionalized with anti-p53. HeLa cells were exposed to either 10 J/m^2 of ultra-violet (UV) light or 400 ng/mL of NCS drug. FTP was inserted into the cytoplasm of the cell, incubated for 5 minutes, and then retrieved out of the cell and measured in the cell culture medium. This insertion, incubation and measurement were repeated every 30 minutes. Figure 3.12a-c show p53 response to UV exposure. Its concentration increases with respect to time and plateaus after about 4-5 hours. Figure 3.12d-f show p53 response to NCS drug. In clear contrast, p53 concentration shows repeated pulse behavior.
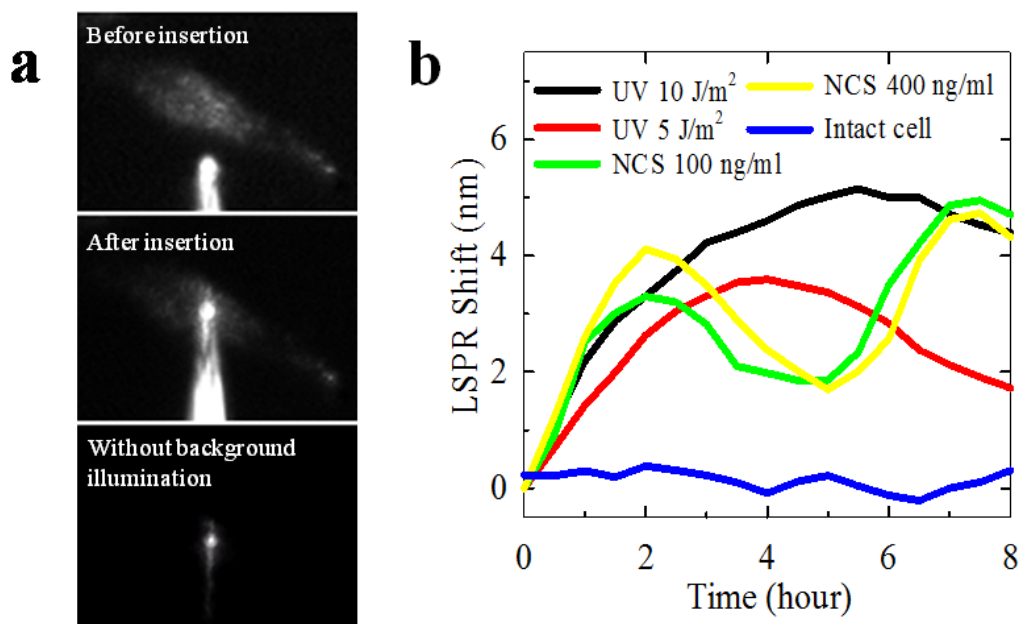
Figure 3.11: Intracellular p53 detection in a single living HeLa cell with FTP. (a) Sequence of EMCCD images of an FTP penetrating a single HeLa cell, viewed from below. The FTP was first positioned outside the cell with its tip lying slightly flat against the petri dish substrate. It was then punctured into the side of the cell. Without background illumination, we can clearly see the LSPR signal from the nanorod glowing inside the cell. (b) p53 dynamics in the intact, UV exposed and NCS treated HeLa cells. The p53 showed sustained concentration increase under UV, and pulsed oscillation under NCS.
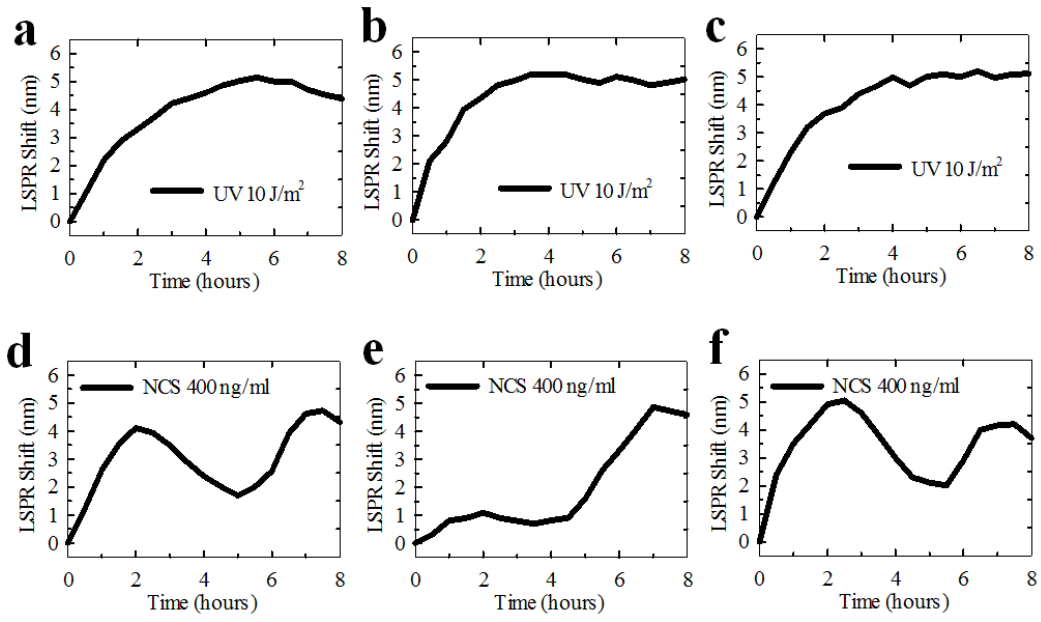
Figure 3.12: p53 dynamics inside an intact HeLa cell in response to UV illumination and NCS drug. (a-c) Intracellular p53 dynamics from HeLa cells exposed to UV (d-f) Intracellular p53 dynamics from HeLa cells treated with NCS drug.

3.6.2 β-Amyloid and Tau Dynamics in Live Neurons

Aβ accumulation (amyloid plaques) and Tau phosphorylation (neurofibrillary tangles) are the pathological hallmarks of Alzheimer's disease. However, there has been a long standing debate on the dynamic relations between Aβ and Tau proteins, partially due to the lack of a tool to track protein dynamics in individual live neurons. Aβ hypothesis posits that generation of Aβ triggers cascade of neurotoxic events, in particular, hyperphosphorylation of Tau that leads to neurofibrillary tangles[47]. Tau hypothesis suggests that Tau phosphorylation leads to inflammatory cascades and Aβ overproduction, and eventually neuronal death[49,28]. Debates still remain on the precedence and causal relations between Aβ generation and Tau phosphorylation[110], partially due to the lack of a technique to simultaneously measure the dynamics of Aβ and phosphorylated Tau proteins in the same individual neuron over time at their native conditions. Here, we demonstrate direct observation of dynamic change of Aβ42 and phosphorylated Tau (at serine 262) proteins in single living neuroblastoma cells using the nanoplasmonic fiber tip probe (nFTP) technology[77]. Our measurements suggest a hierarchical and circular pattern between Aβ generation and Tau phosphorylation: Aβ generation precedes and leads to Tau phosphorylation, and phosphorylated Tau also promotes Aβ generation.

The nFTP device comprises of a nanoscale optical fiber with a single gold nanorod biosensor on its tip (Figure 3.1). The gold nanorod biosensor presents a localized sur-

face plasmon resonance (LSPR) which quantifies proteins that bind on its surface. We designed a mechanically revolving dual-FTP device (Figure 3.13a) with a home-built revolving cylinder, 120º rotatable that can hold three metal fiber chucks (two are shown). Each chuck held one nFTP device. In our experiment, we used two nFTPs functionalized with Aβ42 antibody (ab10148, Abcam) and phospho-specific Tau antibody (anti-Tau-PS262, sc-32828, Santa Cruz), respectively. The device was controlled by the piezoelectric stages and could be precisely manipulated to puncture individual cells under a conventional microscope (Figure 3.13b).

Glycine solution (pH 2.5 tuned with hydrogen chloride) was used to unbind proteins off the antibodies, while preserving the antibodies on the sensor. 1% BSA solution was used to block the non-specific binding, which was found to be an essential step to suppress non-specific binding in the intracellular measurements. One measurement cycle is the following: (a) The FTP sensor was sequentially incubated in the regeneration and blocking solution. (b) It was then brought in proximity to the cell. (c) The baseline spectra were first taken outside of the cell. (d) The FTP was then inserted into the cell, incubated for 2 mins and retrieved out of the cell. (e) The signal spectra were taken at the same focal position as the baseline spectra. LSPR shift between the baseline and signal spectra induced by the proteins captured by the antibodies, quantified the intracellular protein concentrations. This regeneration-blocking-baseline-insertion-incubation-retreat-signal completes one measurement cycle, and can be repeatedly performed on the live cell.

The sensitivity and dynamic range of the nanoscale fiber tip probe (nFTP) biosensor can be tested by mixing different concentrations of Tau-PS262 proteins (Santa Cruz, sc-32828p) into the cell culture medium. The nFTP biosensor was functionalized with anti-Tau-PS262 (sc-32828, Santa Cruz). As shown in Figure 3.14, the sensor has a detection range from 0.5 nM to 0.5 M, equivalent to approximately 300 to 300,000 copies of proteins in the volume of a typical cell (roughly 10 μm size). This dynamic range of proteins falls in the biologically relevant concentration of intracellular proteins[135]. The nFTP biosensor functionalized with anti-Aβ42 (ab10148, Abcam) was used for Aβ42 detection. Figure 3.14b and 3.14c showed the localized surface plasmon resonance (LSPR) shift at different concentrations of Aβ42 and Tau-PS262 mixed into the cell culture medium [without fetal bovine serum (FBS)]. The nFTP biosensor was regenerated between different concentrations. The affinity between Aβ42 and its antibody was 44 ± 12 nM, and the affinity between Tau-PS262 and its antibody was 16 ± 4 nM.

To further test the repeatability of nFTP technique, we measured both Tau-PS262 and β-Amyloid levels in the wild-type neuroblastoma SH-SY5Y cell, Tau over-expressed SH-SY5Y cell (SH-SY5Y-Tau cell), mouse cortex neuron and Tau knock-out mouse cortex neuron (Neuron-Tau$^{-/-}$). All these cells were first treated with isoflurane to trigger Tau-PS262 generation. Results summarized in Figure 3.15 showed clear difference in Tau-PS262 expressions between different cell types, while similar levels of β-Amyloids were observed as control. LSPR shifts can be converted to protein con-

centrations by calibrating nFTP using known concentrations of Tau-PS262 solutions.

To study Aβ and Tau-PS262 dynamics simultaneously in the same cell, we built the mechanically revolving dual-nFTP and functionalized the gold nanorod surfaces with Aβ antibodies and Tau-PS262 antibodies, respectively. Inhalation anesthetic isoflurane has been shown to induce Aβ accumulation[136] and Tau phosphorylation (increase in Tau-PS262 levels without significant changes in total Tau levels)[34], which provides a clinically relevant tool to simultaneously induce both Aβ generation and Tau phosphorylation. Prior to single cell measurements, each FTP was tested in a pre-mixed solution with either Aβ42 or Tau-PS262 proteins in the cell culture medium. The positive spectrum shift verified the successful functionalization of antibodies on the sensor surface.
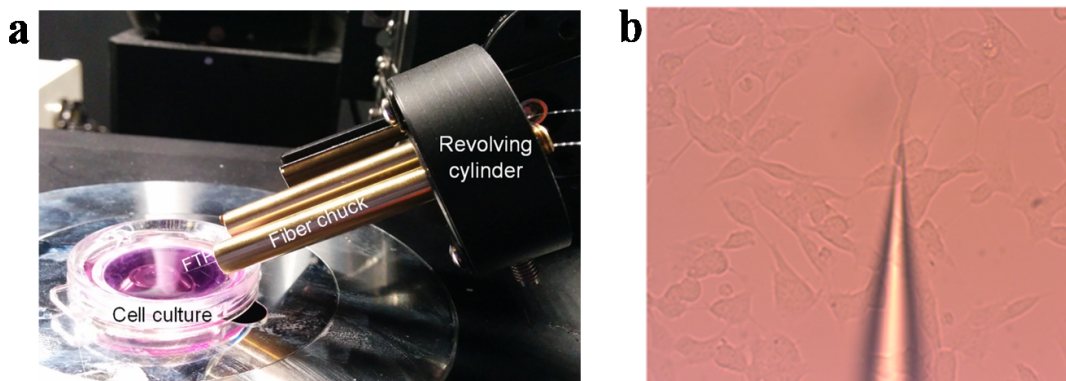
Figure 3.13: Setup for intracellular measurement of Tau and Aβ proteins with nFTP. (a) Photograph of a mechanical revolving dual-nFTP device. Each fiber chuck holds 125 μm optical fiber (Thorlabs), and can be rotated by 120º with the revolving cylinder. (b) Microscope image (20X) of the FTP inserting into an individual live human neuroblastoma cell (SY5Y).
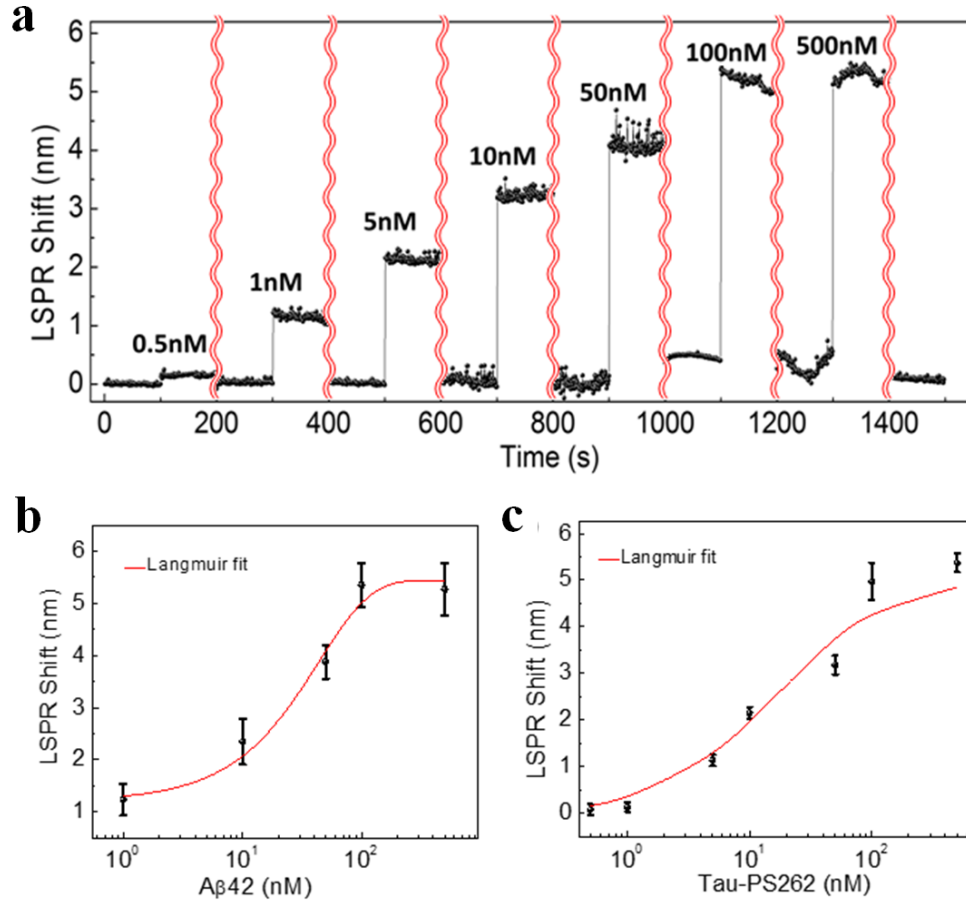
Figure 3.14: Physiological measurement of label-free Tau-PS262 with nFTP. (a) 0.5, 1, 5, 10, 50, 100, 500 nM Tau-PS262 in the cell culture medium (without FBS) were prepared, and sequentially tested. At each concentration, 1,000 spectra were measured. The nFTP was regenerated between two different concentrations The regeneration processes are replaced by red squiggly lines. (b and c) LSPR shift at different concentrations of Aβ42 (b) and Tau-PS262 (c) solutions fitted with the Langmuir equation. The affinity between Aβ42 and its antibody is 44 ± 12 nM (n=3). The affinity between Tau-PS262 and its antibody is 16 ± 4 nM (n=3).
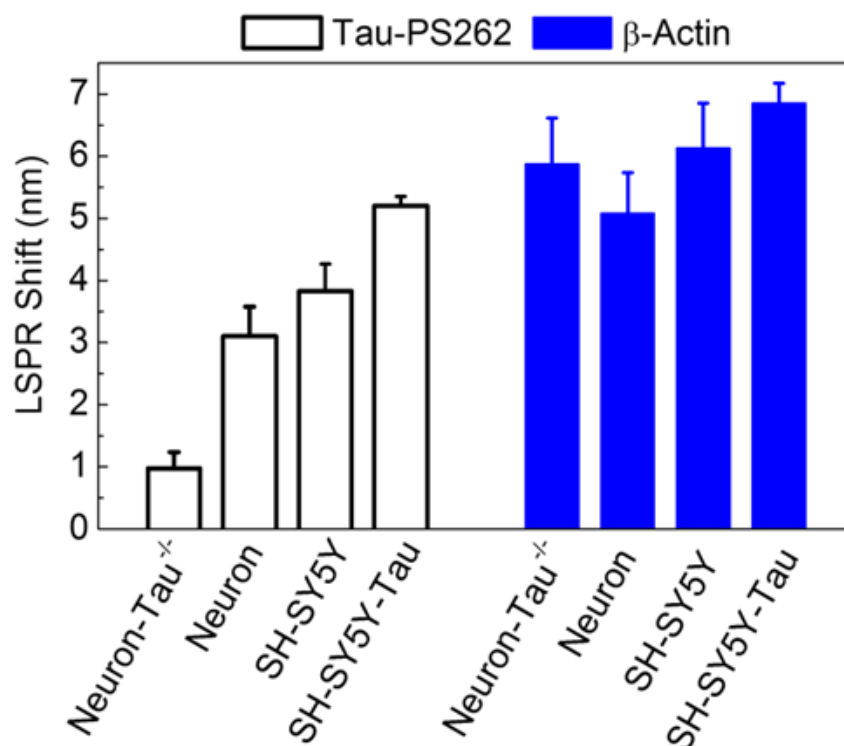
Figure 3.15: Characterization of nFTPs in different cell types. The nFTP sensors, function-alized with anti-Tau-PS262 (sc-32828, Santa Cruz) and anti-β-Amlyoid(ab13822, Abcam), and were employed to measure Tau-PS262 and β-Actin proteins in different cell types after the cells were treated with isoflurane. The error bar is the standard error (n=3). All cells had different concentrations of Tau-PS262 and β-Actin proteins

We first performed a control experiment in the SH-SY5Y-Tau cells without the treatment of isoflurane. As shown in Figure 3.16a, neither Aβ nor Tau-PS262 levels increased under this control condition. Each data point in all of the plots represents the averaged value of three consecutive measurements (n=3) in the same cell. Next, we treated SH-SY5Y-Tau cells with 2% isoflurane for two hours, and then measured Aβ and Tau-PS262 levels simultaneously every two hours up to 12 hours. In contrast to the control condition, isoflurane significantly increased the Aβ and Tau-PS262 levels (Figure 3.16b). Moreover, the time to reach a 50% increase in Aβ level (approximately 4 hours) was less than that needed for a 50% increase in Tau-PS262 level (approximately 7 hours). These data suggest that Aβ generation may precede Tau phosphorylation.

Next, we set out to study whether Aβ generation and Tau phosphorylation could interfere with each other. We treated the SH-SY5Y-Tau cells with 0.5 μM γ-secretase inhibitor (L-685,458, Sigma L1790) one hour before the isoflurane treatment, which has been demonstrated to suppress Aβ accumulation[136]. In the same cell, we observed simultaneous decrease in the Tau-PS262 level (Figure 3.16c). We also used 0.5 μM Tau phosphorylation inhibitor (K252a, Abcam ab120419) to treat SH-SY5Y-Tau cells for one hour before the isoflurane treatment, which has been shown to suppress Tau-PS262 generation[74,53]. In the same cell, we observed Aβ level first increased but finally reduced after 10 hours (Figure 3.16d). These data indicate that inhibition of Tau phosphorylation led to a partial reduction in Aβ levels. Taken to-

gether, these results suggest a hierarchical and circular pattern between Aβ generation and Tau phosphorylation: Aβ42 generation precedes Tau phosphorylation (at size S262). Suppression of Aβ42 generation suppresses Tau-PS262. Suppression of Tau-PS262 partially suppresses Aβ42, indicating a hierarchical relation between Aβ42 and Tau-PS262. Therefore, when Tau phosphorylation is inhibited by K252a, Aβ42 level still increases for the first 10 hours, and decreases at a later stage.

Our results are the first direct measurement of intracellular Aβ generation and Tau phosphorylation in individual live cell. Pending further demonstrations, our technique could be widely applicable to study disease pathways and test drug efficacies at cellular level, and can complement the limitation of fluorescent labeling techniques[79,142,29] and other techniques to detect protein phosphorylations[82,30,113]. Limitations of the current technique include low throughput to interrogate a large amount of cells, which can be improved by multiplexing single fibers into fiber arrays.
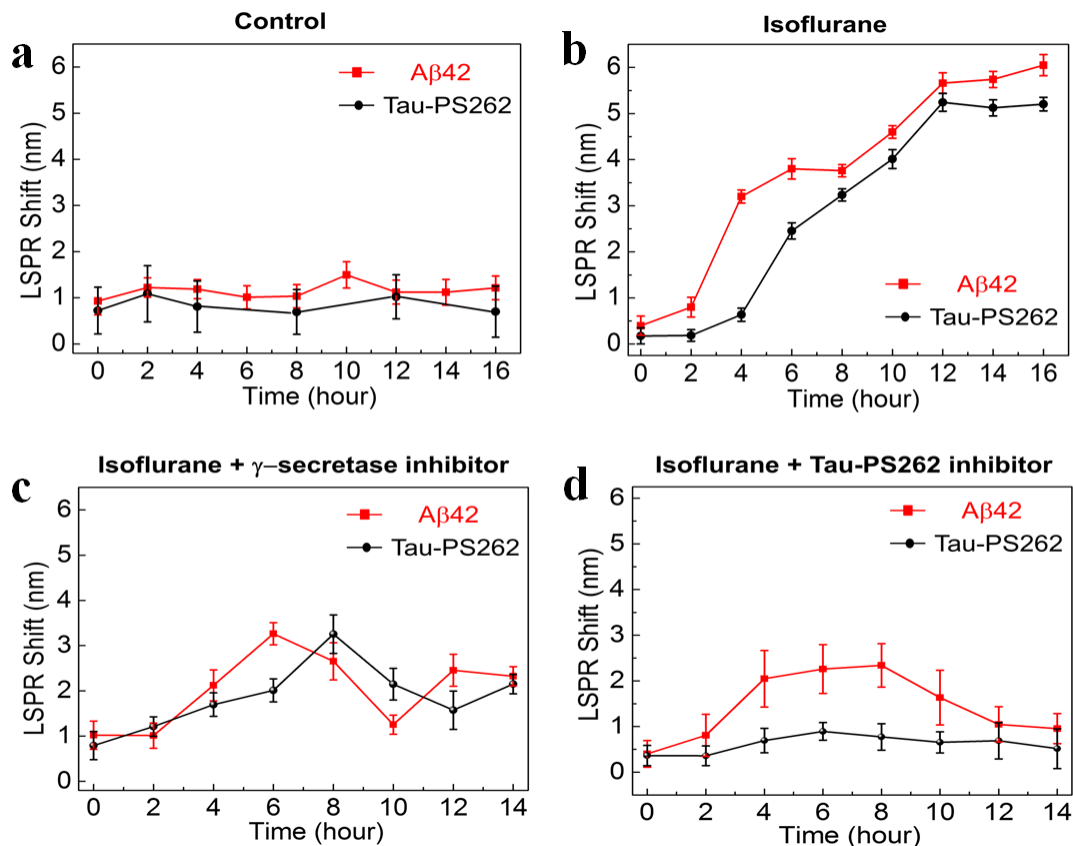
Figure 3.16: Aβ42 and Tau-PS262 dynamics. (a) Aβ42 and Tau-PS262 levels were monitored in the same SH-SY5Y-Tau cell when no isoflurane was applied (control condition). (b) Aβ42 and Tau-PS262 levels were monitored after the treatment of isoflurane in the SH-SY5Y-Tau cell up to 16 hours. (c, d) Dynamic Aβ42 and Tau-PS262 levels in SH-SY5Y-Tau cells, which were pre-conditioned with (c) 0.5 μM γ-secretase inhibitor or (d) phosphorylation kinase inhibitor K252a prior to the isoflurane treatment. For all data points, we measured three times with the same FTP on the same cells, and the error bars are from the three replicated measurements.

3.6.3 Cell Culture, Lysis, Drug Treatment, and Immonoblot

For p53 measurement, human cervix epithelial HeLa cells (American Type Culture Collection, ATCC) were cultured at 37 °C in DMEM F-12 Medium supplemented with 10 % fetal calf serum, 100 U/mL penicillin, and 100 ug/mL streptomycin.

We harvested cells, lysed, and measured the total protein concentration (10 mg/mL) by Bradford assay (Thermo Scientific). We used human p53 protein (Santa Cruz) as control protein to test the validity of antigen and antibody. Proteins were then separated by electrophoresis on 4–20 % Mini-PROTEAN TGX Stain-Free precast gels (Bio-Rad), and transferred to PVDF-membrane (Bio-Rad) by electroblotting. The membrane was incubated with primary p53 monoclonal antibody (Santa Cruz) overnight, washed, and incubated with secondary antibody for 2 hours. Protein levels were then observed by chemoluminiscence after adding SuperSignal West Pico Working Solution (Thermo Scientific) for 5 minutes. Both commercial p53 and intracellular p53 existing inside the lysate of HeLa cells paired well to the commercial anti-p53 (Figure 3.17a). We used western blot to verify the efficacy of the phosphorylation kinase inhibitor K252a (Figure 3.17b). Isoflurane was treated for 6 hours in Figure 3.17, as compared to 2 hours in nFTP experiments. We were not able to observe significant difference between the control and isoflurane group without increasing the isoflurane dosage from 2 hours to 6 hours. K252a concentration of 3 μM was used.

For Aβ and Tau measurement, The wide-type [American Type Culture Col-

61

lection (ATCC), Manassas, VA, CRL-2266] and Tau over-expressed (generous gift of Dr. Luc Buee from Inserm UMR1172, France) human neuroblastoma cells (SH-SY5Y cells) were cultured at 37 °C in a humidified incubator with 5% CO_2 in DMEM F-12 Medium (ATCC, 30-2006) supplemented with 10% fetal calf serum (ATCC, 30-2005), 100 U/ml penicillin and 100μg/ml streptomycin (Sigma, St. Louis, MD, P4333), 1% (v/v) nonessential amino acids (Sigma, M7145) and 2 mM L-Glutamine (Sigma, 59202C).

For anesthetic isoflurane treatment, Twenty-one percent oxygen, 5% carbon dioxide, balanced nitrogen, and 2% isoflurane were delivered from an anesthesia vaporizer to a sealed plastic box in a 37°C incubator containing plates seeded with the SH-SY5Y-Tau cells for two hours. Twenty-one percent oxygen, 5% carbon dioxide and balanced nitrogen without isoflurane were used in the control condition.
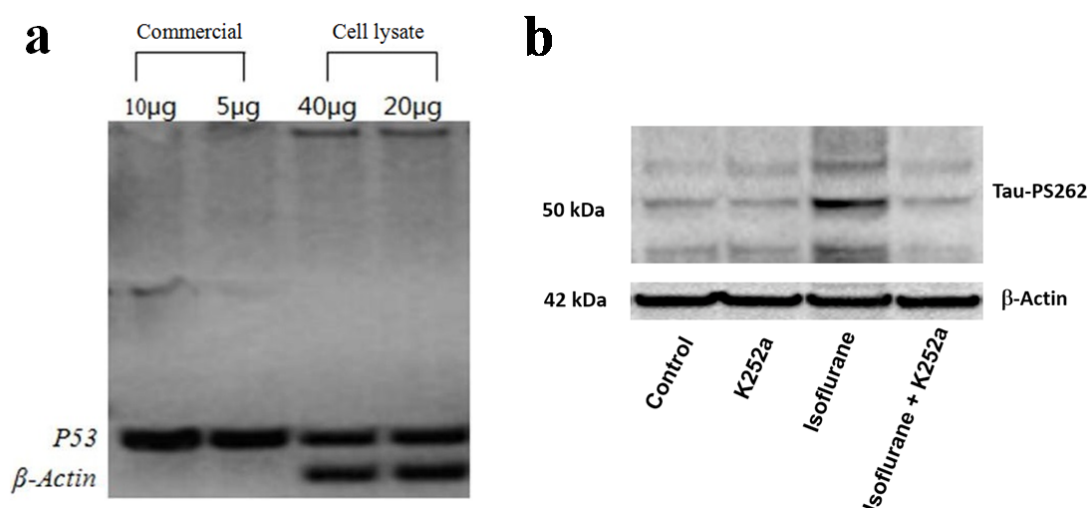
Figure 3.17: Western-blot analysis. (a) Western-blot analysis of expression of 5 and 10 μg of commercial p53 and 20 and 40 μg of cell lysates from HeLa cell, where β-actin was used as control for loading. Commercial anti-p53 paired well with both commercial and intracellular p53. (b) Western blot measures Tau-PS262 protein. Tau protein was expressed only when the cells were treated with isoflurane.

3.6.4 Cell Viability Test

We assessed the cell membrane integrity, enzymatic and metabolic activity after the cell was punctured by nFTP once every hour, consecutively for 12 hours. First, we used the cell viability/cytotoxicity assay (L3224, Invitrogen). 2 μM calcein-AM and 4 μM ethidium homodimer-1 (ethD-1) were applied to the cell. After incubating for 40 minutes, cell medium was replaced by 1 mL Dulbecco's phosphate-buffered saline (DPBS) and cells were imaged under fluorescent microscope. The calcein-AM is a green fluorescent dye that indicates intracellular esterase activity. EthD-1 is a red fluorescent dye that stains nucleic acid, indicating a compromised cell membrane. As shown in Figure 3.18a, the dash-circled cell was punctured by the nFTP and showed green fluorescence and no red fluorescence. The solid-circled cell, punctured by a microscale fiber showed red fluorescent color and no green fluorescence. These results indicated that puncturing by the nFTP (but not microscale probe) preserved esterase activity and membrane integrity.

Next, we performed cell vitality assay (L34951, Invitrogen). 500 nM C12-resazurin and 10 nM SYTOX DNA binding dye were applied to the cell and incubated for 15 minutes. Reduction of C12-resazurin to red-fluorescent C12-resorufin indicates active metabolic condition. SYTOX is a cell-impermeant, green-fluorescent nucleic acid stain that indicates compromised cell membrane. In Figure 3.18b, the dash-circled cell was punctured by the nFTP and the solid-circled cell was punctured by a mi-

croscale probe. The presence of red fluorescent color and absence of green color in the dash-circled cell indicated that the nFTP (but not microscale probe) puncturing preserves cell metabolic activity and membrane integrity.
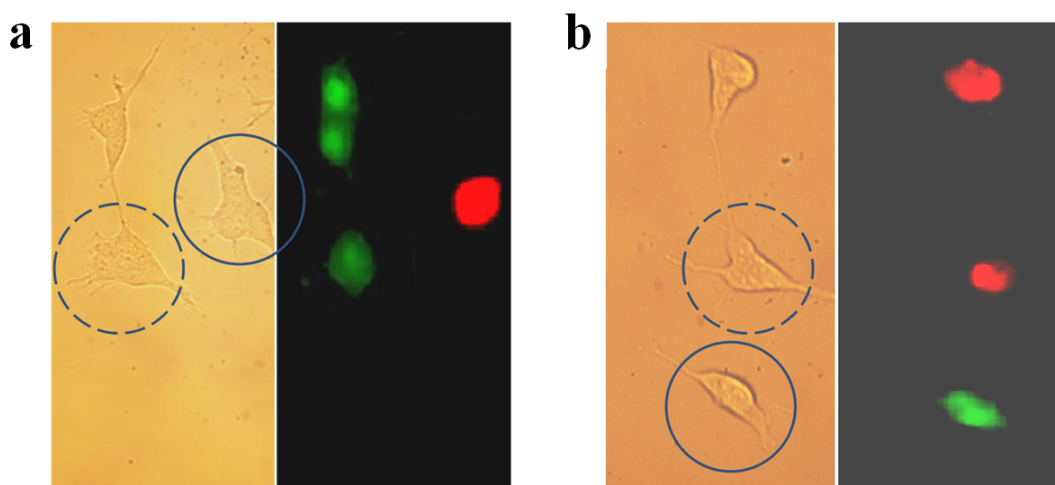
Figure 3.18: Cell viability and vitality assay on SH-SY5Y-Tau cells. The dash-circled cell is punctured by nFTP once every hour for 12 hours. The solid-circled cell is punctured by a microscale fiber. (a) Cell viability/cytotoxicity (L3224, Invitrogen) assay. Green-fluorescence indicated active esterase condition. Red-fluorescence indicated loss of cell membrane integrity. (b) Cell vitality (L34951, Invitrogen) assay. Green-fluorescence indicated loss of cell membrane integrity. Red-fluorescence indicated active metabolic condition.

4

Potential Applications of FTP

4.1   Membrane Potential Sensing with Nanodiamond

The ability to make electrical measurements inside cells is central to understanding the fundamental behavior of cells and cell networks of neural and cardiac systems. The patch clamp technique, in which a glass micropipette filled with electrolyte

is inserted into a cell, offers both high temporal resolution and signal-to-noise ratio[44]. However, the micropipette cannot be very small due to the increase of the impedance at the interface between the micropipette and the cell interior. Other electronic methods that uses nanosize transistor have been proposed[124], but they have low yield on devices functioning successfully and require laborious fabrication steps. I propose using a single nanodiamond with nitrogen-vacancy (NV) centers attached to an FTP tip to optically measure magnetic field or electric field created when neurons or cardiomyocyte cells fire action potential.

The negatively-charged NV center is a lattice defect in diamond, which consists of a substitutional nitrogen atom and an adjacent vacancy. The spin states of NV centers can be optically addressed and are sensitive to a number of physical quantities, such as magnetic[119,83,40] and electric fields[33], temperature[70,1,27,92], orientation[32], and pressure[31]. NV centers in diamonds have emerged as a promising sensor due to its atomic size, stability, and unprecedented sensitivity. Nanodiamond with these defects can be used to locally detect and measure physical quantities of the target. In addition, the photostability and biocompatibility of fluorescent NV centers within nanodiamonds have also permitted quantum control of NV centers within living cells[144]. *In-situ*, real-time measurement of membrane potentials based on electric field detection would be possible, when a single nanodiamond immobilized at an FTP is delivered near to a cell membrane in which they experience a strong potential drop between the intra- and extra-cellular space (Figure 4.1a).
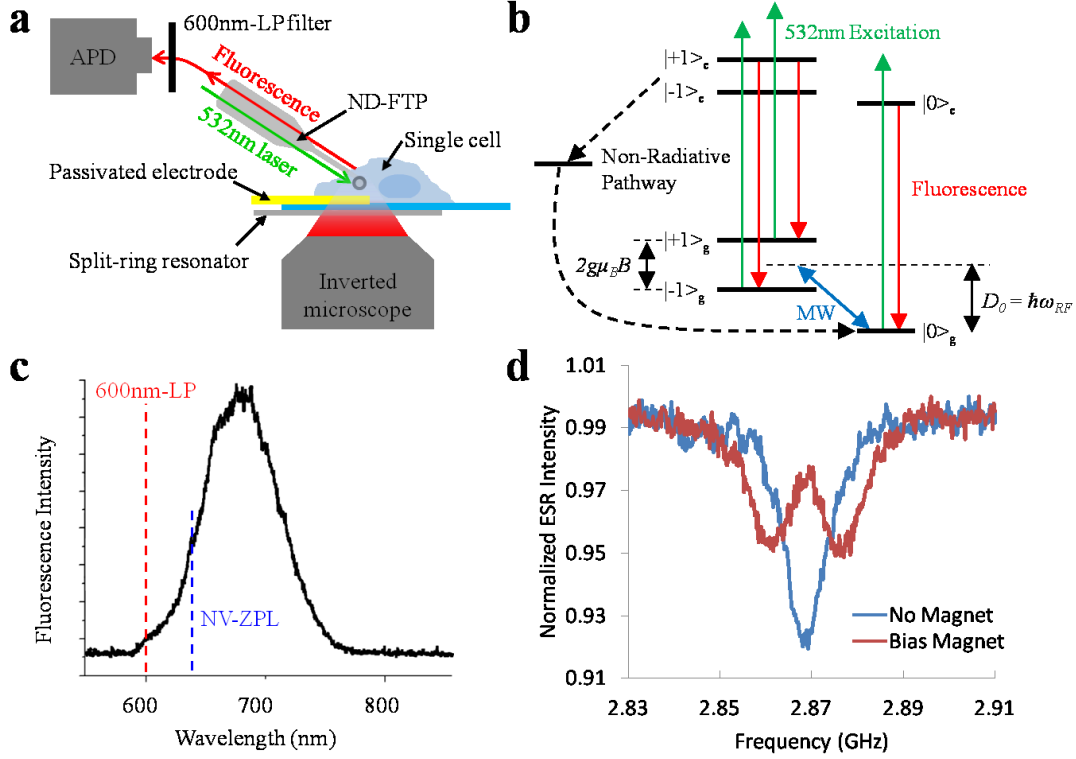
Figure 4.1: Characteristics of the nitrogen-vacancy (NV) center. (a) Schematic setup for using nanodiamond-FTP (ND-FTP) for measuring intracellular action potentials. (b) Energy-level diagram of NV−. |g> denotes the electronic ground state, |s> the electronic excited state. Green arrows indicate the radiative transition (excitation , and black dotted arrows indicate nonradiative decay via the singlet state. D is the zero-field splitting and $2\gamma B$ is the Zeeman splitting. (c) Photoluminescence spectrum of NV centers in a nanodiamond attached to an FTP. 532 nm laser was used for excitation and 600nm-LP filter was used for measuring photoluminescence. We could observe NV− zero phonon line (638 nm) and NV− vibrational side bands (630–800 nm). (d) Electron spin resonance (ESR) spectrum of ND-FTP recorded using the optically detected magnetic resonance (ODMR) technique. A drop in fluorescence at 2.87 GHz was observed at zero magnetic field, and Zeeman splitting of the peak was observed the magnetic field is applied. $2\gamma B$ was 190 MHz and deduced magnetic field applied parallel to the NV axis was 3.3 mT.

The principle of microwave detection is to transduce the amplitude of microwave field into the population of spin states of NV centers. Split-ring resonator was used for microwave delivery. As illustrated in Figure 4.1b, when the microwave frequency ω_{RF} coincides with the resonant frequency ω_0 between the NV's $|0>_g$ ground spin state and the $|-1>_g$ or $|+1>_g$ spin state, the NV is driven from the $|0>_g$ to the $|-1>_g$ or $|+1>_g$ state. The $|+1>_g$ and $|0>_g$ spin population can be optically readout through the fluorescent intensity difference, because the $|+1>_e$ spin states have non-radiative decay paths whereas the $|0>_e$ spin states do not. In other words, as an auxiliary microwave field is swiped over the ESR resonance, excitation from $|0>_g$ to $|+1>_g$ occurs when the microwave frequency is resonant with the ESR transition, resulting in a reduction of fluorescence intensity. This optically detected magnetic resonance (ODMR) effect is characteristic of NV centers. The energy difference between spin sublevels (zero-field splitting or resonant frequency, $D_0 = \hbar\omega$) is D = 2.87 GHz for the ground state.

The main $|g> \leftrightarrow |e>$ transition has a resonant wavelength at 638 nm (zero phonon line), and most luminescence appears in vibrational side bands between 630 and 800 nm (Figure 4.1c). We carried out ODMR experiment by continuous illuminating 532nm excitation laser while step-sweeping microwave frequency. For a nanodiamond sample, we could measure ESR spectrum at zero and nonzero magnetic field (Figure 4.1d). When a magnetic field was applied, two resonance peaks separated by 190 MHz appeared in the ODMR spectrum, because the degeneracy between the

$|\pm1>_g$ levels was lifted (Zeeman splitting). The frequency separation between the two resonances is given by $2\gamma B_z$, where γ (= 28 GHz/T) is the gyromagnetic ratio and B_z is the magnetic field parallel to the NV axis. B_z was applied by the neodymium magnet and was calculated to be 3.3 mT.

To test if ND-FTP has enough temporal resolution and signal-to-noise ratio to detect action potentials, we first simulated a non-invasive magnetic field detection scheme[43]. ND-FTP was placed on top of a micro-ring resonator that applies a uniform microwave in z-axis[16] and was brought near (<5 μm) to an micro-wire which functions as an artificial axon (Figure 4.2a). External magnetic field was created by the artificial axial current and induced Zeeman splitting to the ND-FTP. We fixed the microwave frequency at 2.87 GHz, corresponding to zero-field splitting, and measured the intensity change induced by the Zeeman splitting (Figure 4.2b). We fixed the distance between ND-FTP and the artificial axon and the microwave frequency/intensity, and varied the artificial Axial current intensity and frequency. Figure 4.2c and 4.2d shows that fluorescence contrast of NV centers in response to current frequency modulated by an 20Hz square wave can be stably detected. The current flowed through the artificial axon was 10 mA, and the ESR shows roughly 5 MHz peak splitting. This corresponds to 178 μT magnetic field applied parallel to NV-center axis. To simulate neurons, magnetic field applied to the ND-FTP should be in order of a few nT and induces only a few hundreds of Hz splitting in ESR[43].

For now, we did not meet the required sensitivity for measuring neural action

potentials, but optimizing the setup is ongoing. First, in order to decrease the background noise, we can isolate our system from background electromagnetic fields or microwave sources as well as from vibration or light source. Second, we can adapt other NV signal detection protocols such as Hahn echo pulse scheme (field-induced phase accumulation) or Ramsey-type schemes (free induction decay) instead of current scheme using continuous illumination of excitation laser and microwave (ODMR)[119,33]. Although these measurement schemes require brighter fluorescence from NV centers and more complicated measuring schemes, they have significant advantage in sensitivity. Thirdly, we can goal to measure electric field across the cell membrane. The ODMR spectrum is also sensitive to the electric interaction, caused indirectly by the Stark effect and spin-orbit coupling, and can be used to measure electric fields. Given typical membrane potentials of 40–80 mV and a membrane thickness of 5–10 nm, the expected electric field is of order 10^7 V/m, and the corresponding ODMR frequency shifts a few megahertz. An A.C. electric-field sensitivity reaching rouhgly $2 \cdot 10^5$ $Vm^{-1}Hz^{-1/2}$ has been achieved[33], and this strong response should allow monitoring of the hundreds of milisecond excitation of cardiac cells or the millisecond excitation of neurons in real time.
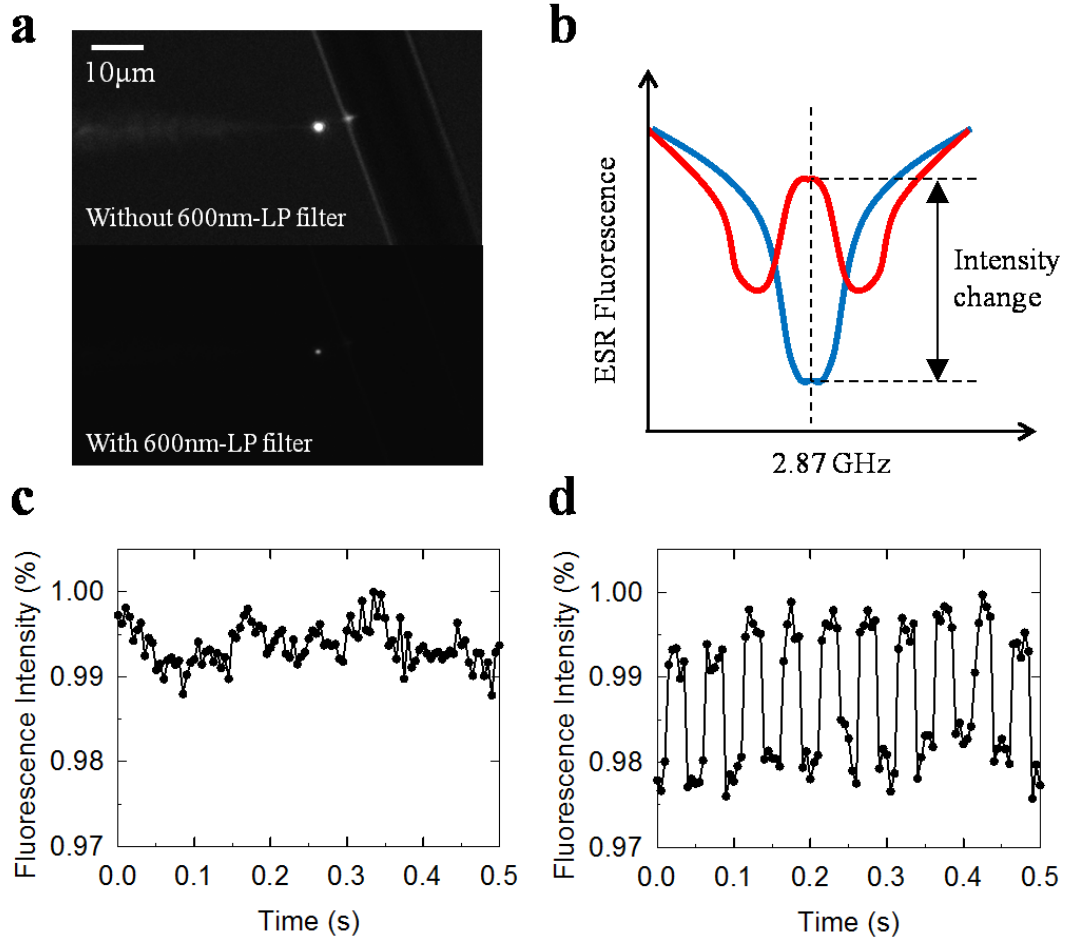
Figure 4.2: Response of ND-FTP to simulated action potential. (a) Optical image of ND-FTP brought close to a 20μm-thick electrode. The electrode served as an artificial neuron where the current was flowed to apply magnetic field on the ND-FTP. (b) Schematic ESR spectrum with (red) and without (blue) the external magnetic field. The magnetic field from the artificial neuron influences the energy level of NV centers and induces the change in ESR spectrum. At fixed microwave frequency of 2.87 GHz, we can detect the fluorescence contrast. (c) Real-time fluorescence intensity of NV centers in a nanodiamond at an FTP tip without the magnetic field (control condition). (d) Fluorescence contrast of NV centers when 10 mA is flowed through the artificial neuron. The fluorescence contrast at 20 Hz modulation could be stably measured.

4.2 Temperature and Pressure Sensing

The zero-field splitting is dependent on the temperature, local strain, and pressure allowing NV centers be used as a nanoscale termal, local strain, and pressure sensor[56]. The hydrostatic pressure shifts the optical ZPL and the ground state ODMR of NV− centers by $\partial D/\partial P=$ 1.5 kHz/bar at room temperature[31], and the temperature shifts by $\partial D/\partial T=$ 74.2 kHz/K under ambient conditions[1].

Precise local thermometry has a wide range of applications in the semiconductor industry and in living systems[70,92]. The lowest sensitivity of a nanodiamond sensor as a thermometer so far is 130 mK/Hz$^{1/2}$[92]. Nanodiamond-FTP device allows measuring local temperature in three-dimensional space with spatial resolution on the order of a few nanometers. For example, a nanodiamond at an FTP tip can be delivered and immobilized within the cells to measure local temperature changes induced by chemical reactions or biochemical processes.

Small changes in volume and pressure of eukaryotic cells offers an important signal for cell proliferation, death, and migration[114], but the nanodiamond-FTP is not suitable as a biosensor for measuring the intracellular pressure changes in different components of a living cell. Silicon chips-based pressure biosensor demonstrated that osmotic shock (1/10 water dilution of the standard cell medium) to HeLa cells induced a hydrostatic pressure of roughly 7 bar inside the cell[38]. The ZPL of NV-

centers is expected to shift only 11 kHz due to the osmotic shock. Instead, the diamond pressure sensor is suitable for applications in extreme environments such as in diamond anvil cells (DAC) that achieves pressure up to millions of bars[31].

4.3   Surface-Enhanced Raman Spectroscopy

Surface-enhanced Raman scattering (SERS) has demonstrated single-molecule sensitivity and is becoming intensively investigated due to its significant potential in chemical and biomedical applications[67,93,100]. When a gold nanorod is excited with an external laser and carries the localized surface plasmons (LSPs), it serves as a hot spot where the local optical field is enhanced tremendously when compared to its surrounding. Single molecule enhancement factor (SMEF), which quantifies the increase in signal intensity (counts $\cdot$ s^{-1}mW^1) per molecule, can be expressed by E^4 approximation, the fourth power of the ratio of the total electric field $E(r_m, f)$ at the molecule location r_m to the incident excitation field $E_{inc}(f)$ where f is the laser frequency[36].

$$SMEF(r_m, f) = \left| \frac{E(r_m, f)}{E_{inc}(f)} \right|^4 \tag{4.1}$$

Typical single molecule enhancement factor (SMEF) of plasmonic materials ranges from 10^4 to 10^7, which is sufficient for single molecule detection[66]. The gold nanorod attached to an FTP tip can be excited via external laser, and its enhanced Ra-

man scattering signal can be collected either through the FTP or through an objective. The gold surface can be functionalized to be sensitive to specific proximate analyte molecules. For example, gold nanorods immobilized with Thymine (T)-rich single-stranded DNA (ssDNA) can be used for Hg^{2+} ion detection[45], or gold nanoparticles labeled with oligonucleotides and Raman-active dyes can be used to uniquely indentify gene sequences for HIV, Ebola, and Hepatitis[25]. Theoretical analysis through time-dependent density functional theory (TDDFT) calculations is also possible for comparison with experimental SERS data[4].

4.4 FTP with Metasurface for Optical Trapping

In order to further reduce invasiveness of the FTP device, I propose a non-invasive method to deliver, immobilize, or manipulate optically-trapped nanosensors inside a single live cell and detect intracellular physical, chemical, and biological properties (Figure 4.3a).

A gradient force of a single tightly focused laser beam allows to trap individual nano- and micro-sized particles in three dimensions. This technique known as optical tweezers has found wide-spread applications in biology, physics, chemistry and materials science[88], because it allows applying well-defined forces and manipulating nano- and microscale particles non-invasively. Structures can be fabricated on a fiber tip to manipulate phase of laser and focus it to create an optical trap in which particles

would be immobilized. The levitated particles or nanosensors will eliminate the need for mechanically puncturing into the cells, thus increasing specificity and remove cell invasiveness. This nanosensor can range from protein-functionalized gold nanoparticle, nanodiamonds, quantum dots, nanocavities, and etc, and be used to quantify real-time, intracellular dynamics. This may provide a new all-optical methodology for internalizing nanosensors within specific intracellular regions.

3D structure functioning to create a tight focus can be a convex optical lens at the fiber tip[10], chemically-etched graded-index fiber[39], or fresnel lens structure at the fiber tip[24]. However, these 3D optical materials are complex to fabricate at accuracy of optical wavelength. Instead, by depositing metal structures on the flat fiber tip that functions as a metastructure[3,80] (Figure 4.3a), optically thin engineered metasurfaces can be used to engineer wave fronts by locally controlling phase and amplitude of light along the surface. These metasurface can be an array of metallic nantennas[3], dielectric a-Si pillars[11], plasmonic micro-ring arrays[80], and plasmonic micro-hole[103].

Unlike optical components that conventionally rely on propagation effect, abrupt phase shift can be introduced to make any desired wave front. V-shaped nanoantennas, whose double resonance effect, make them possible to obtain great phase changes and maintain large amplitude within an ultra-thin area[141]. By circularly arranging these antennas on a flat surface, linearly polarized light can be focused at a certain focal f by compensating the interface for the distance of every point from a spherical surface centered at the focus and with radius f[3]. Since phase can be con-

trolled locally at accuracy of nantenna spacings, this structure allows spherical-abberation-free, diffraction-limited focusing. However, this structure suffers from limited transmission efficiency (1-10%) due to the metal absorption and reflection loss, and is too large to fabricate on a fiber tip (lens size: roughly 1mm in diameter[3]). Similarly, array of dielectric a-Si pillars can be used for local control of light phase and has higher transmission efficiency (roughly 85%), but this structure also suffers from its large lens size[11].

A simple design of metasurface can be created by fabricationg a micro-ring arrays at the flat fiber tip (Figure 4.3b)[80]. When a TM polarized monochromatic plane wave impinges on the micro-ring slit, it excites surface plasmons, the collective oscillations of the electrons at the surface. The surface plasmons propagate along the surface of the metal film and are diffracted to the far-field by the periodic grooves, which are designed with a width smaller than half of the incident wavelength to allow a high diffraction efficiency. Constructing interference of such diffracted beams leads to the focusing effect at a certain point on the beam axis (< 3 μm away from the surface). Since the diffracted beams are modulated by the nanometric grooves, through adjusting the parameters of the grooves such as width, depth, period and number of grooves, the diffracted beams can be fully manipulated resulting in a tailored ultra-compact lens with subwavelength resolution and nanometer accuracy. However, this structure may suffer from low transmission efficiency (5-15%).

Another simple and microsize design of metasurface would be a planar metallic

transmissive micro-aperture ($< 3 \mu$m) capable of focusing visible light at the flat fiber tip (Figure 4.3c)[103]. Four 500nm-thick concentric metal rings spaced 500 nm apart comprises the metasurface. The focal spot size was simulated to be dependent on the incident light wavelength and be diffraction-limited. The interactions of the electromagnetic radiation at the metal–dielectric interface excite surface plasmons at both, the gold–fiber interface as well as the gold–air interfaces and get coupled through the hole. These surface plasmons then reradiate and diffract into photons, superpose with the incident planar wavefronts, and generate high energy concentration at the focal spot. The micro-aperature structure provides tight focal spot and high transmission efficiency (40-60%), and is easier to fabricate than the metal nantenna or micro-ring arrays. The flat fiber facet can be realized with platinum (Pt) using focused ion beam deposition, leaving an circular aperture within 2 μm in diameter.

In order to have a stable trapping where the gradient trapping force is larger than the scattering force, a 1064 nm laser should be used for illumination (Section A.4). Typically, 100mW is enough to trap a gold nanorod[46]. Depending on its aspect ratio and size, the trapped gold nanorods align along or orthogonal to the direction of the propagating laser light[108]. The Brownian motion may introduce extra torque and causes shift and tilt from its equilibrium position[14]. Heating of an optically-trapped nanoparticle can be an issue to use this tool for intracellular detection. Plasmonic heating from non-radiative decay channels due to electron-electron and electron-phonon interactions increase as the absorption cross section increases. For small par-

ticles, the analytical solution of heat change is $\Delta T(r) = \sigma_{abs}I/4\pi\kappa r$[57]. Assuming we know the absorption cross sections and the thermal conductivity of the media, I calculated the heating of airborne gold nanoparticles with diameters of 80, 150, and 200 nm to be 1.8, 9.6, and 21 K/mW with 1064 nm incident laser, respectively. The corresponding values in water are 0.15, 0.88, and 2.0 K/mW, respectively. Assuming 100 mW laser is delivered to a 100nm gold nanoparticle in water, 15K temperature change is expected.

Another potential issue may come from the particle not being able to penetrate through the cell membrane. Median forces required to penetrate cellular or synthetic bilayers with 200nm-thick nanoprobes was roughly 10 nN[8]. Since the particle is much smaller than a nanoprobe, much less power may be required for penetration. For intracellular injection of particles, femto-second laser pulse may be used for precise ablation and penetration of membrane[120], or the particle can be injected into cells through a combination of plasmonic heating and optical force[76].

A metasurface on a flat optical fiber tip can function as an optical tweezer to trap in near-field within 3 μm apart from the flat fiber tip and freely manipulate single plasmonic particles in three dimensions (3D). I propose a realistic way to fabricate flat optical fiber tip and plasmonic nanostructures, which would provide higher field enhancements. Intracellular surface-enhanced Raman spectroscopy would be also available on the trapped nanoparticle[86]. This tool can be used for non-invasive method for drug delivery, cellular manipulation, and intracellular measurements.
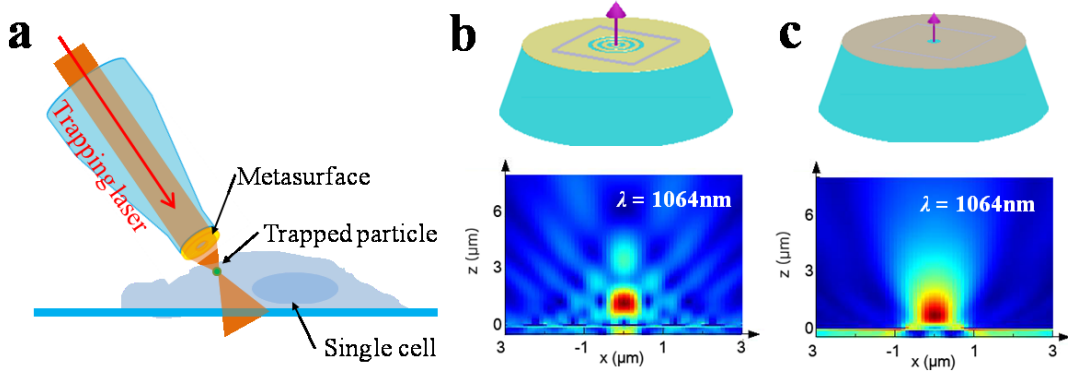
Figure 4.3: Schematics and simulation results of metasurface on an FTP. (a) Schematic setup for trapping a plasmonic particle and interrogating a live single cell. An optical fiber is gradually tapered from 125 µm to roughly 10 µm, and metasurface (metal micro-hole in the figure) is fabricated on a flat fiber surface to focus light in near field (2 µm). A particle can be optically trapped at the focus. (b) Plasmonic micro-ring metasurface. Four 500nm-thick concentric Pt rings (yellow) were fabricated on the fiber surface (blue). Finite-difference-time-domain (FDTD) simulation was used to calculate the near-field optical mode. When incident with Gaussian 1064nm laser (purple arrow), light was focused in an approximate spot of $1\mu m^3$. (c) Plasmonic micro-hole metasurface. Pt aperture with 0.75 µm in diameter was fabricated on the fiber face. FDTD simulation on Pt microring structures showed that the trapping mode of $<1\ \mu m^3$ could be formed at near-field to the FTP.

4.5 Mechanical Sensing with FTP

Microcantilevers are micromechanical beams that are anchored at one end, such as diving spring boards. Micromechanical cantilever-based biosensors can serve as a highly sensitive sensor platform by measuring stresses and mass changes with ex-

tremely high sensitivity[54,12]. Cantilever-based sensors have been used to measure biological dynamics such as antibody/antigen interactions[134], single virus mass detection[41], and detection of biomarker transcripts in human RNA[143]. As demonstrated in Section 2.2, we can fabricate a mechanical FTP with an end-portion nanowire and use it as a cylindrical micromechanical sensor. This sensor allows a lab-on-a-fiber platform for label-free, multiplexed detection of molecules at low cost.

Stress and bending can be measured when molecules are adsorbed on one side of the cantilever, or their change in mechanical resonance frequencies can be measured when the effective mass of the microcantilevers changes due to chemical or biological adsorption. Their typical dimensions are approximately 100 μm long, 20 μm wide, and 1 μm thick. The end-portion nanowire of a mechanical FTP can be submicron thick and several hundreds of microns long and be fabricated at the dimension of well-studied microcantilvevers (Figure 4.4a and 4.4b). By monitoring cantilever bending induced by analyte adsorption and resonance frequency change due to adsorption-induced mass loading, we can measure chemical or biological processes of proteins and nucleic acids or detect nanodusts and chemicals floating in air.

As shown in Figure 4.4c, a mechanical FTP is aligned parallel to a lens fiber that detects the intensity of a HeNe laser coupled to the mechanical FTP. The mechanical FTP is modulated at the driving frequency of electric field created at a gap between two micro-electrodes. At the resonance frequency of the FTP, the end-portion nanowire will modulate with large amplitude and the light intensity measured through

a lens fiber will vary as the fiber gets in and out of alignment with the mechanical FTP. As shown in Figure 4.5, Fast Fourier transform (FFT) of the light intensity graph over time shows one clear peak at the modulating frequency which is also equal to its resonance frequency. The frequency matches the theoretical first order resonance frequency of the end-portion nanowire which is normally at 10 to 100 kHz (Figure 4.6).

The resonance frequency f of a cantilever varies sensitively as a function of mass loading Δm and can be expressed as

$$f = \frac{1}{2\pi} \sqrt{\frac{k}{m^* + \alpha \Delta m}} \tag{4.2}$$

where k is the spring constant of the cantilever, m^* is the effective mass of the cantilever, and α is a numerical constant. We ran COMSOL simulation on a mechanical FTP with an end-portion nanowire. Its dimensions are 2 μm in starting diameter, 400 nm in ending diameter, and 400 μm in length. As the ending diameter and the length of the nanowire increases, the effective mass increases (Figure 4.6b and 4.6e). Its vibrational mode frequency decreases as its length increases (Figure 4.6c), but the frequency may increase as its diameter increases because the nanowire becomes stiffer and its spring constant increases (Figure 4.6f). For a 200μm-long nanowire, the mechanical frequency of the first mode (red line) and the effective mass are 650 kHz and 28 pg respectively, and the calculated spring constant from Equation 4.1 is 467

N/m. The mechanical shift of the first mode induced by the saturated protein adsorption (density $= 1 \cdot 10^{-5}$ kg/m^2) of the nanowire is roughly 85 kHz, and assuming that the spring constant is kept constant during adsorption[68] and $\alpha = 1$, the mass loading from the protein adsorption is calculated to be 9 pg (Equation 4.1). The actual mass of the saturated protein on the surface is 7.5 pg and is in same dimension to the mass loading.

A mechanical FTP has potential as a highly sensitive sensor platform for label-free detection of biological molecules and can be assembled for multiplexed detection at low cost and at shorter turnaround time. For proof-of-concept demonstration, a mechanical FTP can be coated with roughly 50 nm of aluminum oxide (Al$_2$O$_3$) via e-beam evaporation or ALD and be used to detect dew point, ppm, or relative humidity in air or in industrial gases[122,81]. Al$_2$O$_3$ has been demonstrated highly selective for moisture measurement[102]. A quartz-crystal microbalance (QCM) sensor coated with Al$_2$O$_3$ is commercialized for mositure mass spectrometry from AMETEK (Model 3050-OLV) but is bulky and expensive. In comparison, the mechanical FTP allows reliable, portable sensing at low cost. In addition, the mechanical FTP can be used for various applications by coating with materials that adsorb analytes for chemical or particulate pollution detection in air[19,20,105].
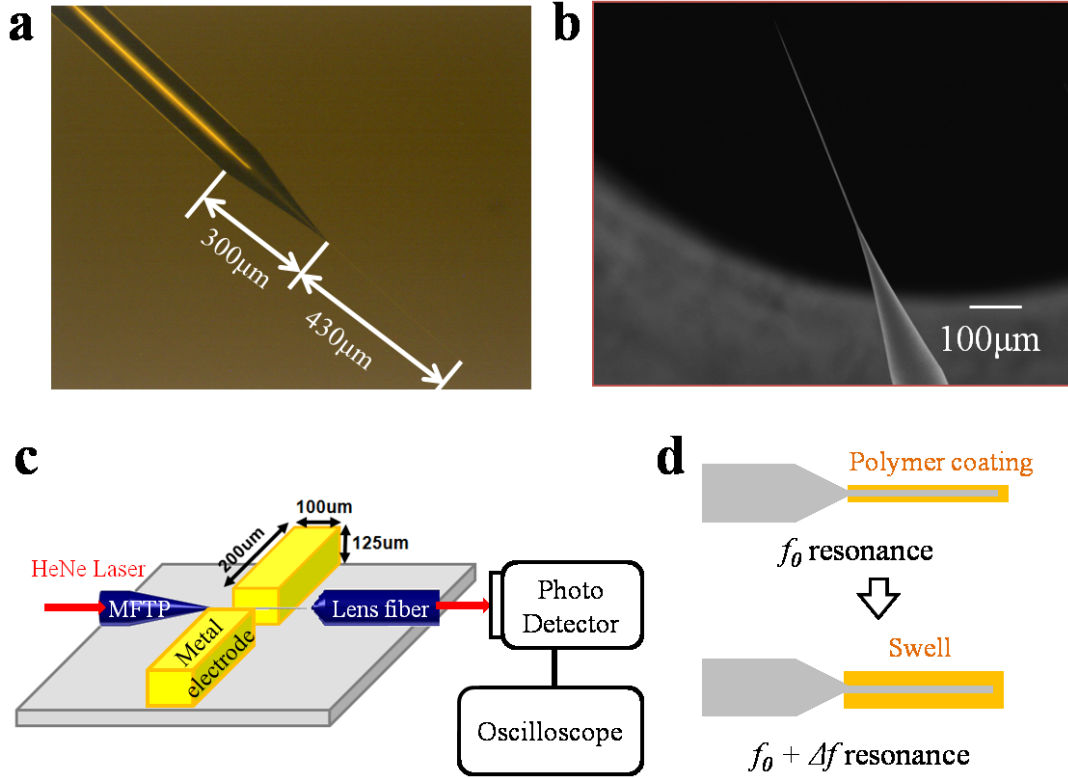
Figure 4.4: (a,b) Optical and SEM image of a mechanical FTP. The taper portion of the FTP was 300 μm long, and the end-portion nanowire was 430 μm long and 700 nm in diameter. (c) Schematic for mechanical FTP sensing. mechanical FTP and a lens fiber is aligned parallel so that the HeNe laser transmitted through the FTP can couple into the lens fiber when in phase. By modulating the frequency of electric field between two micro-electrodes (gold), the transmission through the lens fiber will vary as the mechanical FTP accordingly vibrates. (d) Schematic for humidity detection in air. A mechanical FTP can be coated with polymer (e.g. Polyvinylpyrrolidone (PVP)[90]) which absorbs moisture and swells.

Signal from Oscilloscope   FFT of oscilloscope signal
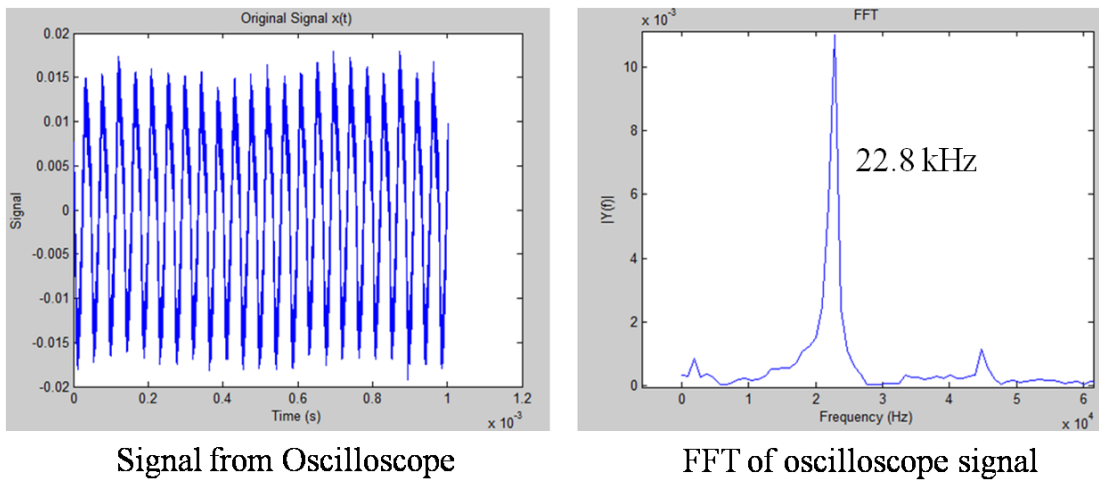
Figure 4.5: Readout from a photodiode coupled with a lens fiber. At resonance frequency, the transmission intensity showed a sign wave with the biggest amplitude (left). Its FFT showed a resonance frequency that matched with the modulation frequency (right)
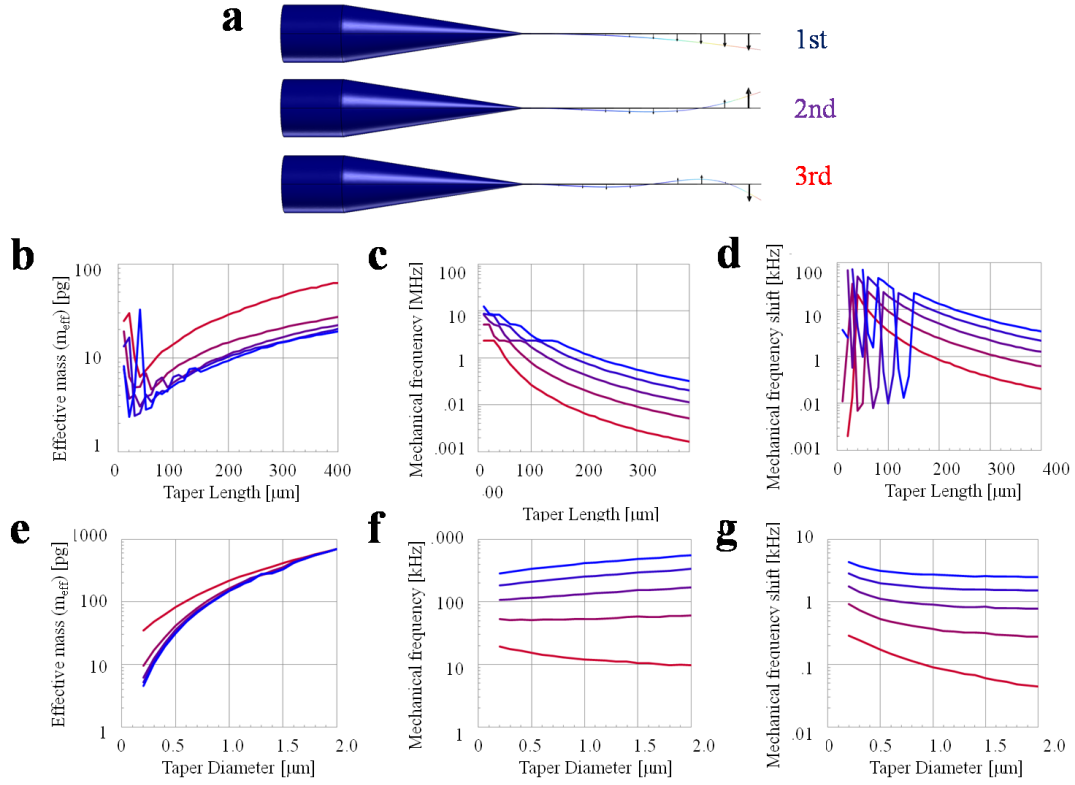
Figure 4.6: COMSOL Simulation of a mechanical FTP. (a) 1st, 2nd, and 3rd order mechanical modes of a mechanical FTP. (b) Effective mass vs. end-portion nanowire length plot. Different color curves mean different vibration modes (red; lower, blue; higher order mode). (c) Mechanical resonance frequency vs. end-portion nanowire length plot. (d) Mechanical shift induced by protein adsorption vs. end-portion nanowire length plot. Mechanical shift is resonance frequency difference between w/ and w/o protein adsorption. We assume standard saturation of the adsorbate as the protein which has 3 x 3 nm size and 60 kDa of the molecular weight ($1 \cdot 10^{-5} \mathrm{kg/cm^2} x$'). (e) Effective mass vs. end-portion nanowire diameter plot. (f) Mechanical resonance frequency vs. end-portion nanowire diameter plot. (g) Mechanical shift induced by protein adsorption vs. end-portion nanowire diameter plot.

5

Conclusion

This thesis mainly discusses wet-chemistry etching methods for nanoscale fiber-tip-probe (FTP) fabrication and its application for label-free, real-time intracellular biomarker detection in single live cell. The fabrication is scalable and mass-producible, and the bioprobe may be composed of a wide range of solid base materials. Other FTP applications such as measuring intracellular dynamics of electromagnetic fields,

temperature, or pressure in neurons or cardiac cells (Section 4.1 and 4.2), detecting humidity or pollutant levels in air (Section 4.3), and coupling light efficiently to optical devices in three-dimensions (Section 2.2) are also discussed.

Chapter 2 discusses the versatile fabrication method of FTPs. FTP is a fiber wet-etched at nanoscale dimensions. One main form of FTPs mostly discussed in this thesis is a single-ended tapered optical fiber that has a sub-100nm tip in diameter and has extreme smooth surface. Nanoscale optical sensors such as functionalized gold nanorod, nanodiamonds, or quantum dots can be immobilized at the FTP tip for efficient light coupling and localized approach of the sensors to measure physical properties of the environment. Another form of FTPs has an end-portion nanowire with various aspect ratios. They can be several hundreds of micrometers long as well as sub-micron in diameter, and function as a microcantilever sensor. FTP with a shorter nanowire can be used for efficient light coupling to characterize optical devices or properties of materials. Double-ended FTP with unetched optical fibers at both ends and a mid portion nanowire can be used as well for device characterization. Multiple FTPs in a uniform configuration can be mass-fabricated at the same fabrication round and at low cost. The base material of the FTP can be any as long as it has a matching etchant.

Chapter 3 discusses the achievement of using FTP for measuring intracellular biomarker dynamics in intact live cells. Combining the advantages of high selectivity from antibody-antigen recognition and high sensitivity of localized surface plasmon

resonance (LSPR) of a gold nanorod immobilized at the FTP tip, we could quantify intracellular biomarker concentration dynamics in a label-free, real-time manner. Our method is an alternative approach to fluorescent labeling approach, and will be especially useful for cells and systems that are hard to label, for example, immune cells, neurons, and precious patients' cells and circumstances that require *in-vivo* and *in-situ* detection. The capacity of LSP-FTP to three-dimensionally manipulate ensures the minimal and local invasion of the probe into the cell and high reproducibility of the results. Current demonstration regards bioprobes detecting a few specific biomarkers such as p53 (tumor surpressor biomarker) in Hela cells and β-Amyloid and Tau protein in neurons. Its high sensitivity and single cell measurement capability make it a unique tool to diagnose biomarkers in clinically obtained, limited, primary cells, as well as to determine the outcomes of interventions of neurodegenerative diseases.

Chapter 4 discusses the applications of FTPs. A plasmonic FTP can be used for surface-enhanced Raman spectroscopy (SERS) for high-sensitive chemical, molecular detection. A nanodiamond, instead of gold nanorod, can be immobilized at the FTP tip for intracellular electromagnetic fields, pressure, or temperature at single cell level. Instead of using a nanoscale tip, a metasurface can be fabricated at a flat fiber end in a few micrometers in diameter and be used for superfocusing and optical trapping of a nanodevice for minimal invasiveness. A mechanical FTP with an end-portion nanowire of large-aspect-ratio functions as a portable, low-cost microcantilver sensor and be used for humidity or pollutant sensing in air.

For future direction for improvement, firstly better measurement scheme can be realized. For example, a laser with single wavelength may be transmitted through an FTP for excitation of LSPR of a gold nanorod, and the emitted light signal may be detected through the FTP. The collected light may be filtered out of the excitation laser wavelength and only feature excitation from the gold nanorod. Secondly, short peptides as biorecognition elements may be used instead of larger antibodies for higher sensitive detection[117]. The immobilized peptide recognition elements can significantly increase sensitivity and lower detection limit by bringing targeted analytes much closer to the surface. If proper functional peptides can be tested and proven functional, it may enable detection of smaller proteins such as DNA or RNA strands.

In summary, the advantage of this FTP technology is (1) scalability, (2) fast and low-cost fabrication in mass-production, (3) nanoscale locality and maneuverability in three dimensions, and (4) high sensitivity and specificity. FTP allows quantitative, label-free, real-time measurement of intracellular biomarker dynamics in intact live cells, or in clinically obtained, limited, primary cells. Furthermore, our method can extend to a high-throughput multiplexed system, using FTP arrays for 3D mapping of the environments.

A

Theoretical Background

A.1 Surface Plasmon Resonance (SPR)

When the frequency of incident photons matches the natural frequency of oscillating surface electrons at the interface between a negative and positive permitivity material, surface plasmons (SPs) can be excited and confined at the interface. Surface

plasmon can be defined as a density fluctuation of nearly-free electron gas propagating in a direction parallel to the interface. Analytical solution of surface plasmon can be derived for infinite flat surfaces and for nanparticles. In this section, we will discuss bulk plasmons (the electron density oscillations of electron gas), surface plasmons (the electron density oscillations bound at the metal/dielectric interface) and localized surface plasmons in nanostructures.

A.1.1 Drude−Sommerfeld Electron-Gas Model

Drude−Sommerfeld model simplifies the electron dynamics in a noble metal into an equation of motion of a damped oscillator where the electrons are moving between heavier, relatively immobile background ions. These electrons move freely in between independent collisions, which occur with an average rate of $\gamma = 1/\tau$, where τ is the electron relaxation time. Drude−Sommerfeld model of a free electron gas (no spring constant) is

$$m_e \frac{\partial^2 \vec{r}}{\partial t^2} + \frac{m_e}{\tau} \frac{\partial \vec{r}}{\partial t} = e\vec{E}_0 e^{-i\omega t} \tag{A.1}$$

where m_e describes the effective free electron mass, e is the free electron charge, τ is the relaxation time, and ω and E_0 are the frequency and amplitude of the applied electric field, respectively. By substituting the velocity ($\vec{v}$) with the conduction current density equation ($\vec{J} = -Ne\vec{v}$) and assuming that the current density oscillates at the

same rate to the applied electric field, Equation A.1 can be expanded to the conductivity equation.

$$\sigma(\omega) = \frac{ne^2/m}{1/\tau - i\omega} = \frac{\sigma_0}{1/\tau - i\omega} \tag{A.2}$$

Both bound and conduction electrons contribute to permittivity of metal, and by substituting the current density equation, the conductivity equation (Equation A.2) into the Amphere law of Maxwell equation ($\vec{\nabla} \times \vec{H} = \frac{\partial \varepsilon_0 \varepsilon_B \vec{E}(t)}{\partial t} + \vec{J} = \varepsilon_0 \varepsilon_{eff} \vec{E}(t)$), the effective permittivity equation of Drude−Sommerfeld model ($\varepsilon_{eff}(\omega)$) can be derived.

$$\varepsilon_{eff}(\omega) = \varepsilon_B - \frac{\omega_p^2 \tau^2}{1 + \omega^2 \tau^2} + i \frac{\omega_p^2 \tau^2}{\omega \tau + \omega^3 \tau^3} \tag{A.3}$$

When $\omega_{vis}\tau \gg 1$,

$$\varepsilon_{eff}(\omega) = \varepsilon_B - \frac{\omega_p^2}{\omega^2} + i \frac{\omega_p^2}{\omega^3 \tau} \tag{A.4}$$

where n and m^* are the density and effective mass of the conduction electrons respectively, ε_B is the permittivity from bound electrons, and the plasma frequency is $\omega_p = \sqrt{ne^2/\varepsilon_0 m^*}$. As shown in Table A.1, the electron relaxation time (τ)and the plasma frequency (ω_p) can be calculated from the empirical DC conductivity (σ) by calculating $\tau = \sigma m^*/ne^2$.

Bulk plasmon polariton (Equation A.5) can be derived from the wave equation in

93

	Ag	**Au**	**Cu**
m^*/m_e [58]	0.96	0.99	1.49
n m^{-3} [95]	$5.86 \cdot 10^{28}$	$5.90 \cdot 10^{28}$	$8.47 \cdot 10^{28}$
σ $(\Omega m)^{-1}$ [65]	$6.21 \cdot 10^7$	$4.55 \cdot 10^7$	$5.88 \cdot 10^7$
τ fs	36.1	27.1	36.1
$\hbar\omega_p$ eV	9.17	9.06	8.85

Table A.1: Drude parameters for the noble metals Ag, Au and Cu.

Helmholtz form ($\frac{\varepsilon_r}{c^2}\frac{\partial^2 \vec{E}(\mathbf{r,t})}{\partial t^2} = \nabla^2 \vec{E}(\vec{r},t)$) by substituting the electric field equation and the real part of the dispersion equation from Equation A.4, and this equation is plotted in Figure A.2a. This applies to situations when the characteristic dimensions of the considered metal structures are larger than the electron mean-free path.

$$\omega = \sqrt{\omega_p^2 + c^2 k^2} \tag{A.5}$$

The bulk values for noble metals can be determined experimentally by reflection and transmission measurements on clean surfaces under ultrahigh vacuum conditions[58]. As shown in Figure A.1, although the Drude−Sommerfeld model (Equation A.3) describes well at low energy values (infrared regime), additional contributions are present at higher energies (above visible regime). This is because higher energy photons can promote electrons from deeper bands into the conduction band. This transition is called the interband excitations. In noble metals, the electrons originate

from the completely filled d-bands, which are relatively close to the Fermi-energy.
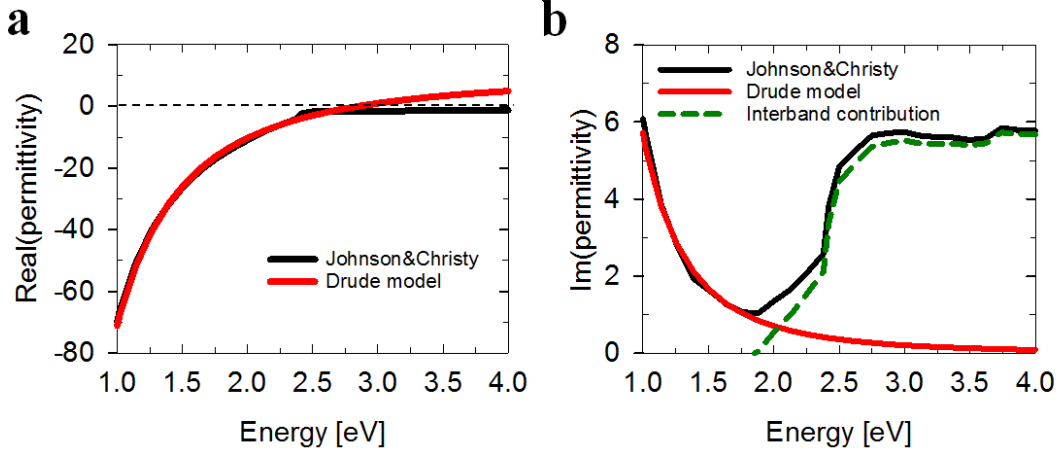
Figure A.1: Dielectric constant of gold. (a) Real part of the dielectric coefficient of gold. (b) Imaginary part of the dielectric coefficient of gold. Experimental data is compared to the analytical solution from the Drude-Sommerfeld model (Equation A.3). I set ω_p = 10 eV, $1/\tau$ = 0.07eV, and ε_∞ = 10. The interband contribution (green dotted line) is the difference between the experimental data and the Drude model. The empirical and calculated results behave similarly at lower photon energies but differently at higher photon energies due to the interband contribution.

A.1.2 SPR at Flat Surface

The electron density oscillations can be bound to the metal-dielectric interfaces, involving charges in the metal and electromagnetic fields in both media. This bound electromagnetic waves which travel along a metal/dielectric interface is called surface plasmon polaritons (SPPs). The field intensity in the metal and the dielectric

medium falls off exponentially in the direction normal to the surface (imaginary k vector). In the plane of the interface, the electromagnetic field intensity and charge distribution highly localized within the interface area propagates as a longitudinal wave along the surface (real k vector). Analytical solution of SPPs can be derived by solving Maxwell equations with the following boundary conditions of a TM wave.

$$z > 0 \begin{cases} H_d = (0, H_{yd}, 0)e^{(k_{xd}x + k_{zd}z - \omega t)} \\ E_d = (E_{xd}, 0, E_{zd})e^{(k_{xd}x + k_{zd}z - \omega t)} \end{cases} \tag{A.6}$$

$$z < 0 \begin{cases} H_m = (0, H_{ym}, 0)e^{(k_{xm}x + k_{zm}z - \omega t)} \\ E_m = (E_{xm}, 0, E_{zm})e^{(k_{xm}x + k_{zm}z - \omega t)} \end{cases} \tag{A.7}$$

The solution of the Maxwell equations satisfying the boundary conditions above is Equation A.8, and we can derive the dispersion relation of surface plasmons by solving the boundary solution.

$$\begin{cases} \frac{k_{zd}}{\varepsilon_d} + \frac{k_{zm}}{\varepsilon_m} = 0 \\ k_{xd} = k_{xm} = k_x \\ k^2 = \varepsilon_i \frac{\omega^2}{c} = k_x^2 + k_{zi}^2 \end{cases} \tag{A.8}$$

$$k_x = \frac{\omega}{c}\sqrt{\frac{\varepsilon_m \varepsilon_d}{\varepsilon_m + \varepsilon_d}}, \quad k_{zi} = \frac{\omega}{c}\sqrt{\frac{\varepsilon_i^2}{\varepsilon_m + \varepsilon_d}} \tag{A.9}$$

Equation A.9 shows that SPP can exists in a TM wave form at the interface. Real k_x is required for interface waves to propagate along the interface. According to Equation A.9, this can be fulfilled, if both the sum ($\varepsilon_m + \varepsilon_d$) and the product ($\varepsilon_m \cdot \varepsilon_d$)

of metal and dielectric permittivity are either both positive or both negative. In order for a bound solution, the normal components of the wave vector (k_{zi}) should be purely imaginary in both media and thus, exponentially decaying solutions. This can only be achieved if the sum of the permittivity is negative. From this, we conclude that both the product and the sum of the permittivity should be negative. Metals, especially noble metals such as gold and silver, have a large negative real part of the dielectric constant along with a small imaginary part. Therefore, at the interface between a noble metal and a dielectric, localized modes can exist.

Direct excitation of surface plasmons with an electromagnetic wave is not possible, because the dispersion curve of the surface plasmon does not cross the light cone at any point (Figure A.2a). For excitation of surface plasmons, a momentum kick should be provided i.e. by increasing the dielectric constant of the propagation medium ($n1>1$) to have higher momentum at the metal/medium interface. The light line in this case is tilted by a factor of n to $\omega = ck/n$. This situation is shown in Figure A.2a, which shows the surface plamon dispersion with the original free-space light line and the tilted light line in glass. As shown in Figure A.2b, Kretschmann configuration is often used to excite surface plasmon polariton. A thin metal film is deposited on top of a prism. To excite a surface plasmon at the metal/air interface, an evanescent created at the glass/metal interface has to penetrate through the metal layer. When an EM wave is propagating in a dielectric and is made incident on the metal film, some light is reflected back into the dielectric whereas the other propa-

gates in the metal parallel to the interface. This EM wave decays exponentially in the direction perpendicular to the interface and forms an evanescent wave. By tuning the angle of incidence of the totally reflected beam inside the prism, the resonance condition for excitation of surface plasmon resonance, the matching of the parallel wave vector component, can be fulfilled (yellow star point in Figure A.2a). Only the low energy branch of the surface plasmon polariton corresponds to a true interface wave, because the interband contribution and the imaginary part of dielectric function increases at high energy branch (Figure A.1).

The SPP excitation will show up as a minimum in the reflected light. The reflectivity is a function of the angle of incidence and the metal thickness (Figure A.2c)[69]. SPP will be strongly damped into the glass when metal is too thin, while SPP can no longer be efficiently excited due to metal film absorption when the metal film is too thick. The distinct resonance condition associated with the SPP excitation can be used for various sensor applications, because the resonance is sensitive to the refractive index of the medium on the opposite side of the film from the reflected light. For example, the position of the dip in the reflectivity curves can be used to measure adsorption or removal of target materials on the metal surface at submonolayer accuracy. As shown in Figure A.2d, COMSOL simultaion result demonstrated that a 3nm uniform coating of water leads to a measurable change in the surface plasmon resonance peak. This technique is commercialized[51] and commonly used to detect chemical binding/unbinding kinetics[61].
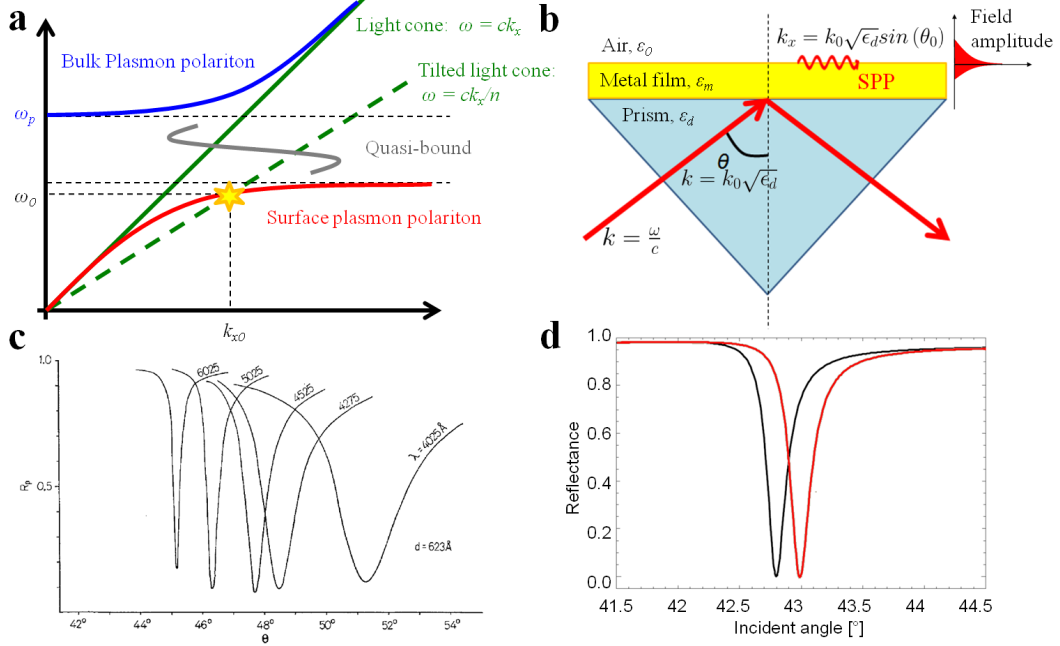
Figure A.2: Excitation of surface plasmons in the Kretschmann configuration. (a) Plasmon dispersion relation for a metal/air interface. Since the dispersion line of plasmons (red line without damping, blue line for free electrons) does not cross the light cone (green line) at any point, it is not possible to excite a surface plasmon at a metal/air interface with a light wave. Yet the light cone can be tilted (dotted green line) if we change from free space to a dielectric medium. At yellow star point, the evanescent wave from the prism will efficiently couple to the surface plasmon mode bound at the top of the gold surface. (b) Kretschmann configuration for excitation of SPP at the top of the gold surface. (c) The reflectivity of the exciting beam vs. the incident angle and for silver film thickness. The wavelength is fixed to 546.1 nm. The optimal thickness for efficient coupling to surface plasmon mode is roughly between 490 nm and 600 nm. (c) is excerpted from the Kretschmann's paper[69]. (d) Shift of surface plasmon resonance peak due to the surface absorption. The peak is calculated for absorption of a 3nm layer of water (n=1.33) in air (n=1), which leads a measurable peak shift. SPR shifts from black to red curve.

99

A.1.3   Localized SPR (LSPR) of Nanoparticles

The parallel components of the wavevector (k_x) necessary for surface plamon excitation are also present in subwavelength confined modes near subwavelength apertures or metallic particles[48]. If such confined fields are brought close enough to a suitable interface, these nanostructures feature localized surface plasmon resonance (LSPR), the non-propagating excitation of the conduction electrons of a metallic nanostructure coupled to an EM field. Upon illumination, a nanoparticle both absorbs and scatters light, which leads to attenuation of the incident electromagnetic wave. We first assume the quasi-static approximation that neglects retardation effects: all points of an object respond simultaneously to an excitation field. This approximation is valid only if the size of the object is much smaller than the wavelength of light (Rayleigh particle, $a \ll \lambda$).

Let's consider a dielectric with N number of particles per unit volume in an external electric field E. The total field inside a single spherical particle in the dielectric can be approximated by $\vec{E}_{total} = \vec{E} + \vec{P}/(3\varepsilon_0)$, where $\vec{P}$ is the sum of the induced dipoles. Equations for the total dipole moment ($\vec{P}$, Equation A.10), for the induced dipole of an individual particle ($\vec{p}_i$, Equation A.11), and for their relationship (Equation A.12) are the following.

$$\vec{P} = \varepsilon_0(\varepsilon_r - 1)\vec{E} \tag{A.10}$$

$$\vec{p}_i = \alpha\vec{E}_{total} = \alpha(\vec{E} + \frac{\vec{P}}{3\varepsilon_0}) = \alpha\vec{E}(\frac{\varepsilon_r + 2}{3}) \qquad (A.11)$$

$$\vec{P} = N\vec{p}_i = N\alpha\vec{E}(\frac{\varepsilon_r + 2}{3}) \qquad (A.12)$$

Clausius-Mossotti relation (Equation A.13) for spherical particles can be derived by combining Equation A.10 and A.12.

$$\rightarrow \alpha = 3V \cdot \frac{\varepsilon_r - 1}{\varepsilon_r + 2} \qquad (A.13)$$

where V is the volume of the sphere and $\varepsilon_r = \varepsilon_r' + i\varepsilon_r''$ is the relative dielectric constant of the particle. This expression is applicable only to the Rayleigh particle where the quasi-static approximation is applied and the nanoparticle acts as an electric dipole. The scattering and absorption cross-sections are[129,18]

$$\sigma_{scatt} = \frac{8\pi}{3}k^4 |\alpha|^2 = \frac{8\pi}{3}k^4 a^6 \cdot \frac{(\varepsilon_r' - 1)^2 + \varepsilon_r''^2}{(\varepsilon_r' + 2)^2 + \varepsilon_r''^2} \qquad (A.14)$$

$$\sigma_{abs} = 4\pi k \Re(i\alpha) = 4\pi k a^3 \cdot \frac{(\varepsilon_r' - 1)^2 + \varepsilon_r''^2}{(\varepsilon_r' + 2)^2 + \varepsilon_r''^2} \qquad (A.15)$$

where $k = 2\pi/\lambda$, and a is the radius of the spherical particle. We can conclude that the analytical solution of the cross-sections show that LSPR happens when the real part of the relative permittivity is -2 ($\varepsilon_r' = -2$). For free Rayleigh particles in vacuum, resonance energies are calculated to be 3.48 eV for silver (near UV) and 2.6 eV for gold (blue)[111].

For larger particles similar or larger than the incident wavelength ($a \geq \lambda$), the phase of the driving field significantly changes over the particle volume, and the quasi-static approximation no more holds true. Mie theory involves a more rigorous electrodynamics approach to describe the scattering process of a small particle[63]. Maxwell's equations are solved in spherical coordinates through separation of variables. The incident plane wave is expanded in Legendre polynomials, and the solutions inside and outside the sphere can be matched at the boundary. Bessel and Hankel functions are used in the complex expression for simplification. The scattering cross-section is[18]

$$\sigma_{scatt} = \frac{1}{2k^2} (i_1 + i_2) \begin{cases} i_1 = \left| \sum_{n=1}^{\infty} \frac{2n+1}{n(n+1)} \left[a_n \pi_n cos\theta + b_n \tau_n cos\theta \right] \right|^2 \\ i_2 = \left| \sum_{n=1}^{\infty} \frac{2n+1}{n(n+1)} \left[a_n \tau_n cos\theta + b_n \pi_n cos\theta \right] \right|^2 \end{cases} \quad \text{(A.16)}$$

where π_n and τ_n are Legendre polynomials, and a_n and b_n are Bessel and Hankel functions. Equation A.16 can be algebraically solved using the tabulated bulk values for the nanoparticle[111]. The scattering and absorption cross-sections were calculated for a 100 nm gold nanosphere in air (Figure A.3a). The extinction cross-section, the sum of scattering and absorption cross-sections, showed a resonance feature at 522 nm, which is called localized surface plasmon resonance (LSPR). The peak and bandwidth of the cross-section resonance could be tuned by changing the size, the aspect ratio and by changing refractive index of the surrounding medium[111]. As shown in

Figure A.3b, even the slightest change in the dielectric surrounding led to a detectable shift of the resonance energy. That is the reason why metallic nanoparticles are very suitable for sensing applications. Placing a molecule in the vicinity of a nanoparticle effects the dielectric environment and therefore shifts the plasmon peak. Biosensing is one of the major applications for plasmonic nanoparticles[94,139,145,77,52]. We used this localized surface plasmon resonance (LSPR) properties of gold nanorods to use it as an interacellular sensor for label-free biomarkers.
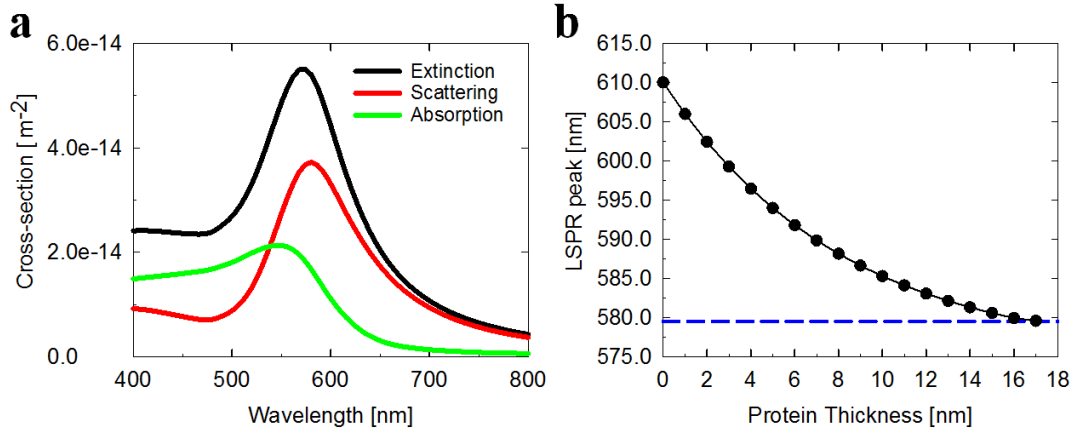
Figure A.3: Localized Surface Plasmon Resonance (LSPR) of nanoparticles. (a) Extinction, absorption and scattering cross-sections (C_{ext}, C_{abs}, C_{sca}, respectively) of a 100nm gold sphere in air. The cross sections are calculated with the Mie theory using the dielectric function values for gold[58]. (b) Resonance wavelength for a 100 nm gold nanosphere embedded in water (n=1.33) vs. increasing thickness of a layer with refractive index n=1.5. Blue dotted line is the resonance wavelength for an infinite layer thickness (homogenous refractive index change).

A.2   Microcanteliver

A mechanical FTP can be simplified as a cylindrical cantilever beam with its one end bound to a fixed support. This beam is assumed to have constant stiffness and mass density along the shaft, and is subjected to free vibration. Euler-Lagrange equation for beams, or the undamped equation of motion for beams without load, can be written as[85]

$$\frac{d^2}{dx^2}\{EI(x)\frac{d^2Y(x)}{dx^2}\} = \omega^2 m(x)Y(x) \tag{A.17}$$

where E is the modulus of rigidity of beam material, I is the moment of inertia of the beam cross-section, x is the distance from the fixed end, $Y(x)$ is the displacement in y direction at x in x direction, ω is the natural frequency, m is the mass per unit length, and ρ is the material density where $m(x) = \rho A(x)$. For a uniform beam under free vibration, Equation A.17 can be simplified as

$$\frac{d^4Y(x)}{dx^4} - \beta^4 Y(x) = 0, \ where \ \beta^4 = \frac{m\omega^2}{EI} \tag{A.18}$$

For a cantilever with a fixed end, the displacement and slope are zero at the fixed end, while the moment and shear are zero at the free end. Thus, the boundary conditions for a cantilever beam is following.

$$\begin{cases} at \ x = 0, \ Y(x) = 0, \ Y'(x) = 0 \\ at \ x = l, \ Y''(x) = 0, \ Y'''(x) = 0 \end{cases} \tag{A.19}$$

The solution (mode shape) of a motion equation meeting the boundary conditions is given as[35]

$$cos(\beta_n L)cosh(\beta_n L) = 1, \ where \ n = 1, 2, 3, ..., \infty \tag{A.20}$$

$$\rightarrow \begin{cases} \beta_1 L = 1.8751 \\ \beta_2 L = 4.6941 \\ \beta_3 L = 7.8548 \\ \beta_4 L = 10.9955 \end{cases} \tag{A.21}$$

The natural frequencies f_n for transverse vibration of a uniform beam can be written as

$$f_n = \frac{\omega_n}{2\pi} = \frac{(\beta_n L)^2}{2\pi} \sqrt{\frac{EI}{mL^4}} \tag{A.22}$$

Tabulated values for a micro-size cylinder similar to the end-portion nanowire at a mechanical FTP are following.

$L = 5 \cdot 10^{-4}$ m   Length of nanowire

$D = 6 \cdot 10^{-7}$ m   Cross-section diameter of nanowire

$E = 7.31 \cdot 10^{10}$ N/m^2 Young's modulus of silica

$\rho = 2203$ kg/m^3 Density of silica

$v = 0.17$ Poisson's ratio of silica

$A = 2.83 \cdot 10^{-13}$ m^2 Cross-section of a cylinderical nanowire ($=\pi D^2/4$)

$m = 6.23 \cdot 10^{-10}$ kg/m   Mass per unit length of nanowire ($=\rho A$)

$I = 6.36 \cdot 10^{-27}$ m^4 Moment of inertia of the beam cross-section ($=\pi D^4/64$)

Given Equation A.22 for mode frequency and numbers for the variables, the natural frequencies of the free vibration can be analytically obtained.

$$\rightarrow \begin{cases} f_1 = 12.1 \text{ kHz} \\ f_2 = 75.8 \text{ kHz} \\ f_3 = 212 \text{ kHz} \\ f_4 = 416 \text{ kHz} \end{cases} \tag{A.23}$$

This analytical results roughly matches in dimensions with the resonance frequency calculated via COMSOL multiphysics software (Figure 4.7). The discrepancy arises because the actual end-portion of the mechanical FTP is not a perfect cylinder but a tapered nanowire that linearly tapers from roughly 2 μm to 400 nm in diameter.

A mechanical FTP can be coated with sensitive materials to detect specific targeted analytes. Coating on the FTP surface produces nonlinearity on stiffness and damping, which makes the analytical modeling of coated composite structure challenging[115]. We used COMSOL to calculate the resonance frequency shift and the

required Q factor to measure due to the protein adsorption on the cantilever surface. Q factor describes how under-damped a resonator is and characterizes a resonator's bandwidth relative to its center frequency. Higher Q indicates a lower rate of energy loss relative to the stored energy of the resonator and the sharper resonance peak. The smaller required Q factor is favorable, because the detection resolution can be achieved even with the broader resonance. We simulated the vibration modes of a end-portion nanowire with 400 nm in ending diameter, 2 μm in starting diameter, and 400 μm in length (Figure A.4). Assuming the adsorbate as the protein which has 3 x 3 nm size and 60 kDa of the molecular weight, the monolayer adsorbate density was roughly $1 \cdot 10^{-5}$ kg/m^2. As shown in Figure A.4a, as the adsorbate density increases, the induced mechanical resonance shift increases proportionally and then saturates. The red vertical line indicates the standard saturation density, and we need at least Q of 100 for every modes (Figure A.4b). As shown in Figure A.4c and A.4d, the Q factor remains constant as the length varies, but the Q factor increases as the diameter increases due to the increased effective spring constant and the decreased mechanical resonance shift. Thus, it is optimal to fabricate the nanowire as thin as possible.
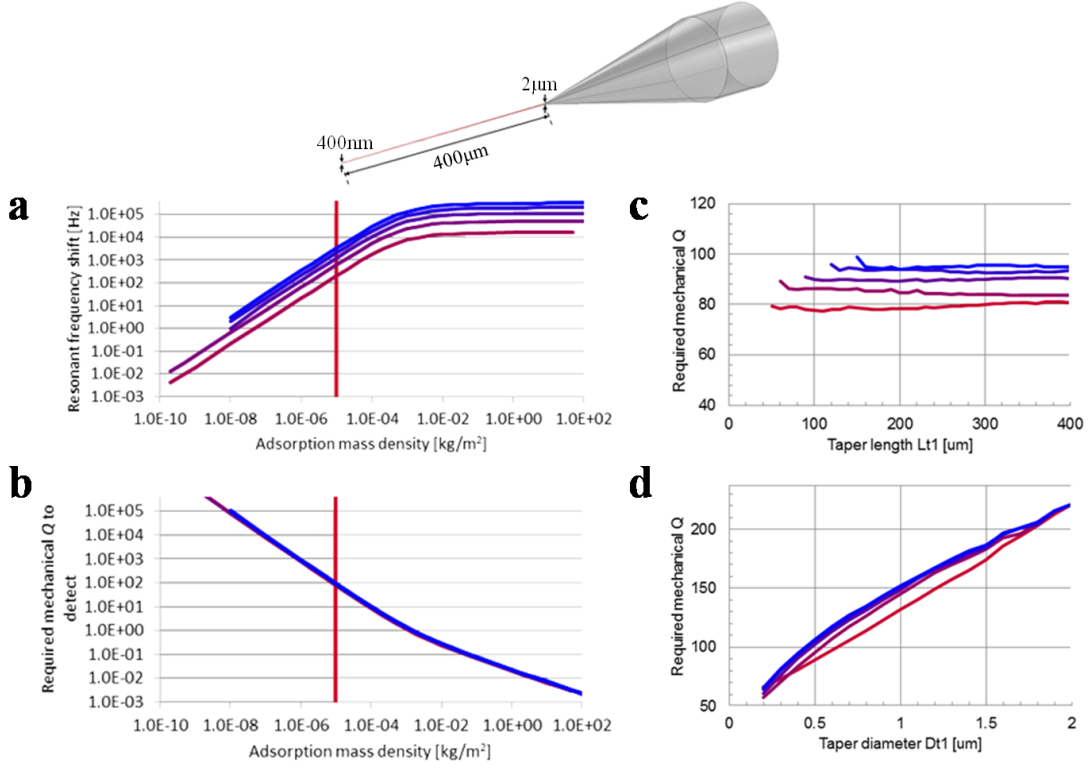
Figure A.4: COMSOL simulation result on protein adsorption on the surface of a mechanical FTP. Its end-portion nanowire has the taper diameter at the top = 400 nm, at the bottom = 2 μm, and the taper length = 400 μm (top). (a) Resonant frequency shift vs. adsorption mass density. Different color curves mean different vibration modes (red; lower, blue; higher order mode). Orthogonal red line against the x axis means the standard saturation density (= $1 \cdot 10^{-5}$ kg/m^2). (b) Required mechanical Q factor vs. adsorbed mass density. From this, we need at least Q of 100 to measure the saturated protein adsorption. (c) Required Q factor vs. end-portion nanowire length plot. (d) Required Q factor vs. end-portion nanowire diameter plot. Diameter betters be as small as possible for sensitive detection, because the required Q factor increases as the diameter increases.

A.3 Optical Trapping Force

Given an optical fiber tip with a metasurface that can focus light with high numerical aperture, we need to calculate if the gradient force acting on a nanoparticle when illuminated by a laser beam is large enough to trap a particle. As discussed in Section 4.1, optical response of a nanostructure can be often modeled as a collection of dipoles. For larger particles with $a \sim \lambda$ where quasi-static approximation to particles holds true, the retardation effects are considered by an expansion of the first TM mode of Mie's formulation, which provides an analytical formula for the complex polarizability of a spherical metal nanoparticle ($\alpha = \alpha' + i\alpha''$)[71].

$$\alpha_{Mie} = \frac{1 - (1/10)(\varepsilon_m(\omega) + \varepsilon_d)x^2 + O(x^4)}{\frac{1}{3} + \frac{\varepsilon_d}{\varepsilon_m(\omega) - \varepsilon_d} - \frac{1}{30}(\varepsilon_m(\omega) + 10\varepsilon_d)x^2 - i\frac{4\pi^2\varepsilon_d^{3/2}}{3}\frac{V}{\lambda^3} + O(x^4)} V \tag{A.24}$$

where $x = 2\pi a/\lambda$, ε_d is the dielectric constant of the medium, and $\varepsilon_m(\omega)$ is the dielectric constant of the metal particle. The real (α') and imaginary (α'') parts of the polarizability are calculated from Equation A.13 for Rayleigh particle and from Equation A.24 for 100 nm gold nanoparticle and permittivity from Johnson and Christy's paper[58]. As expected, both real and imaginary parts of the polarizability peak near the LSPR wavelength of gold spherical nanoparticle (Figure A.5a). As shown in Figure

A.5b, the scattering and absorption cross-sections could be calculated from Equation

A.14 and A.15 for Rayleigh particles. Both cross-sections show resonance features

at roughly 540 nm. This resonance peak is called localized surface plasmon reso-

nance (LSPR). For a dipolar particle with dimensions $a \sim \lambda$ irradiated by an arbitrary

monochromatic EM wave, the time averaged radiation-induced forces that are acting

on this dipole is the following[127].

$$\vec{F} = \frac{1}{4}\varepsilon_0\varepsilon\alpha'\nabla\left(\vec{E}\cdot\vec{E}\right) + \frac{1}{2}\varepsilon_0\varepsilon\alpha''Im\left(\sum_l \vec{E_l}\cdot\nabla\vec{E_l}\right) = \vec{F}_{grad} + \vec{F}_{scatt} \tag{A.25}$$

The gradient force originates from the gradient of the intensity profile of the in-

cident laser and is proportional to the real part of polarizability (α'), and the scattering

force is proportional to the imaginary part of polarizability (α''). A tightly focused

laser beam at the focus is required to trap a particle accelerated by the gradient force

towards intensity maxima of the radiation field. On the other hand, scattering force

represents the momentum transfer from the external radiation field due to the extinc-

tion of nanoparticle, and pushes the nanoparticle out of the trap. $\vec{F}_{grad} \gg \vec{F}_{scatt}$ is re-

quired for stable trapping. The analytical solution for the radial and z-components

of the gradient and scattering forces can be obtained[2]. Illumination with an inci-

dent laser off-resonance (1064 nm) from localized surface plasmon resonance (532

nm) will minimize the scattering force and allow stable trapping. This is because

α'' is largest at resonance wavelength and results in the large scattering force (532 nm), while α'' decays sharper than α' and results in dominating radiation force at off-resonance (1064 nm).

$$\begin{cases} F^r_{grad}(r,z) = -\frac{2\varepsilon_0}{\pi}\alpha' \left|\vec{E}_0\right|^2 r\frac{\omega_0^2}{\omega^4}\exp\left[-\frac{2r^2}{\omega^2}\right] \\ F^z_{grad}(r,z) = -\frac{\varepsilon_0}{\pi}\alpha' \left|\vec{E}_0\right|^2 z\frac{\omega_0^2}{z_0^2}\left(\frac{1}{\omega^4} - \frac{2r^2}{\omega^6}\right)\exp\left[-\frac{2r^2}{\omega^2}\right] \\ F^r_{scatt}(r,z) = \frac{\varepsilon_0}{\pi}\alpha'' \left|\vec{E}_0\right|^2 r\frac{\omega_0^2}{\omega^4}\frac{k}{R}\exp\left[-\frac{2r^2}{\omega^2}\right] \\ F^z_{scatt}(r,z) = \frac{\varepsilon_0}{\pi}\alpha'' \left|\vec{E}_0\right|^2 z\frac{\omega_0^2}{\omega^2}\left[k - \frac{kr^2\left(z^2-z_0^2\right)}{2\left(z^2+z_0^2\right)} - \frac{\omega_0^2}{z_0\omega^2}\right]\exp\left[-\frac{2r^2}{\omega^2}\right] \end{cases} \qquad (A.26)$$

where $\omega_0 = \lambda/(NA \cdot \pi)$ and $z_0 = \pi\omega_0^2\sqrt{\varepsilon_d}/\lambda$. The optical gradient forces experienced by nanoparticles are typically very weak, because the polarizability scales with the third power of the particle size (Equation A.13 and A.24). To confine nanoparticle against the destabilizing effects of thermal fluctuation, a significant optical power may be required: 15 mW for 100nm sphere and 1.5W for 10nm sphere silica in water[13]. However, since the free-electron plasma yields a large near-infrared (NIR) polarizability and a large effective spring constant in Drude-Sommerfeld model[116], 35nm gold nanoparticles can be trapped at much lower power (3.5 mW) in water[86]. Elongated plasmonic nanostructures such as gold nanorods can sustain plasmon resonances in a broad spectral region in the visible/NIR and results in even stronger trapping, radiation forces[106,97].
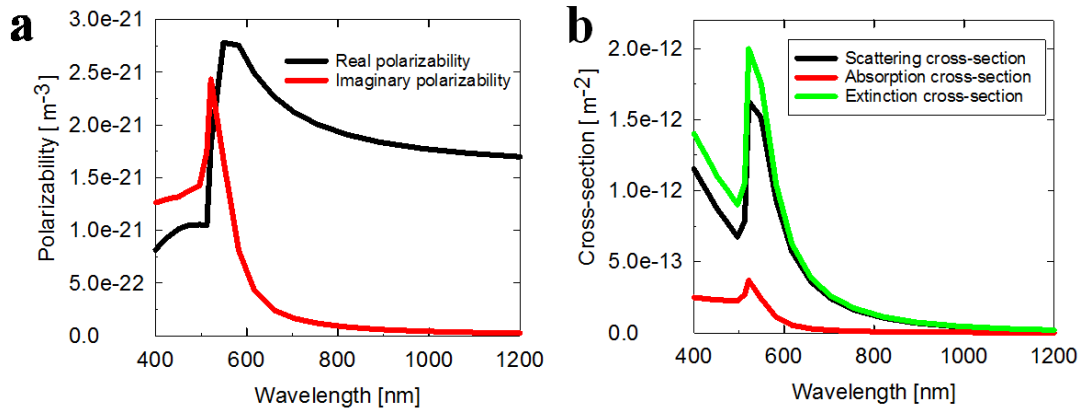
Figure A.5: Graph of analytical polarizability and cross-sections. (a) Real part and imaginary part of polarizability from Equation A.24. Both peak in visible range, but only the imaginary part decays to zero at higher wavelength. (b) Cross-sections from Equation A.14 and A.15 for Rayleigh particles ($a \ll \lambda$) in air. Extinction ross-sections peak at roughly 540 nm.

A.4 Statistics in Cell Biology

Many research findings in medical research papers are limited by prevailing bias, not variability, and thus are false or irreproducible[55,98]. Biologists often form conclusions solely on the basis of results statistically significant when evaluated by a p-value of less than .05, but this is not enough. In order to test the statistical significance, the repeats of experiments need to be conducted independently, and the replicates of experiments with the same sources of variability cannot be used to make statistical inference[130]. This section is to provide a basic understanding of statistics that can be useful to help in monitoring the conduct of experiments, in interpreting the results, and in presenting them in publications in cell biology field.

Much of today's research in cell biology require repeated experimentation to statistically conclude biological significance. Descriptive statistics is used to determine if the experiments were performed well, and inferential statistics is used to determine what conclusions and inferences are justified regarding the population, or the actual data. Descriptive statistics require only replicates to provide quality controls of the experimental conducts (n=1). Replicates cannot be used to form conclusions, and inferential statistics require independent repeats of the whole experiment (n > 1) to make inference on the main experimental questions. Different types of statistics are summarized in Table A.5.1, where x_i is the individual data, m is the sample mean, and

t_{n-1} is a critical value of t-statistics.

Statistics	Type	Formula
Range	Descriptive	$max(x_i) - min(x_i)$
Standard deviation (SD)	Descriptive	$SD = \sqrt{\sum_i \frac{(x_i-m)^2}{n-1}}$
Standard error (SE)	Inferential	$SE = \frac{SD}{\sqrt{n}}$
Confidence interval (CI)	Inferential	$m \pm t_{n-1} \cdot SE$

Table A.2: Basic properties of common error bars.

Descriptive statistics can be used to show how the data are distributed broadly or narrowly and can help determining the expected amount of variation. Two exemplary descriptive statistics are range and standard deviation (SD). The range is defined as the interval from the lowest sample value to the highest sample value. It is not often used, because one extreme outlier may define the entire statistical description.

A commonly used descriptive statistic is standard deviation (SD). SDs are calculated by taking square root of average of squared differences between samples and sample mean (m). In other words, SD is a measure to quantify the amount of variation or dispersion of sample values from sample mean. The $m \pm SD$ interval encompasses approximately 68% of the data points in normal distribution, regardless of how many samples there are.

Once cell biologists obtain reasonable SD and are satisfied that the experimental results are reliable, they can start analyzing the data and measure the accuracy of an estimate, to draw inferences and test hypotheses they are interested in. Inferential

statistics can help deciding whether preliminary results are worth repeating. The most

commonly used inferential statistics are standard error (SE) and confidence intervals

(CIs).

Standard error (SE) is referred to as an inferential statistic because it can help

you make inferences from the data. For example, if the data are normally distributed,

you can infer that the population mean (μ) will be within the interval: μ is within $m2SE$

for approximately 68% of the time when n is 3, and approximately 95% when n is 10

or greater. SE is defined as $SE = SD/\sqrt{n}$ and varies inversely with the square root of

n, so the more often an experiment is repeated, or the more samples are measured, the

smaller the SE becomes. This allows precise estimate of where the population mean

might lie.

Confidence interval (CI) is another inferential statistics that estimates a propor-

tion that the true value of the parameter (population parameter) will match the given

confidence level. Formally, 95% CI is defined as the interval that the true value of

the parameter is in our confidence interval for 95% times. CIs are calculated by mul-

tiplying the SE by the t-value, which Gosset used to monitor the quality of stout at

the Guinness Brewery. This critical t-value varies with n. As shown in Figure A.6a

for 95% CIs, t-value converges to 2 for n=10 or more; it increases for small n, and

for n=3 it is 4. Therefore, 95% CI intervals are roughly $m4SE$ (when n=3) and $m2SE$

(when n =10 or greater). For example, if a figure shows SE bars, you can double them

in width, to get approximate 95% CIs, as long as n is 10 or more. However, if n=3,

you need to multiply the SE bars by 4.

We can apply these statistical concepts when plotting Figure 3.7d and A.6b. To provide quality controls of the conduct of experiments, same FTP was used to measure same analyte compositions multiple times and produced replicates. We replicated five times by flowing 10nM p53 solution in PBS 1X and flushing with PBS 1X on the same FTP device. Sample mean, SD and SE of LSPR shift were 4.7, 0.53, 0.24 respectively. We tested with different concentrations of p53 on the same device and proved its robustness to measure reliably (Figure 3.7a and 3.7b). Small SD and SE proves that we can reliably obtain data in physiological environment. Next, we repeated the whole experiment independently with different FTPs functionalized with different antibodies to make inferential conclusion that FTP demonstrates well-defined antibody-antigen specificity and tolerance to non-specific bindings. Five FTPs are used for measurements for each antibody-antigen pair. Since we tested 6 sets of different antibody-antigen pairs, 30 FTPs were experimented in total. In Figure A.6b, from left to right, red error bar indicates SE, black error indicates SD, and blue error bar indicates 95% CI (two-tailed t-value = 2.6 for n=5).

The probability value (p-value) in null hypothesis significance testing is the probability of wrongly rejecting the null hypothesis if it is in fact true. In other words, a small p-value ($\leq .05$) indicates strong evidence against the null hypothesis so it is rejected, and a large p-value ($> .05$) indicates weak evidence against the null hypothesis so it cannot be rejected. Setting a null hypothesis that there is no difference in

response to p53 and to TNF-α on anti-p53-functionalized LSPR FTP ($\Delta LSPR_{p53} = \Delta LSPR_{TNF-\alpha}$), we can obviously reject null hypothesis (p-value < .0001). However, if the null hypothesis states no difference in response to p53 and to p53+1% BSA on anti-p53-functionalized LSPR FTP ($\Delta LSPR_{p53} = \Delta LSPR_{p53+BSA}$), we cannot reject null hypothesis, so the difference in two LSPR shifts may not be significant (p-value > .05).

In summary, we can use (1) descriptive statistics such as range or standard deviation (SD) to monitor the conduct of experiments and to make sure they were performed well and (2) inferential statistics such as standard error (SE) or confidence interval (CI) to estimate the true parameters (polulation) and determine what conclusions and inferences are justified. Independent repeats of the whole experiment (n > 1), not simple replicates, is required to apply statistical inference. 95% CI intervals are roughly $m \pm 2SE$ when n=10 or greater, and thus at least n > 10 is preferred to base conclusions on statistical grounds.
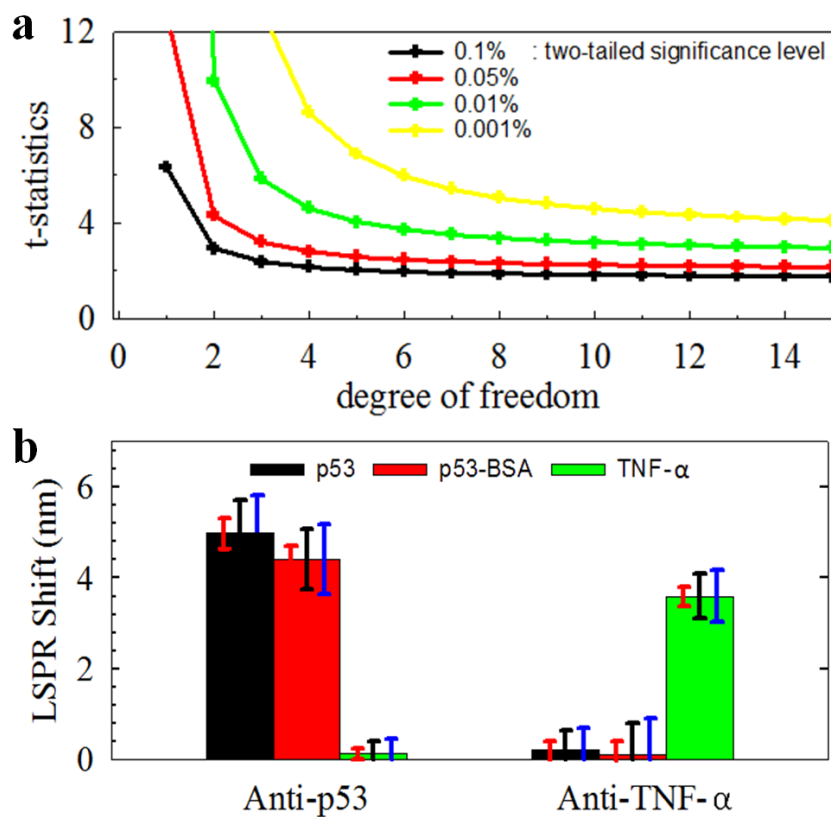
Figure A.6: Proper use of descriptive and inferential error bars. (a) T-value vs. degree of freedom (dof) at different two-tailed significance levels. For all significance levels, t-value decreases as dof increases. (b) Different sets of error bars for specificity test of LSP-FTP sensor (Figure 3.7d). SE (red), SD (black), and 95% CI (blue) are shown for all antibody-antigen pairs each repeated for 5 times. T-value is 2.6 at n=5, and $\sqrt{5}$ is 2.2. According to the equations in Table A.2, SD is roughly $2.2 \cdot SE$ and 95% CI is $2.6 \cdot SE$.

References

[1] Acosta, V. M., Bauch, E., Ledbetter, M. P., Waxman, A., Bouchard, L. S., & Budker, D. (2010). Temperature dependence of the nitrogen-vacancy magnetic resonance in diamond. *Physical Review Letters*, 104(7), 070801.

[2] Agayan, R. R., Gittes, F., Kopelman, R., & Schmidt, C. F. (2002). Optical trapping near resonance absorption. *Applied Optics*, 41(12), 2318–2327.

[3] Aieta, F., Genevet, P., Kats, M. A., Yu, N., Blanchard, R., Gaburro, Z., & Capasso, F. (2012). Aberration-free ultrathin flat lenses and axicons at telecom wavelengths based on plasmonic metasurfaces. *Nano Letters*, 12(9), 4932–4936.

[4] Aikens, C. M. & Schatz, G. C. (2006). TDDFT studies of absorption and SERS spectra of pyridine interacting with Au20. *Journal of Physical Chemistry A*, 110(49), 13317–13324.

[5] Altschuler, S. J. & Wu, L. F. (2010). Cellular heterogeneity: do differences make a difference? *Cell*, 141(4), 559–563.

[6] Ament, I., Prasad, J., Henkel, A., Schmachtel, S., & Sönnichsen, C. (2012). Single unlabeled protein detection on individual plasmonic nanoparticles. *Nano Letters*, 12(2), 1092–1095.

[7] Ang, P. K., Wang, S., Bao, Q., Thong, J. T. L., & Loh, K. P. (2009). High-throughput synthesis of graphene by intercalation-exfoliation of graphite oxide and study of ionic screening in graphene transistor. *ACS Nano*, 3(11), 3587–3594.

[8] Angle, M. R., Wang, A., Thomas, A., Schaefer, A. T., & Melosh, N. A. (2014). Penetration of cell membranes and synthetic lipid bilayers by nanoprobes. *Biophysical Journal*, 107(9), 2091–2100.

[9] Anker, J. N., Hall, W. P., Lyandres, O., Shah, N. C., Zhao, J., & Van Duyne, R. P. (2008). Biosensing with plasmonic nanosensors. *Nature Materials*, 7(6), 442–453.

[10] Arabi, H. E., An, S., & Oh, K. (2010). Fiber optic engine for micro projection display. *Optics Express*, 18(5), 4655–4663.

REFERENCES

[11] Arbabi, A., Horie, Y., Bagheri, M., & Faraon, A. (2015). Dielectric meta-surfaces for complete control of phase and polarization with subwavelength spatial resolution and high transmission. *Nature Nanotechnology*, 10(11), 937–943.

[12] Arlett, J. L., Myers, E. B., & Roukes, M. L. (2011). Comparative advantages of mechanical biosensors. *Nature Nanotechnology*, 6(4), 203–215.

[13] Ashkin, a., Dziedzic, J. M., Bjorkholm, J. E., & Chu, S. (1986). Observation of a single-beam gradient force optical trap for dielectric particles. *Optics Letters*, 11(5), 288–290.

[14] Bareil, P. B. & Sheng, Y. (2010). Angular and position stability of a nanorod trapped in an optical tweezers. *Optics Express*, 18(25), 26388–26398.

[15] Batchelor, E., Loewer, A., Mock, C., & Lahav, G. (2011). Stimulus-dependent dynamics of p53 in single cells. *Molecular Systems Biology*, 7, 488.

[16] Bayat, K., Choy, J., Farrokh Baroughi, M., Meesala, S., & Loncar, M. (2014). Efficient, uniform, and large area microwave magnetic coupling to NV centers in diamond using double split-ring resonators. *Nano Letters*, 14(3), 1208–1213.

[17] Betzig, E., Lewis, A., Harootunian, A., Isaacson, M., & Kratchmer, E. (1986). Near-field scanning optical microscopy (NSOM). *Biophysical Journal*, 49(10), 269–279.

[18] Bohren, C. F. & Huffman, D. R. (2008). *Absorption and scattering of light by small particles*. John Wiley & Sons.

[19] Boldo, E., Medina, S., LeTertre, A., Hurley, F., Mücke, H.-G., Ballester, F., Aguilera, I., & Eilstein, D. (2006). Apheis: Health impact assessment of long-term exposure to PM2.5 in 23 European cities. *European Journal of Epidemi-ology*, 21(6), 449–458.

[20] Boubel, R. W., Vallero, D., Fox, D. L., Turner, B., & Stern, A. C. (2013). *Fundamentals of air pollution*. Elsevier.

[21] Brolo, A. (2012). Plasmonics for future biosensors. *Nature Photonics*, 6(11), 709–713.

[22] Burek, M. J. (2016). *Free-standing nanomechanical and nanophotonic structures in single-crystal diamond*. PhD thesis, Harvard University.

[23] Burek, M. J., Chu, Y., Liddy, M. S. Z., Patel, P., Rochman, J., Meesala, S., Hong, W., Quan, Q., Lukin, M. D., & Lončar, M. (2014). High-Q optical nanocavities in bulk single-crystal diamond. *Nature Communications*, 5, 5718.

[24] Canning, J., Sommer, K., Huntington, S., & Carter, A. (2001). Silica-based fibre Fresnel lens. *Optics Communications*, 199(5-6), 375–381.

[25] Cao, Y. C., Jin, R., & Mirkin, C. a. (2002). Nanoparticles with Raman spectroscopic fingerprints for DNA and RNA detection. *Science*, 297(5586), 1536–1540.

[26] Chen, H., Shao, L., Woo, K. C., Ming, T., Lin, H. Q., & Wang, J. (2009). Shape-dependent refractive index sensitivities of gold nanocrystals with the same plasmon resonance wavelength. *Journal of Physical Chemistry C*, 113(41), 17691–17697.

[27] Chen, X. D., Dong, C. H., Sun, F. W., Zou, C. L., Cui, J. M., Han, Z. F., & Guo, G. C. (2011). Temperature dependent energy level shifts of nitrogen-vacancy centers in diamond. *Applied Physics Letters*, 99(16), 2009–2012.

[28] Chin, J. (2010). Selecting a mouse model of alzheimer's disease. *Methods in Molecular Biology 2*, 670, 169–189.

[29] Choi, S. H., Kim, Y. H., Hebisch, M., Sliwinski, C., Lee, S., D'Avanzo, C., Chen, H., Hooli, B., Asselin, C., Muffat, J., Klee, J. B., Zhang, C., Wainger, B. J., Peitz, M., Kovacs, D. M., Woolf, C. J., Wagner, S. L., Tanzi, R. E., & Kim, D. Y. (2014). A three-dimensional human neural cell culture model of Alzheimer's disease. *Nature*, 515(7526), 274–278.

[30] Dephoure, N., Gould, K. L., Gygi, S. P., & Kellogg, D. R. (2013). Mapping and analysis of phosphorylation sites: a quick guide for cell biologists. *Molecular Biology of the Cell*, 24(5), 535–542.

[31] Doherty, M. W., Struzhkin, V. V., Simpson, D. A., McGuinness, L. P., Meng, Y., Stacey, A., Karle, T. J., Hemley, R. J., Manson, N. B., Hollenberg, L. C. L., & Prawer, S. (2014). Electronic properties and metrology applications of the diamond NV - Center under pressure. *Physical Review Letters*, 112(4), 047601.

[32] Dolan, P., Li, X., Storteboom, J., & Gu, M. (2014). Complete determination of the orientation of NV centers with radially polarized beams. *Optics Express*, 22(4), 4379–4387.

[33] Dolde, F., Fedder, H., Doherty, M. W., Noebauer, T., Rempp, F., Balasubramanian, G., Wolf, T., Reinhard, F., Hollenberg, L. C. L., Jelezko, F., Wrachtrup, J., & Nöbauer, T. (2011). Electric-field sensing using single diamond spins. *Nature Physics*, 7(6), 459–463.

REFERENCES

[34] Dong, Y., Wu, X., Xu, Z., Zhang, Y., & Xie, Z. (2012). Anesthetic isoflurane increases phosphorylated tau levels mediated by caspase activation and Aβ generation. *PLoS ONE*, 7(6), 1–12.

[35] DUKKIPATI, V. R. A. O. & Srinivas, J. (2012). *Textbook of mechanical vibrations*. PHI Learning Pvt. Ltd.

[36] García-Vidal, F. J. & Pendry, J. B. (1996). Collective theory for surface enhanced Raman scattering. *Physical Review Letters*, 77(6), 1163–1166.

[37] Giepmans, B., Adams, S., Ellisman, M., & Tsien, R. (2006). The fluorescent toolbox for assessing protein location and function. *Science*, 312(5771), 217–224.

[38] Gómez-Martínez, R., Hernández-Pinto, A. M., Duch, M., Vázquez, P., Zinoviev, K., de la Rosa, E. J., Esteve, J., Suárez, T., & Plaza, J. A. (2013). Silicon chips detect intracellular pressure changes in living cells. *Nature Nanotechnology*, 8(7), 517–521.

[39] Gong, Y., Ye, A.-Y., Wu, Y., Rao, Y.-J., Yao, Y., & Xiao, S. (2013). Graded-index fiber tip optical tweezers: numerical simulation and trapping experiment. *Optics Express*, 21(13), 16181–16190.

[40] Grinolds, M., Hong, S., Maletinsky, P., & Luan, L. (2013). Nanoscale magnetic imaging of a single electron spin under ambient conditions. *Nature Physics*, 9(4), 215–219.

[41] Gupta, A., Akin, D., & Bashir, R. (2004). Single virus particle mass detection using microresonators with nanoscale thickness. *Applied Physics Letters*, 84(11), 1976–1978.

[42] Haber, L. H., Schaller, R. D., Johnson, J. C., & Saykally, R. J. (2004). Shape control of near-field probes using dynamic meniscus etching. *Journal of Microscopy*, 214(1), 27–35.

[43] Hall, L. T., Beart, G. C. G., Thomas, E. A., Simpson, D. A., McGuinness, L. P., Cole, J. H., Manton, J. H., Scholten, R. E., Jelezko, F., Wrachtrup, J., Petrou, S., & Hollenberg, L. C. L. (2012). High spatial and temporal resolution wide-field imaging of neuron activity using quantum NV-diamond. *Scientific Reports*, 2, 401.

[44] Hamill, O. P., Marty, A., Neher, E., Sakmann, B., & Sigworth, F. J. (1981). Improved patch-clamp techniques for high-resolution current recording from cells and cell-free membrane patches. *Pflügers Archiv European Journal of Physiology*, 391(2), 85–100.

REFERENCES

[45] Han, D., Lim, S. Y., Kim, B. J., Piao, L., & Chung, T. D. (2010). Mercury(ii) detection by SERS based on a single gold microshell. *Chemical Communications*, 46(30), 5587–5589.

[46] Hansen, P. M., Bhatia, V. K., Harrit, N., & Oddershede, L. (2005). Expanding the optical trapping range of gold nanoparticles. *Nano Letters*, 5(10), 1937–1942.

[47] Hardy, J. & Selkoe, D. J. (2002). The amyloid hypothesis of Alzheimer's disease: progress and problems on the road to therapeutics. *Science*, 297(5580), 353–356.

[48] Hecht, B., Bielefeldt, H., Novotny, L., Inouye, Y., & Pohl, D. (1996). Local excitation, scattering, and interference of surface plasmons. *Physical Review Letters*, 77(9), 1889–1892.

[49] Higgins, G. a. & Jacobsen, H. (2003). Transgenic mouse models of Alzheimer's disease: phenotype and application. *Behavioural Pharmacology*, 14(5-6), 419–438.

[50] Hoffmann, P., Dutoit, B., & Salathé, R.-P. (1995). Comparison of mechanically drawn and protection layer chemically etched optical fiber tips. *Ultramicroscopy*, 61(1-4), 165–170.

[51] Homola, J., Yee, S. S., & Gauglitz, G. (1999). Surface plasmon resonance sensors: review. *Sensors and Actuators B*, 54(1-2), 3–15.

[52] Hong, W., Liang, F., Schaak, D., Loncar, M., & Quan, Q. (2014). Nanoscale label-free bioprobes to detect intracellular proteins in single living cells. *Scientific Reports*, 4, 6179.

[53] Hübinger, G., Geis, S., LeCorre, S., Mühlbacher, S., Gordon, S., Fracasso, R. P., Hoffman, F., Ferrand, S., Klafki, H. W., & Roder, H. M. (2008). Inhibition of PHF-like tau hyperphosphorylation in SH-SY5Y cells and rat brain slices by K252a. *Journal of Alzheimer's Disease*, 13(3), 281–294.

[54] Ilic, B., Czaplewski, D., Craighead, H. G., Neuzil, P., Campagnolo, C., & Batt, C. (2000). Mechanical resonant immunospecific biological detector. *Applied Physics Letters*, 77(3), 450–452.

[55] Ioannidis, J. P. A. (2005). Why most published research findings are false. *PLoS Medicine*, 2(8), 0696–0701.

[56] Ivády, V., Simon, T., Maze, J. R., Abrikosov, I. a., & Gali, A. (2014). Pressure and temperature dependence of the zero-field splitting in the ground state of

NV centers in diamond: A first-principles study. *Physical Review B*, 90(23), 235205.

[57] Jauffred, L., Taheri, S. M.-R., Schmitt, R., Linke, H., & Oddershede, L. B. (2015). Optical trapping of gold nanoparticles in air. *Nano Letters*, 15(7), 4713–4719.

[58] Johnson, P. B. & Christy, R. W. (1972). Optical constants of the noble metals. *Physical Review B*, 6(12), 4370–4379.

[59] Kalkbrenner, T., Ramstein, M., Mlynek, J., & Sandoghdar, V. (2001). A single gold particle as a probe for apertureless scanning near-field optical microscopy. *Journal of Microscopy*, 202(1), 72–76.

[60] Käll, M. (2012). Biosensors: One molecule at a time. *Nature Nanotechnology*, 7(6), 347–349.

[61] Karlsson, R. & Fält, A. (1997). Experimental design for kinetic analysis of protein-protein interactions with surface plasmon resonance biosensors. *Journal of Immunological Methods*, 200(1), 121–133.

[62] Kastelic, D., Frković-Grazio, S., Baty, D., Truan, G., Komel, R., & Pompon, D. (2009). A single-step procedure of recombinant library construction for the selection of efficiently produced llama VH binders directed against cancer markers. *Journal of Immunological Methods*, 350(1), 54–62.

[63] Kerker, M. (2013). *The scattering of light and other electromagnetic radiation: physical chemistry: A series of monographs*, volume 16. Academic Press.

[64] Khosravi, R., Maya, R., Gottlieb, T., Oren, M., Shiloh, Y., & Shkedy, D. (1999). Rapid ATM-dependent phosphorylation of MDM2 precedes p53 accumulation in response to DNA damage. *Proceedings of the National Academy of Sciences*, 96(26), 14973–14977.

[65] Kittel, C. (2004). *Introduction to solid state physics*, volume 8. John Wiley and Sons.

[66] Kleinman, S. L., Ringe, E., Valley, N., Wustholz, K. L., Phillips, E., Scheidt, K. A., Schatz, G. C., & Van Duyne, R. P. (2011). Single-molecule surface-enhanced raman spectroscopy of crystal violet isotopologues: Theory and experiment. *Journal of the American Chemical Society*, 133(11), 4115–4122.

[67] Kneipp, K., Wang, Y., Kneipp, H., Perelman, L. T., Itzkan, I., Dasari, R. R., & Feld, M. S. (1997). Single molecule detection using surface-enhanced Raman scattering (SERS). *Physical Review Letters*, 78(9), 1667–1670.

REFERENCES

[68] Kokavecz, J. & Mechler, A. (2008). Spring constant of microcantilevers in fundamental and higher eigenmodes. *Physical Review B*, 78(17), 172101.

[69] Kretschmann, E. (1971). Die bestimmung optischer konstanten von metallen durch anregung von oberflächenplasmaschwingungen. *Zeitschrift für Physik*, 241(4), 313–324.

[70] Kucsko, G., Maurer, P. C., Yao, N. Y., Kubo, M., Noh, H. J., Lo, P. K., Park, H., & Lukin, M. D. (2013). Nanometre-scale thermometry in a living cell. *Nature*, 500(7460), 54–58.

[71] Kuwata, H., Tamaru, H., Esumi, K., & Miyano, K. (2003). Resonant light scattering from metal nanoparticles: Practical analysis beyond rayleigh approximation. *Applied Physics Letters*, 83(22), 4625–4627.

[72] Lakowicz, J. R. (2013). *Principles of fluorescence spectroscopy*. Springer Science & Business Media.

[73] Langmuir, I. (1918). The adsorption of gases on plane surfaces of glass, mica and platinum. *Journal of the American Chemical Society*, 40(9), 1361–1403.

[74] Le Corre, S., Klafki, H. W., Plesnila, N., Hübinger, G., Obermeier, A., Sahagún, H., Monse, B., Seneci, P., Lewis, J., Eriksen, J., Zehr, C., Yue, M., McGowan, E., Dickson, D. W., Hutton, M., & Roder, H. M. (2006). An inhibitor of tau hyperphosphorylation prevents severe motor impairments in tau transgenic mice. *Proceedings of the National Academy of Sciences of the United States of America*, 103(25), 9673–9678.

[75] Lee, J. Y., Lee, C. W., Lin, E. H., & Wei, P. K. (2008). Single live cell refractometer using nanoparticle coated fiber tip. *Applied Physics Letters*, 93(17), 2006–2009.

[76] Li, M., Lohmüller, T., & Feldmann, J. (2015). Optical injection of gold nanoparticles into living cells. *Nano Letters*, 15(1), 770–775.

[77] Liang, F., Zhang, Y., Hong, W., Dong, Y., & Xie, Z. (2016). Direct tracking of amyloid and Tau dynamics in neuroblastoma cells using nanoplasmonic fiber tip probes. *Nano Letters (Submitted)*.

[78] Lichtman, J. & Conchello, J.-A. (2005). Fluorescence microscopy. *Nature Methods*, 2(12), 910–919.

[79] Lippincott-Schwartz*, J., Patterson, G. H., & Lippincott-schwartz, J. (2003). Development and use of fluorescent protein markers in living cells. *Science*, 300(5616), 87–91.

REFERENCES

[80] Liu, Y., Xu, H., Stief, F., Zhitenev, N., & Yu, M. (2011). Far-field superfocusing with an optical fiber based surface plasmonic lens made of nanoscale concentric annular slits. *Optics Express*, 19(21), 20233–20243.

[81] Ma, R.-H., Lee, C.-Y., Wang, Y.-H., & Chen, H.-J. (2008). Microcantilever-based weather station for temperature, humidity and flow rate measurement. *Microsystem Technologies-Micro-and Nanosystems-Information Storage and Processing Systems*, 14(7), 971–977.

[82] Macek, B., Mann, M., & Olsen, J. V. (2009). Global and site-specific quantitative phosphoproteomics: principles and applications. *Annual Review of Pharmacology and Toxicology*, 49(1), 199–221.

[83] Mamin, H. J., Kim, M., Sherwood, M. H., Rettner, C. T., Ohno, K., Awschalom, D. D., & Rugar, D. (2013). Nanoscale nuclear magnetic resonance with a nitrogen-vacancy spin sensor. *Science*, 339(6119), 557–560.

[84] Maruyama, K., Ohkawa, H., Ogawa, S., Ueda, A., Niwa, O., & Suzuki, K. (2006). Fabrication and characterization of a nanometer-sized optical fiber electrode based on selective chemical etching for scanning electrochemical/optical microscopy. *Analytical Chemistry*, 78(6), 1904–1912.

[85] Meirovitch, L. (1967). *Analytical methods in vibration*, volume 16. Macmillan.

[86] Messina, E., Cavallaro, E., Cacciola, A., Saija, R., Borghese, F., Denti, P., Fazio, B., D'Andrea, C., Gucciardi, P. G., Iatì, M. A., Meneghetti, M., Compagnini, G., Amendola, V., & Maragò, O. M. (2011). Manipulation and raman spectroscopy with optically trapped metal nanoparticles obtained by pulsed laser ablation in liquids. *Journal of Physical Chemistry C*, 115(12), 5115–5122.

[87] Michaelis, L. & Menten, M. L. (1913). Die kinetik der invertinwirkung. *Biochem Z*, 49, 333–369.

[88] Moffitt, J. R., Chemla, Y. R., Smith, S. B., & Bustamante, C. (2008). Recent advances in optical tweezers. *Annual Review of Biochemistry*, 77(1), 205–228.

[89] Mononobe, S., Maheswari, R. U., & Ohtsu, M. (1997). Fabrication of a pencil-shaped fiber probe with a nanometric protrusion from a metal film for near-field optical microscopy. *Optics Express*, 1(8), 229–233.

[90] Morisawa, M., Amemiya, Y., & Kohzu, H. (2001). Plastic optical fibre sensor for detecting. *Measurement Science and Technology*, 877(7), 877–881.

126

REFERENCES

[91] Nath, N. & Chilkoti, A. (2004). Label-free biosensing by surface plasmon resonance of nanoparticles on glass: Optimization of nanoparticle size. *Analytical Chemistry*, 76(18), 5370–5378.

[92] Neumann, P., Jakobi, I., Dolde, F., Burk, C., Reuter, R., Waldherr, G., Honert, J., Wolf, T., Brunner, A., Shim, J. H., Suter, D., Sumiya, H., Isoya, J., & Wrachtrup, J. (2013). High-precision nanoscale temperature sensing using single defects in diamond. *Nano Letters*, 13(6), 2738–2742.

[93] Nie, S. (1997). Probing single molecules and single nanoparticles by surface-enhanced Raman scattering. *Science*, 275(5303), 1102–1106.

[94] Nusz, G. J., Marinakos, S. M., Curry, A. C., Dahlin, A., Hook, F., Wax, A., & Chilkoti, A. (2008). Label-free plasmonic detection of biomolecular binding by a single gold nanorod. *Analytical Chemistry*, 80(4), 984–989.

[95] N.W. Ashcroft, N. M. (1976). *Solid state physics*. Saunders College.

[96] Ohtsu, M. (2012). *Near-field nano/atom optics and technology*. Springer Science & Business Media.

[97] Pelton, M., Liu, M., Kim, H. Y., Smith, G., Guyot-Sionnest, P., & Scherer, N. F. (2006). Optical trapping and alignment of single gold nanorods by using plasmon resonances. *Optics Letters*, 31(13), 2075–2077.

[98] Prinz, F., Schlange, T., & Asadullah, K. (2011). Believe it or not: how much can we rely on published data on potential drug targets? *Nature Reviews. Drug Discovery*, 10(9), 712–713.

[99] Purvis, J. E., Karhohs, K. W., Mock, C., Batchelor, E., Loewer, A., & Lahav, G. (2012). P53 dynamics control cell fate. *Science*, 336(6087), 1440–1444.

[100] Qian, X.-M. & Nie, S. M. (2008). Single-molecule and single-nanoparticle SERS: from fundamental mechanisms to biomedical applications. *Chemical Society Reviews*, 37(5), 912–920.

[101] Robinson, J. T., Jorgolli, M., Shalek, A. K., Yoon, M.-H. H., Gertner, R. S., & Park, H. (2012). Vertical nanowire electrode arrays as a scalable platform for intracellular interfacing to neuronal circuits. *Nature Nanotechnology*, 7(3), 180–184.

[102] Rogers, L. W. W. & G (1985). Humidity sensitive MIS structure. *Journal of Physics E*, 18(7), 577–581.

REFERENCES

[103] Saxena, S., Chaudhary, R. P., Singh, A., Awasthi, S., & Shukla, S. (2014). Plasmonic micro lens for extraordinary transmission of broadband light. *Scientific Reports*, 4, 5586.

[104] Schnell, U., Dijk, F., Sjollema, K. A., & Giepmans, B. N. G. (2012). Immunolabeling artifacts and the need for live-cell imaging. *Nature Methods*, 9(2), 152–158.

[105] Seaton, A., MacNee, W., Donaldson, K., & Godden, D. (1995). Particulate air pollution and acute health effects. *Lancet*, 345(8943), 176–178.

[106] Selhuber-Unkel, C., Zins, I., Schubert, O., Sönnichsen, C., & Oddershede, L. B. (2008). Quantitative optical trapping of single gold nanorods. *Nano Letters*, 8(9), 2998–3003.

[107] Shambat, G., Kothapalli, S. R., Provine, J., Sarmiento, T., Harris, J., Gambhir, S. S., & Vučković, J. (2013). Single-cell photonic nanocavity probes. *Nano Letters*, 13(11), 4999–5005.

[108] Singer, W., Nieminen, T. A., Gibson, U. J., Heckenberg, N. R., & Rubinsztein-Dunlop, H. (2006). Orientation of optically trapped nonspherical birefringent particles. *Physical Review E*, 73(2), 021911.

[109] Singhal, R., Orynbayeva, Z., Kalyana Sundaram, R. V., Niu, J. J., Bhattacharyya, S., Vitol, E. a., Schrlau, M. G., Papazoglou, E. S., Friedman, G., & Gogotsi, Y. (2011). Multifunctional carbon-nanotube cellular endoscopes. *Nature Nanotechnology*, 6(1), 57–64.

[110] Small, S. A. & Duff, K. (2009). Linking Aβ and Tau in late-onset Alzheimer's disease: A dual dathway hypothesis. *Neuron*, 60(4), 534–542.

[111] Sönnichsen, C., Franzl, T., Wilk, T., von Plessen, G., Feldmann, J., Wilson, O., & Mulvaney, P. (2002). Drastic reduction of plasmon damping in gold nanorods. *Physical Review Letters*, 88(7), 077402.

[112] Stadler, C., Rexhepaj, E., Singan, V. R., Murphy, R. F., Pepperkok, R., Uhlén, M., Simpson, J. C., & Lundberg, E. (2013). Immunofluorescence and fluorescent-protein tagging show high correlation for protein localization in mammalian cells. *Nature Methods*, 10(4), 315–323.

[113] Steen, H. & Mann, M. (2004). The ABC's (and XYZ's) of peptide sequencing. *Nature Reviews. Molecular Cell Biology*, 5(9), 699–711.

[114] Stewart, M. P., Helenius, J., Toyoda, Y., Ramanathan, S. P., Muller, D. J., & Hyman, A. a. (2011). Hydrostatic pressure and the actomyosin cortex drive mitotic cell rounding. *Nature*, 469(7329), 226–230.

REFERENCES

[115] Sun, W., Liu, Y., & Du, G. (2015). Analytical modeling of hard-coating cantilever composite plate considering the material nonlinearity of hard coating. *Mathematical Problems in Engineering*, 2015, 978392.

[116] Svoboda, K. & Block, S. M. (1994). Optical trapping of metallic Rayleigh particles. *Optics Letters*, 19(13), 930–932.

[117] Tadepalli, S., Kuang, Z., Jiang, Q., Liu, K.-k., & Fisher, M. A. (2015). Peptide functionalized gold nanorods for the sensitive detection of a cardiac biomarker using plasmonic paper devices. *Scientific Reports*, 5, 16206.

[118] Tan, W., Shi, Z. Y., Smith, S., Birnbaum, D., & Kopelman, R. (1992). Submicrometer intracellular chemical optical fiber sensors. *Science*, 258(5083), 778–781.

[119] Taylor, J. M., Cappellaro, P., Childress, L., Jiang, L., Budker, D., Hemmer, P. R., Yacoby, A., Walsworth, R., & Lukin, M. D. (2008). High-sensitivity diamond magnetometer with nanoscale resolution. *Nature Physics*, 4(10), 810–816.

[120] Terakawa, M. & Tanaka, Y. (2011). Dielectric microsphere mediated transfection using a femtosecond laser. *Optics Letters*, 36(15), 2877–2879.

[121] Thierry, B., Ng, J., Krieg, T., & Griesser, H. J. (2009). A robust procedure for the functionalization of gold nanorods and noble metal nanoparticles. *Chemical Communications*, 1(13), 1724–1726.

[122] Thundat, T., Chen, G. Y., Wannack, R. J., Allison, D. P., & Wachter, E. A. (1995). Vapor detection using resonating microcantilevers. *Analytical Chemistry*, 67(3), 519–521.

[123] Tian, B., Cohen-Karni, T., Qing, Q., Duan, X., Xie, P., & Lieber, C. M. (2010). Three-dimensional, flexible nanoscale field-effect transistors as localized bioprobes. *Science*, 329(5993), 830–834.

[124] Tian, B. & Lieber, C. M. (2013). Synthetic nanoelectronic probes for biological cells and tissues. *Annual Review of Analytical Chemistry*, 6, 31–51.

[125] Tong, L., Gattass, R. R., Ashcom, J. B., He, S., Lou, J., Shen, M., Maxwell, I., & Mazur, E. (2003). Subwavelength-diameter silica wires for low-loss optical wave guiding. *Nature*, 426(6968), 816–819.

[126] Tsien, R. Y. (1998). The green fluorescent protein. *Annual Review of Biochemisty*, 67(11), 509–44.

129

REFERENCES

[127] Urban, A. S., Carretero-Palacios, S., Lutich, A. A., Lohmüller, T., Feldmann, J., & Jäckel, F. (2014). Optical trapping and manipulation of plasmonic nanoparticles: fundamentals, applications, and perspectives. *Nanoscale*, 6(9), 4458–4474.

[128] Vahala, K. J. (2003). Optical microcavities. *Nature*, 424(6950), 839–846.

[129] Van de Hulst, H. C. (1957). *Light scattering by small particles*. Courier Corporation.

[130] Vaux, D. L. (2014). Basic statistics in cell biology. *Annual Review of Cell and Developmental Biology*, 30, 23–37.

[131] Vo-Dinh, T. (2008). Nanosensing at the single cell level. *Spectrochimica Acta - Part B*, 63(2), 95–103.

[132] Whelan, J. C., Karawdeniya, B. I., Bandara, Y. M. N. D. Y., Velleco, B. D., Masterson, C. M., & Dwyer, J. R. (2014). Electroless plating of thin gold films directly onto silicon nitride thin films and into micropores. *ACS Applied Materials and Interfaces*, 6(14), 10952–10957.

[133] Williams, K. R., Gupta, K., & Wasilik, M. (2003). Etch rates for micromachining processing - Part II. *Journal of Microelectromechanical Systems*, 12(6), 761–778.

[134] Wu, G., Datar, R. H., Hansen, K. M., Thundat, T., Cote, R. J., & Majumdar, A. (2001). Bioassay of prostate-specific antigen (PSA) using microcantilevers. *Nature Biotechnology*, 19(9), 856–860.

[135] Xie, X. S., Choi, P. J., Li, G.-W., Lee, N. K., & Lia, G. (2008). Single-molecule approach to molecular biology in living bacterial cells. *Annual Review of Biophysics*, 37, 417–444.

[136] Xie, Z., Dong, Y., Maeda, U., Moir, R. D., Xia, W., Culley, D. J., Crosby, G., & Tanzi, R. E. (2007). The inhalation anesthetic isoflurane induces a vicious cycle of apoptosis and Amyloid \textbeta -protein accumulation. *Journal of Neuroscience*, 27(6), 1247–1254.

[137] Yan, R., Park, J.-H., Choi, Y., Heo, C.-J., Yang, S.-M., Lee, L. P., & Yang, P. (2011). Nanowire-based single-cell endoscopy. *Nature Nanotechnology*, 7(3), 191–196.

[138] Yonzon, C. R., Jeoung, E., Zou, S., Schatz, G. C., Mrksich, M., & Duyne, R. P. V. (2004). A comparative analysis of localized and propagating surface

plasmon resonance sensors : The binding of Concanavalin A to a Monosaccharide functionalized self-assembled monolayer. *Journal of the American Chemical Society*, 126(39), 12669–12676.

[139] Yu, C. & Irudayaraj, J. (2007). Multiplex biosensor using gold nanorods. *Analytical Chemistry*, 79(2), 572–579.

[140] Yu, J., Zhou, J., Sutherland, A., Wei, W., Shin, Y. S., Xue, M., & Heath, J. R. (2014). Microfluidics-based single-cell functional proteomics for fundamental and applied biomedical applications. *Annual Review of Analytical Chemistry*, 7, 275–95.

[141] Yu, N., Genevet, P., Kats, M. a., Aieta, F., Tetienne, J.-P., Capasso, F., & Gaburro, Z. (2011). Light propagation with phase discontinuities: generalized laws of reflection and refraction. *Science*, 334(6054), 333–337.

[142] Zhang, J., Campbell, R. E., Ting, A. Y., & Tsien, R. Y. (2002). Creating new fluorescent probes for cell biology. *Nature Reviews. Molecular Cell Biology*, 3(12), 906–918.

[143] Zhang, J., Lang, H. P., Huber, F., Bietsch, A., Grange, W., Certa, U., McKendry, R., Güntherodt, H.-J., Hegner, M., & Gerber, C. (2006). Rapid and label-free nanomechanical detection of biomarker transcripts in human RNA. *Nature Nanotechnology*, 1(3), 214–220.

[144] Zhu, Y., Li, J., Li, W., Zhang, Y., Yang, X., Chen, N., Sun, Y., Zhao, Y., Fan, C., & Huang, Q. (2012). The biocompatibility of nanodiamonds and their application in drug delivery systems. *Theranostics*, 2(3), 302–312.

[145] Zijlstra, P., Paulo, P. M. R., & Orrit, M. (2012). Optical detection of single non-absorbing molecules using the surface plasmon resonance of a gold nanorod. *Nature Nanotechnology*, 7(6), 379–382.